The Dissertation Committee for Kayoung Lee Certifies that this is the approved version of the following dissertation:

QUANTUM TRANSPORT IN BILAYER GRAPHENE AND ITS HETEROSTRUCTURES

Committee:

Emanuel Tutuc, Supervisor

Sanjay Banerjee

L. Frank Register

Edward Yu

Allan H. MacDonald

QUANTUM TRANSPORT IN BILAYER GRAPHENE AND ITS HETEROSTRUCTURES

by

Kayoung Lee, B.S.E.E., M.S.E.

Dissertation

Presented to the Faculty of the Graduate School of
The University of Texas at Austin
in Partial Fulfillment
of the Requirements
for the Degree of

DOCTOR OF PHILOSOPHY

The University of Texas at Austin
May, 2016

Dedication

To my father, mother, and the best friend Sooel.

Acknowledgements

I deeply appreciate my advisor Prof. Emanuel Tutuc for his invaluable support and advice. I am sure that I cannot reach this point without his knowledge and help. His encouragement and exigence have enabled me to expand my intellectual horizons, and to improve the research than I expected. He has given a lot of suggestions and ideas in the journey of my research, and helped me improve this dissertation extensively.

Many thanks to Babak Fallahazad as I have learned a lot about fabrication and measurement skills from him; I am also very grateful for his inspiring and kind words many times. Many thanks to Jiamin Xue; the frequent research discussions with him taught me a great deal of fundamental physics, and I was inspired by his endless questions about science, and hard work. Many thanks to Seyoung Kim for teaching me fabrication and measurement skills, and also helping me to settle down in Austin; I learnt most of measurement skills from him, and I enjoyed the Magnet lab trips to Tallahassee. Many thanks to Junghyo Nah for his considerate words and a lot of suggestions, especially when I felt unfamiliar in many things in the beginning as a graduate student. Many thanks to Kyounghwan Kim for building the probes for our magnet and cryostat systems; my measurements were impossible without the equipment, and his endeavor and hard work was inspiring. Many thanks to Dave Dillen; I could measure my samples because of the magnet and cryostat systems he built as well as his help whenever the systems had issues. Many thanks to Stefano Larentis; I always enjoyed chatting with him, and his systematic and smart work have always inspired me.

I also deeply thank my family for their support and love. I appreciate Sooel Son who is my husband as well as my lifelong best friend. Your encouragement, emotional

support, foods, as well as technical support have helped me to endure and pass through difficult time throughout my doctoral studies. Thank you for making me happy and grateful.

QUANTUM TRANSPORT IN BILAYER GRAPHENE AND ITS HETEROSTRUCTURES

Kayoung Lee, Ph.D.

The University of Texas at Austin, 2016

Supervisor: Emanuel Tutuc

Bilayer graphene represents an attractive two-dimensional electron system for electron physics and potential device applications. In this dissertation, we present a comprehensive experimental study of electron transport in bilayer graphene, and its heterostructures. Using double bilayer graphene heterostructures, separated by a hexagonal boron nitride dielectric, we map the chemical potential in the bottom bilayer employing the top bilayer as a resistively detected Kelvin probe. The measured chemical potential-density dependence at zero magnetic field shows signatures of electron-electron interactions, along with electron-hole asymmetry. We provide an in-depth investigation of quantum Hall (QH) ferromagnetism in bilayer graphene, revealing new QH phases at filling factors $\nu = 0$ and $\nu = \pm 2$, predicted to possess coherent Landau level superpositions, spin-to-valley polarized transitions, as well as interaction-driven negative compressibility. We also study the interactions between the two bilayers, where the interlayer spacing is smaller than the intra-layer particle spacing by probing frictional drag, a phenomenon in which charge current flowing in one (drive) layer induces a voltage drop in the opposite (drag) layer. At temperatures (*T*) lower than 10

K, we observe a large anomalous negative drag near the drag layer charge neutrality, which increases dramatically with reducing *T*, strikingly becoming comparable to the layer resistivity at the lowest *T* = 1.5 K. A comparison of the drag resistivity and the drag layer Peltier coefficient suggests a thermoelectric origin of the drag.

Table of Contents

List of Tables

List of Figures

Chapter 1

Introduction

1.1 Motivation

Mono- and bilayer graphene are interesting two-dimensional electron systems for the study of various quantum transport phenomena [2], and potential device applications [3]. The differences in electronic structure and chirality between mono- and bilayer graphene [2] translate into the differences in fundamental physical properties. In particular, Bernal stacked bilayer graphene possesses a band gap and energy-momentum dispersion, which can be tuned by an applied transverse electric field [4–7], a feature renders the bilayer graphene attractive for both electronic and optoelectronic applications.

In a perpendicular magnetic field, bilayer graphene shows quantum Hall states (QHSs) at integer filling factors (ν) multiple of four because of spin and valley degeneracy, along with additional twofold orbital degeneracy, $N = 0$ and $N = 1$, at zero energy [4–7], which provides the richer QH phases in bilayer graphene. In the presence of Zeeman effect, interlayer bias, and electron-electron interactions, the eight-fold (four-fold) degeneracy for $N = 0, 1$ ($N \geq 2$) Landau levels (LLs) can be fully or partially lifted, leading to symmetry broken QHSs at integer fillings [1,7,8]. The competition between spin splitting and valley splitting, with the corrections by electron interactions can result in a variety of unique, and complex QH phases [1,8,9].

Graphene is also a good candidate to search for the electron-hole paired correlated states [10–12]. Distinct from fermionic electrons and holes, closely bound electron-hole pairs (indirect excitons) are bosons, which can condensate into a single quantum coherent electronic state [13]. Excitons are however prone to recombine, which leads to a short lifetime. To artificially pull apart the electrons and holes, two parallel electron and hole two-dimensional systems have been proposed. Depending on the thickness and the type of interlayer material, electrons in one layer can strongly interact with the holes in the opposite layer [13], and they are predicted to form strongly bound neutral excitons. Under such conditions, the electron-hole pairs in a quantum coherent state move both layers equally without dissipation. This has been experimentally observed at total filling factor $\nu_T = 1$such that each layer has one half-filled LL in a magnetic field [14,15]. However, despite the long-time theoretical and experimental efforts, it seems very challenging to observe the exciton condensation in equilibrium at zero magnetic field, or at different total filling in a high magnetic field. A recent theoretical study suggests that double bilayer graphene heterostructures as a candidate for the high-temperature exciton condensates [11,16], albeit the results remain under debate [17].

In this dissertation, we start with the derivation of the electronic band structure of mono- and bilayer graphene, and then focus on electron transport in double bilayer graphene heterostructures, consisting of two Bernal stacked bilayer graphene flakes separated by a hexagonal boron nitride dielectric. By using the top bilayer as a resistively detected Kelvin probe, we precisely map the chemical potential (Fermi energy) in the opposite (bottom) bilayer as a function of density and magnetic field [18]. Thermodynamic measurements of the chemical potential or the density of states are fundamental to understand the electronic and optical properties in bilayer graphene [19–22]. The chemical potential dependence on filling factor in high magnetic fields provides a direct measurement of the orbital LL energies, as well as the gaps of broken symmetry integer QHSs [18]. We also investigate the interactions between the two bilayers, where the interlayer spacing is smaller than the intra-layer particle spacing by probing frictional drag, a phenomenon in which charge current flowing in one (drive) layer induces a voltage drop (drag voltage) in the opposite (drag) layer. Despite we do not observe the signature of electron-hole pairs, this dissertation presents a strongly interacting regime at low temperatures, where the drag resistivity reaches comparable to layer resistivity, and discusses about thermoelectric contributions in the drag in our double bilayer graphene heterostructures.

1.2 Atomic Structure of Graphene

The atomic structure of monolayer graphene is described by a honeycomb lattice as presented in Fig. 1.1(a) [2], where the A and B represent the inequivalent atomic sub-lattices. In this regard, bilayer graphene consist of two layers of monolayer graphene as in Fig. 1.1(b) [5], the $\tilde{A}$ and $\tilde{B}$ are the inequivalent atomic sites of the second layer. The two honeycomb lattices are stacked for the $\tilde{A}$ and B (solid circle in Fig. 1.1(b)) to be aligned vertically to the graphene plane [5].

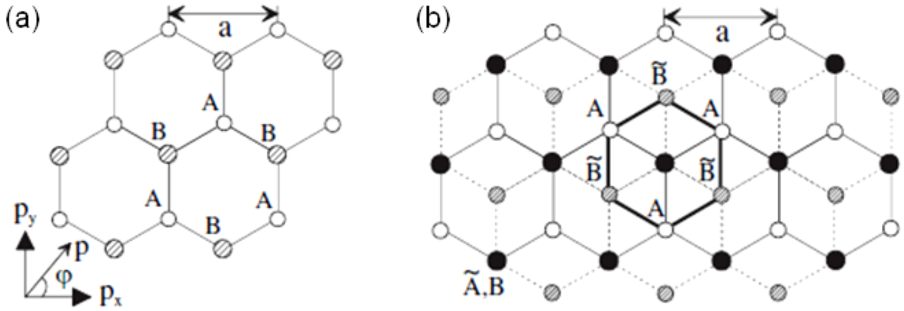

Figure 1.1: (a) Schematic of monolayer graphene. (b) Bilayer graphene containing four atoms in a unit cell: The representative A (white circle), $\tilde{B}$ (hashed), and $\tilde{A}$-B dimer (solid) are marked. Solid (dashed) lines indicate atomic bonds in the bottom (top) layer. a is the lattice constant. The figures are adapted from [5].

1.3 Tight-binding Description of Monolayer Graphene

Here, we derive energy (E) vs. wave-vector (k) relation in monolayer graphene using tight-binding approximation [23–27]. Block functions associated with the A and B atomic bases in N unit cells are described by

$$\Phi_i = \frac{1}{\sqrt{\mathrm{N}}}\sum_{\mathrm{R}_i}^{\mathrm{N}} \mathrm{e}^{\mathrm{i}k\cdot\mathrm{R}_i}\varphi_i(r-\mathrm{R}_i)\,, \quad (1.1)$$

, where R_i is the hexagonal lattice vector corresponding to the atomic sub-lattice i, which is either A or B, and φ_i is the atomic π orbital at an atom in the sub-lattice i. The Eigen wave function ψ in monolayer graphene then can be modeled by a linear combination

$$\psi = \mathrm{C_A}\Phi_\mathrm{A} + \mathrm{C_B}\Phi_\mathrm{B}, \quad (1.2)$$

C_i is the electronic amplitude of the Block function for the basis i, and the Eigen energy is obtained by

$$<\mathrm{E}> = \frac{<\psi|\hat{\boldsymbol{H}}|\psi>}{<\psi|\psi>} = \frac{\sum_{i,j}\mathrm{C}_i^*\mathrm{C}_j\mathrm{H}_{ij}}{\sum_{i,j}\mathrm{C}_i^*\mathrm{C}_j\mathrm{S}_{ij}}; \quad (1.3)$$

$\hat{\boldsymbol{H}}$ is Hamiltonian operator, $\mathrm{H}_{ij} = <\Phi_i|\hat{\boldsymbol{H}}|\Phi_j>$, and $\mathrm{S}_{ij} = <\Phi_i|\Phi_j>$. Minimizing the energy with respect to C_i^* provides

$$\mathbf{H}\mathrm{C} = \mathrm{E}\mathbf{SC}; \quad (1.4)$$

$\mathbf{H} = \begin{pmatrix}\mathrm{H_{AA}} & \mathrm{H_{AB}}\\ \mathrm{H_{BA}} & \mathrm{H_{BB}}\end{pmatrix}$ is transfer integral matrix, $\mathbf{S} = \begin{pmatrix}\mathrm{S_{AA}} & \mathrm{S_{AB}}\\ \mathrm{S_{BA}} & \mathrm{S_{BB}}\end{pmatrix}$ is overlap integral matrix, and $\mathbf{C} = \begin{pmatrix}\mathrm{C_A}\\ \mathrm{C_B}\end{pmatrix}$. The element of transfer integral matrix is

$$\mathrm{H}_{ij} = \frac{1}{\mathrm{N}}\sum_{\mathrm{R}_i,\,\mathrm{R}_j}^{\mathrm{N}} \mathrm{e}^{\mathrm{i}k\cdot(\mathrm{R}_j-\mathrm{R}_i)}\left\langle\varphi_i(r-\mathrm{R}_i)\middle|\hat{\boldsymbol{H}}\middle|\varphi_j(r-\mathrm{R}_j)\right\rangle. \quad (1.5)$$

Assuming that $\left\langle \varphi_i(r - \mathrm{R}_i) \middle| \hat{\boldsymbol{H}} \middle| \varphi_j(r - \mathrm{R}_j) \right\rangle$ has non-zero value only when $\varphi_i(r - \mathrm{R}_i)$ and $\varphi_j(r - \mathrm{R}_j)$ are identical, or the nearest neighbors, leads

$$\mathrm{H_{AA}} = \mathrm{H_{BB}} = \langle \varphi_{\mathrm{A}}(r) | \hat{\boldsymbol{H}} | \varphi_{\mathrm{A}}(r) \rangle \equiv \varepsilon_0, \quad (1.6)$$

to be the on-site electron energy ε_0, and the off-diagonal element

$$\mathrm{H_{AB}} = \frac{1}{\mathrm{N}} \sum_{\mathrm{R_A, R_B}}^{\mathrm{N}} \mathrm{e}^{\mathrm{i}k\cdot(\mathrm{R_B} - \mathrm{R_A})} \ \langle \varphi_{\mathrm{A}}(r - \mathrm{R_A}) | \hat{\boldsymbol{H}} | \varphi_{\mathrm{B}}(r - \mathrm{R_B}) \rangle = -\gamma_0 f(\mathrm{k}); \quad (1.7)$$

$$-\gamma_0 = \langle \varphi_{\mathrm{A}}(r - \mathrm{R_{A,i}}) | \hat{\boldsymbol{H}} | \varphi_{\mathrm{B}}(r - \mathrm{R}_{\mathrm{B},\ell}) \rangle, \quad (1.8)$$

$$f(k) = \sum_{\ell}^{3} \mathrm{e}^{\mathrm{i}k\cdot\delta_\ell}. \quad (1.9)$$

$-\gamma_0$ represents the coupling force between an atom A and one of the nearest neighbor atom B, and δ_ℓ is the three nearest neighbor vectors, ℓ = 1, 2, and 3, defined as

$$\delta_1 = \mathrm{R_{B,1}} - \mathrm{R_A} = (0, \frac{\mathrm{a}}{\sqrt{3}}),$$

$$\delta_2 = \mathrm{R_{B,2}} - \mathrm{R_A} = (\frac{\mathrm{a}}{2}, -\frac{\mathrm{a}}{2\sqrt{3}}), \quad (1.10)$$

$$\delta_3 = \mathrm{R_{B,3}} - \mathrm{R_A} = (-\frac{\mathrm{a}}{2}, -\frac{\mathrm{a}}{2\sqrt{3}}).$$

Therefore, the following Hamiltonian matrix is earned:

$$\mathbf{H} = \begin{pmatrix} \varepsilon_0 & -\gamma_0 f(\mathrm{k}) \\ -\gamma_0 f^*(\mathrm{k}) & \varepsilon_0 \end{pmatrix}. \quad (1.11)$$

In the similar manner, the overlap integral matrix elements are

$$\mathrm{S_{AA}} = \mathrm{S_{BB}} = \langle \varphi_{\mathrm{A}} | \varphi_{\mathrm{A}} \rangle = 1, \quad (1.12)$$

$$S_{AB} = \sum_{\ell}^{3} e^{ik\cdot\delta_\ell} <\varphi_A(r - R_A)|\varphi_B(r - R_{B,\ell})> = sf(k), \quad (1.13)$$

$$s = <\varphi_A(r - R_A)|\varphi_B(r - R_{B,\ell})> \quad (1.14)$$

which yield the overlap integral matrix

$$\mathbf{S} = \begin{pmatrix} 1 & sf(\mathrm{k}) \\ sf^*(\mathrm{k}) & 1 \end{pmatrix}. \quad (1.15)$$

The Eigen value equation and the corresponding energy are therefore written as

$$\begin{pmatrix} \varepsilon_0 & -\gamma_0 f(\mathrm{k}) \\ -\gamma_0 f^*(\mathrm{k}) & \varepsilon_0 \end{pmatrix}\begin{pmatrix} C_A \\ C_B \end{pmatrix} = E\begin{pmatrix} 1 & sf(\mathrm{k}) \\ sf^*(\mathrm{k}) & 1 \end{pmatrix}\begin{pmatrix} C_A \\ C_B \end{pmatrix}. \quad (1.16)$$

$$E = \frac{\varepsilon_0 \pm \gamma_0|f(\mathrm{k})|}{1 \mp s|f(\mathrm{k})|}. \quad (1.17)$$

Figure. 1.2(a) shows the electronic structure calculated using Eq. (1.17) in a Brillouin zone, while Fig. 1.2(b) presents the magnified spectrum in the vicinity of the *K*-valley, $\boldsymbol{K}_{\xi=\pm1} = \xi(4\pi/3a, 0)$.

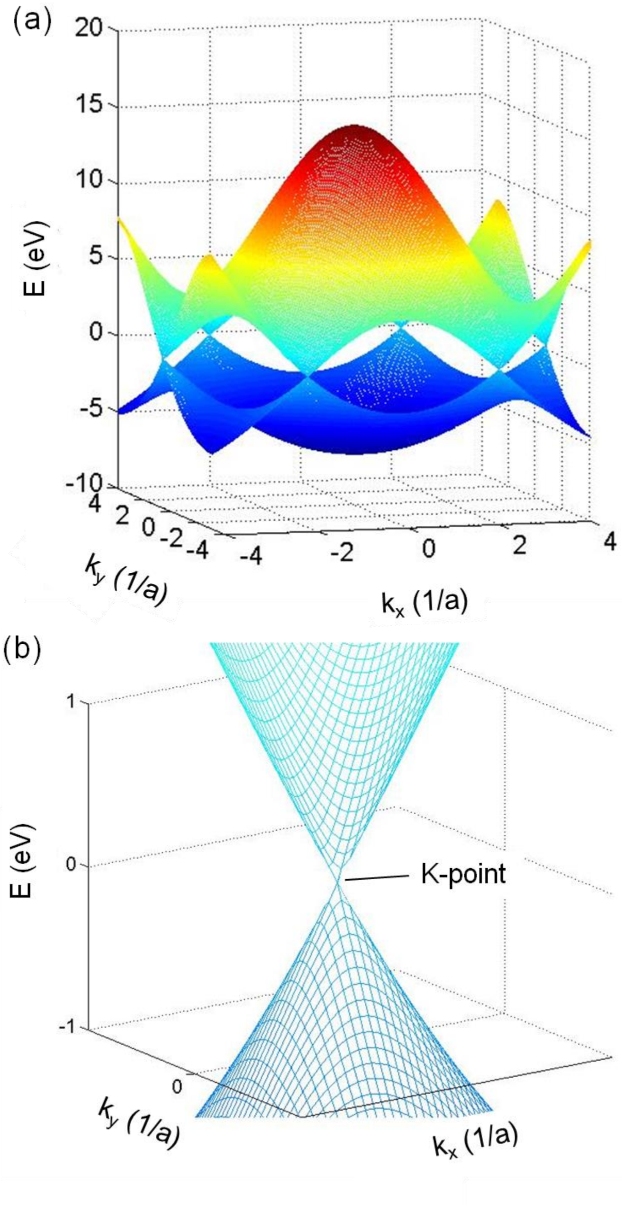

Figure 1.2: (a) Calculated E vs. *k* dispersion of monolayer graphene in the first Brillouin zone. (b) Linear dispersion noted in the vicinity of the *K*-valley.

Here, we focus on the low-energy spectrum in the vicinity of the *K*-valley. Using the Taylor expansion, *f*(*k*) is approximated into

$$f(k) = \sum_{\ell}^{3} \mathrm{e}^{\mathrm{i}k\cdot\delta_\ell} \approx -\frac{\sqrt{3}}{2}\frac{\mathrm{a}}{\hbar}(\xi p_\mathrm{x} - \mathrm{i}p_\mathrm{y}) \quad (1.18)$$

, p_x (p_y) is the x (y)-component of momentum (*p*), and subsequently H_AB becomes

$$\mathrm{H}_\mathrm{AB} \approx \frac{\sqrt{3}}{2}\frac{\mathrm{a}\gamma_0}{\hbar}(\xi p_\mathrm{x} - \mathrm{i}p_\mathrm{y}) = \upsilon_0(\xi p_\mathrm{x} - \mathrm{i}p_\mathrm{y}), \quad (1.19)$$

$\upsilon_0 = \frac{\sqrt{3}}{2}\frac{\mathrm{a}\gamma_0}{\hbar}$ is the carrier velocity in monolayer graphene. The effective Hamiltonian is then

$$\mathbf{H} = \upsilon_0\xi\begin{pmatrix} 0 & p_\mathrm{x} - \mathrm{i}p_\mathrm{y} \\ p_\mathrm{x} + \mathrm{i}p_\mathrm{y} & 0 \end{pmatrix} = \upsilon_0\xi p\begin{pmatrix} 0 & \mathrm{e}^{-\mathrm{i}\varphi} \\ \mathrm{e}^{\mathrm{i}\varphi} & 0 \end{pmatrix}. \quad (1.20)$$

This operates in the space of ψ_A and ψ_B, the electronic amplitudes on the sub-lattices A and B, respectively, at *K*-valley. The effective low-energy matrix equation is given as

$$\upsilon_0\xi p\begin{pmatrix} 0 & \mathrm{e}^{-\mathrm{i}\varphi} \\ \mathrm{e}^{\mathrm{i}\varphi} & 0 \end{pmatrix}\begin{pmatrix} \psi_\mathrm{A} \\ \psi_\mathrm{B} \end{pmatrix} = \mathrm{E}\begin{pmatrix} \psi_\mathrm{A} \\ \psi_\mathrm{B} \end{pmatrix}, \quad \mathrm{E} = \pm\upsilon_0 p. \quad (1.21)$$

The Bloch function amplitudes on the A and B are provided as

$$\begin{pmatrix} \psi_\mathrm{A} \\ \psi_\mathrm{B} \end{pmatrix} = \frac{1}{\sqrt{2}}\begin{pmatrix} \mathrm{e}^{-\mathrm{i}\frac{\varphi}{2}} \\ \mathrm{e}^{\mathrm{i}\frac{\varphi}{2}} \end{pmatrix}. \quad (1.22)$$

This shows that the wave functions on the A and B sub-lattices have the phase difference of φ, which leads to the absence of back-scattering, and the high mobility in monolayer graphene.

1.4 Tight-binding Description of Bilayer Graphene

We model bilayer graphene as two coupled honeycomb lattices as presented in Fig. 1.1(b) [5], where A and B ($\widetilde{\mathrm{A}}$ and $\widetilde{\mathrm{B}}$) are the inequivalent atomic bases in the bottom (top) hexagonal lattice, and the two honeycomb lattices are stacked for $\widetilde{\mathrm{A}}$ and B (solid circle in Fig. 1.1(b)) to be aligned vertically to the graphene plane [5]. E vs. *k* relation in bilayer graphene is obtained employing the nearest neighbor tight binding description [28], as used for the monolayer graphene electronic structure. The Eigen function ψ is written by the linear combination of Bloch functions at each atomic basis as

$$\psi = \sum_{i=\mathrm{A},\widetilde{\mathrm{A}},\mathrm{B},\widetilde{\mathrm{B}}} \mathrm{C}_i \Phi_i \,; \quad (1.23)$$

$$\Phi_i = \frac{1}{\sqrt{\mathrm{N}}} \sum_{\mathrm{R}_i}^{\mathrm{N}} \mathrm{e}^{\mathrm{i}k\cdot\mathrm{R}_i} \varphi_i(r - \mathrm{R}_i)\,, \quad (1.24)$$

Φ_i is the Bloch functions at atomic basis *i*, which is A, $\widetilde{\mathrm{A}}$, B, or $\widetilde{\mathrm{B}}$. The Hamiltonian matrix equation is then

$$\begin{pmatrix} \mathrm{H}_{\mathrm{AA}} & \mathrm{H}_{\mathrm{A}\widetilde{\mathrm{B}}} & \mathrm{H}_{\mathrm{A}\widetilde{\mathrm{A}}} & \mathrm{H}_{\mathrm{AB}} \\ \mathrm{H}_{\widetilde{\mathrm{B}}\mathrm{A}} & \mathrm{H}_{\widetilde{\mathrm{B}}\widetilde{\mathrm{B}}} & \mathrm{H}_{\widetilde{\mathrm{B}}\widetilde{\mathrm{A}}} & \mathrm{H}_{\widetilde{\mathrm{B}}\mathrm{B}} \\ \mathrm{H}_{\widetilde{\mathrm{A}}\mathrm{A}} & \mathrm{H}_{\widetilde{\mathrm{A}}\widetilde{\mathrm{B}}} & \mathrm{H}_{\widetilde{\mathrm{A}}\widetilde{\mathrm{A}}} & \mathrm{H}_{\widetilde{\mathrm{A}}\mathrm{B}} \\ \mathrm{H}_{\mathrm{BA}} & \mathrm{H}_{\mathrm{B}\widetilde{\mathrm{B}}} & \mathrm{H}_{\mathrm{B}\widetilde{\mathrm{A}}} & \mathrm{H}_{\mathrm{BB}} \end{pmatrix} \begin{pmatrix} \mathrm{C}_{\mathrm{A}} \\ \mathrm{C}_{\widetilde{\mathrm{B}}} \\ \mathrm{C}_{\widetilde{\mathrm{A}}} \\ \mathrm{C}_{\mathrm{B}} \end{pmatrix} = \mathrm{E} \begin{pmatrix} \mathrm{S}_{\mathrm{AA}} & \mathrm{S}_{\mathrm{A}\widetilde{\mathrm{B}}} & \mathrm{S}_{\mathrm{A}\widetilde{\mathrm{A}}} & \mathrm{S}_{\mathrm{AB}} \\ \mathrm{S}_{\widetilde{\mathrm{B}}\mathrm{A}} & \mathrm{S}_{\widetilde{\mathrm{B}}\widetilde{\mathrm{B}}} & \mathrm{S}_{\widetilde{\mathrm{B}}\widetilde{\mathrm{A}}} & \mathrm{S}_{\widetilde{\mathrm{B}}\mathrm{B}} \\ \mathrm{S}_{\widetilde{\mathrm{A}}\mathrm{A}} & \mathrm{S}_{\widetilde{\mathrm{A}}\widetilde{\mathrm{B}}} & \mathrm{S}_{\widetilde{\mathrm{A}}\widetilde{\mathrm{A}}} & \mathrm{S}_{\widetilde{\mathrm{A}}\mathrm{B}} \\ \mathrm{S}_{\mathrm{BA}} & \mathrm{S}_{\mathrm{B}\widetilde{\mathrm{B}}} & \mathrm{S}_{\mathrm{B}\widetilde{\mathrm{A}}} & \mathrm{S}_{\mathrm{BB}} \end{pmatrix} \begin{pmatrix} \mathrm{C}_{\mathrm{A}} \\ \mathrm{C}_{\widetilde{\mathrm{B}}} \\ \mathrm{C}_{\widetilde{\mathrm{A}}} \\ \mathrm{C}_{\mathrm{B}} \end{pmatrix}, \quad (1.25)$$

where the element of the Hamiltonian matrix is

$$\mathrm{H}_{ij}\Big|_{i,j=\mathrm{A},\widetilde{\mathrm{A}},\mathrm{B},\widetilde{\mathrm{B}}} = \langle \Phi_i | \hat{\boldsymbol{H}} | \Phi_j \rangle = \frac{1}{\mathrm{N}} \sum_{\mathrm{R}_i}^{\mathrm{N}} \sum_{\mathrm{R}_j}^{\mathrm{N}} \mathrm{e}^{\mathrm{i}k\cdot(\mathrm{R}_j - \mathrm{R}_i)} \left\langle \varphi_i(r - \mathrm{R}_i) \middle| \hat{\boldsymbol{H}} \middle| \varphi_j(r - \mathrm{R}_j) \right\rangle . \quad (1.26)$$

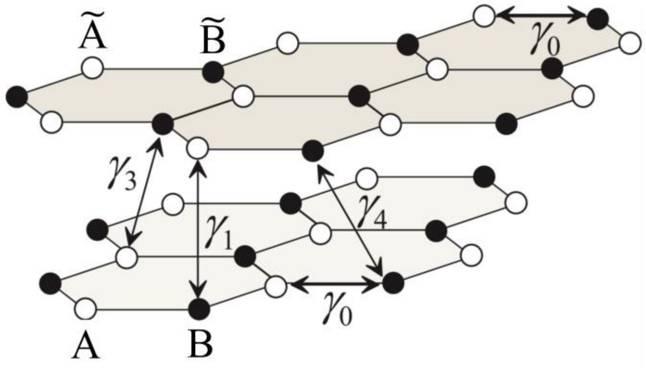

Figure 1.3: Atomic structure of bilayer graphene. The four different nearest neighbor atomic couplings are marked. The figure is adapted and modified from [28].

Considering only four nearest neighbor atomic couplings as marked in Fig. 1.3 [28], we obtain the matrix elements such as

$$H_{AA} = H_{\tilde{A}\tilde{A}} = H_{BB} = H_{\tilde{B}\tilde{B}} = \varepsilon_0, \quad (1.27)$$

$$H_{AB} = H_{\tilde{A}\tilde{B}} = H_{BA}{}^{*} = H_{\tilde{B}\tilde{A}}{}^{*} = -\gamma_0 f(k), \quad (1.28)$$

$$H_{\tilde{A}B} = H_{B\tilde{A}} = \gamma_1, \quad (1.29)$$

$$H_{A\tilde{B}} = H_{\tilde{B}A}{}^{*} = \gamma_3 f(k), \quad (1.30)$$

$$H_{A\tilde{A}} = H_{B\tilde{B}} = H_{\tilde{A}A}{}^{*} = H_{\tilde{B}B}{}^{*} = -\gamma_4 f(k), \quad (1.31)$$

where γ_0 is the nearest-neighbor coupling within the intra-layer, γ_1 is the coupling force in the $\tilde{A}$-B dimmer, which is the strongest inter-layer coupling parameter, leading to the high (deep) energy bands, γ_3 is weak A-$\tilde{B}$ coupling, and γ_4 is weaker coupling in either A-$\tilde{A}$ or B-$\tilde{B}$. The Hamiltonian and overlap integral matrix are therefore given as

$$\mathbf{H} = \begin{pmatrix} \varepsilon_0 & \gamma_3 g(\mathrm{k}) & \gamma_4 f(\mathrm{k}) & -\gamma_0 f(\mathrm{k}) \\ \gamma_3 f(\mathrm{k}) & \varepsilon_0 & -\gamma_0 f^*(\mathrm{k}) & \gamma_4 f^*(\mathrm{k}) \\ \gamma_4 f^*(\mathrm{k}) & -\gamma_0 f(\mathrm{k}) & \varepsilon_0 & \gamma_1 \\ -\gamma_0 f^*(\mathrm{k}) & \gamma_4 f(\mathrm{k}) & \gamma_1 & \varepsilon_0 \end{pmatrix}, \quad (1.32)$$

$$\mathbf{S} = \begin{pmatrix} 1 & 0 & 0 & sf(\mathrm{k}) \\ 0 & 1 & sf^*(\mathrm{k}) & 0 \\ 0 & sf(\mathrm{k}) & 1 & s_1 \\ sf^*(\mathrm{k}) & 0 & s_1 & 1 \end{pmatrix} \quad (1.33)$$

Tayler expansion of $f(k)$ for the small wave vector yields the following low-energy Hamiltonian matrix equation

$$\begin{pmatrix} 0 & \upsilon_3 p\mathrm{e}^{\mathrm{i}\varphi} & 0 & \upsilon p\mathrm{e}^{-\mathrm{i}\varphi} \\ \upsilon_3 p\mathrm{e}^{-\mathrm{i}\varphi} & 0 & \upsilon p\mathrm{e}^{\mathrm{i}\varphi} & 0 \\ 0 & \upsilon p\mathrm{e}^{-\mathrm{i}\varphi} & 0 & \gamma_1 \\ \upsilon p\mathrm{e}^{\mathrm{i}\varphi} & 0 & \gamma_1 & 0 \end{pmatrix} \begin{pmatrix} \psi_{\mathrm{A}} \\ \psi_{\tilde{\mathrm{B}}} \\ \psi_{\tilde{\mathrm{A}}} \\ \psi_{\mathrm{B}} \end{pmatrix} = \mathrm{E} \begin{pmatrix} \psi_{\mathrm{A}} \\ \psi_{\tilde{\mathrm{B}}} \\ \psi_{\tilde{\mathrm{A}}} \\ \psi_{\mathrm{B}} \end{pmatrix}, \quad (1.34)$$

$$\upsilon = \frac{\sqrt{3}}{2}\frac{\mathrm{a}\gamma_0}{\hbar},$$

$$\upsilon_3 = -\frac{\sqrt{3}}{2}\frac{\mathrm{a}\gamma_3}{\hbar},$$

where γ_4 is neglected, which is much smaller than γ_1, and ψ_{A}, $\psi_{\tilde{\mathrm{B}}}$, $\psi_{\tilde{\mathrm{A}}}$, and ψ_{B} are the amplitudes of the low-energy Bloch functions at sub-lattices A, $\tilde{\mathrm{B}}$, $\tilde{\mathrm{A}}$, and B, respectively. Solving the seqular equation provides the four energy bands yields

$$(\mathrm{E}_{\pm}^{\alpha})^2 = \frac{{\gamma_1}^2}{2} + \left(\upsilon^2 + \frac{{\upsilon_3}^2}{2}\right)p^2 + (-1)^{\alpha}\sqrt{\Gamma}, \quad (1.35)$$

$$\Gamma = \frac{1}{4}({\gamma_1}^2 - {\upsilon_3}^2 p^2) + \upsilon^2 p^2({\gamma_1}^2 + {\upsilon_3}^2 p^2) + 2\gamma_1 \upsilon_3 \upsilon^2 p^3 \cos 3\phi, \quad (1.36)$$

$\alpha = 1$ (2) represents the lower (higher) energy band, and + (−) represents the conduction (valence) band. The higher energy band with $\alpha = 2$ is formed by the strong A-$\widetilde{\mathrm{B}}$ dimmers, and away from zero energy (ε_0) by about $\pm|\gamma_1|$ [28], whereas the lower energy band with $\alpha = 1$ is formed by the wave functions on $\widetilde{\mathrm{A}}$ and B, which is further approximated into

$$\mathrm{E}_{\pm}^{1} = \pm\left(\frac{1}{2}\right)\gamma_1\left(\sqrt{1+\frac{4\upsilon^2 p^2}{{\gamma_1}^2}}-1\right). \quad (1.37)$$

The lower energy band is close to the parabolic dispersion $\mathrm{E}_{\pm}{}^{1} \approx \pm p^2/2m^*$, $m^* = \gamma_1/2\upsilon^2$, in the vicinity of zero energy, while it approaches to the linear dispersion $\mathrm{E}_{\pm}{}^{1} \approx \pm p\upsilon$ at higher energy [5,28].

Because the lower energy band is composed of Bloch functions on the $\widetilde{\mathrm{A}}$ and B bases, it is convenient to have a Hamiltonian in the space of these two bases [5,28]. The two-component Hamiltonian is obtained by eliminating the $\widetilde{\mathrm{A}}$ and B dimer components, which lead to the higher energy band, and treating γ_1 as very large. Eq. (1.34) can be also represented as

$$\upsilon_3 p e^{i\varphi}\psi_{\widetilde{\mathrm{B}}} + \upsilon p e^{-i\varphi}\psi_{\mathrm{B}} = \mathrm{E}\psi_{\mathrm{A}}, \quad (1.38)$$

$$\upsilon_3 p e^{-i\varphi}\psi_{\mathrm{A}} + \upsilon p e^{i\varphi}\psi_{\widetilde{\mathrm{A}}} = \mathrm{E}\psi_{\widetilde{\mathrm{B}}}, \quad (1.39)$$

$$\upsilon p e^{-i\varphi}\psi_{\widetilde{\mathrm{B}}} + \gamma_1\psi_{\mathrm{B}} = \mathrm{E}\psi_{\widetilde{\mathrm{A}}}, \quad (1.40)$$

$$\upsilon p e^{i\varphi}\psi_{\mathrm{A}} + \gamma_1\psi_{\widetilde{\mathrm{A}}} = \mathrm{E}\psi_{\mathrm{B}}, \quad (1.41)$$

By substituting Eq. (1.41) into ψ_{B} in Eq. (1.40),

$$\psi_{\widetilde{\mathrm{A}}} = \frac{1}{-\gamma_1} vp\mathrm{e}^{\mathrm{i}\varphi}\psi_{\mathrm{A}}. \quad (1.42)$$

By substituting the above equation into $\psi_{\widetilde{\mathrm{A}}}$ in Eq. (1.40),

$$\psi_{\mathrm{B}} = \frac{1}{-\gamma_1}\, vp\mathrm{e}^{-\mathrm{i}\varphi}\psi_{\widetilde{\mathrm{B}}}. \quad (1.43)$$

Using Eq. (1.42) and Eq. (1.43),

$$\mathbf{H} = -\frac{v^2}{\gamma_1}\begin{pmatrix} 0 & (p\mathrm{e}^{-\mathrm{i}\varphi})^2 \\ (p\mathrm{e}^{\mathrm{i}\varphi})^2 & 0 \end{pmatrix} + v_3\begin{pmatrix} 0 & p\mathrm{e}^{\mathrm{i}\varphi} \\ p\mathrm{e}^{-\mathrm{i}\varphi} & 0 \end{pmatrix} \quad (1.44)$$

By neglecting the weaker γ_3 coupling, the effective Schrodinger matrix equation is further approximated into

$$-\frac{p^2}{2m^*}\begin{pmatrix} 0 & \mathrm{e}^{-\mathrm{i}2\varphi} \\ \mathrm{e}^{\mathrm{i}2\varphi} & 0 \end{pmatrix}\begin{pmatrix} \psi_{\mathrm{A}} \\ \psi_{\widetilde{\mathrm{B}}} \end{pmatrix} = \mathrm{E}\begin{pmatrix} \psi_{\mathrm{A}} \\ \psi_{\widetilde{\mathrm{B}}} \end{pmatrix}. \quad (1.45)$$

Near the zero energy, the energy-momentum dispersion becomes near parabolic, and the corresponding low-energy electronic states are given as

$$\begin{pmatrix} \psi_{\mathrm{A}} \\ \psi_{\widetilde{\mathrm{B}}} \end{pmatrix} = \frac{1}{\sqrt{2}}\begin{pmatrix} \mathrm{e}^{-\mathrm{i}\varphi} \\ \mathrm{e}^{\mathrm{i}\varphi} \end{pmatrix}. \quad (1.46)$$

While in monolayer graphene back-scattering is suppressed because of the phase difference φ between the atomic sites A and $\widetilde{\mathrm{B}}$, in bilayer graphene back-scattering is present by the phase difference 2φ.

Chapter 2

Chemical Potential and Quantum Hall Ferromagnetism in Bilayer Graphene[*]

Bilayer graphene has a distinctive electronic structure influenced by a complex interplay between various degrees of freedom. We probed its chemical potential using double bilayer graphene heterostructures, separated by a hexagonal boron nitride dielectric, where one bilayer can serve as gate and resistively detected Kelvin probe for the opposite bilayer. The chemical potential has a non-linear carrier density dependence, and bears signatures of electron-electron interactions. The data allowed a direct measurement of the electric field-induced bandgap at zero magnetic field, the orbital Landau level (LLs) energies, and the broken symmetry quantum Hall state gaps at high magnetic fields. We observe spin-to-valley polarized transitions for all half-filled LLs, as well as emerging phases at filling factors $\nu = 0$ and $\nu = \pm 2$, theoretically expected to have quantum coherence between different LLs. Furthermore, the data reveal interaction-driven negative compressibility and electron-hole asymmetry in $N = 0, 1$ LLs.

---

[*] Portions of this chapter were published previously: Kayoung Lee, Babak Fallahazad, Jiamin Xue, David C. Dillen, Kyounghwan Kim, Takashi Taniguchi, Kenji Watanabe, and Emanuel Tutuc, “Chemical potential and quantum Hall ferromagnetism in bilayer graphene,” *Science* 345, 58 (2014) [18].

Kayoung Lee performed the sample fabrication, and the low temperature measurements. Babak Fallahazad and Jiamin Xue assisted in sample fabrication, and Emanuel Tutuc assisted in low temperature measurements. David C. Dillen and Kyounghwan Kim built the cryostat and probing systems, and Takashi Taniguchi and Kenji Watanabe synthesized the hBN crystals. Kayoung Lee and Emanuel Tutuc analyzed the data and wrote the paper with input from all authors.

2.1 Introduction

Bilayer graphene represents a peculiar two-dimensional electron system [2,4], possessing a bandgap and energy-momentum dispersion that can be tuned by an applied transverse electric (*E*) field [5,6]. In high magnetic (*B*) fields, electron-electron interactions coupled with the spin and valley degrees of freedom can lead to a diverse set of quantum Hall states (QHSs) [1,2,4–9,29]. Thermodynamic measurements of the chemical potential or the density of states are fundamental to understanding the electronic properties of bilayer graphene [19–22]. Global compressibility measurements in the density of states (DOS) of bilayer graphene [19,20] report the DOS modulation associated with fourfold, spin- and valley-degenerate Landau levels (LLs), while local compressibility measurements in single-gated suspended bilayer graphene samples reveal broken symmetry QHSs [21].

2.2 Methods

2.2.1 Sample Preparation

The samples investigated in this study consist of two Bernal stacked bilayer graphene flakes, separated by a thin hexagonal boron nitride (hBN). The fabrication of samples studied here starts with consecutive mechanical exfoliations of hBN onto silicon dioxide thermally grown on a highly doped Si substrate, and bilayer graphene onto poly-methyl-methacrylate (PMMA) spin on water-soluble polyvinyl-alcohol (PVA) layer on a

Si substrate. The exfoliated hBN flakes are scanned using atomic force microscopy (AFM) to determine the thickness, and to probe the surface topography, and optical contrast and Raman spectroscopy are used to identify the number of graphene layers. Figure 2.1(a,b) show the optical micrograph and the AFM image of an example of exfoliated hBN on SiO_2, respectively. Note that this flake was annealed at 350 °C in vacuum for 6 hours to remove tape residue from the exfoliation process before the AFM scanning, which confirms the ultraclean surface with roughness lower than 0.2 nm (Fig. 2.1(b)). The light blue color of hBN on 290 nm thick SiO_2/Si reveals the thickness of this flake would be roughly 30 ~ 50 nm, and the AFM measures its thickness as 46 nm, which is suitable for the use of bottom (substrate) hBN. Figure 2.2 shows the exfoliated graphene on a PMMA/PVA polymer stack, where monolayer, bilayer, and trilayer graphene are marked.

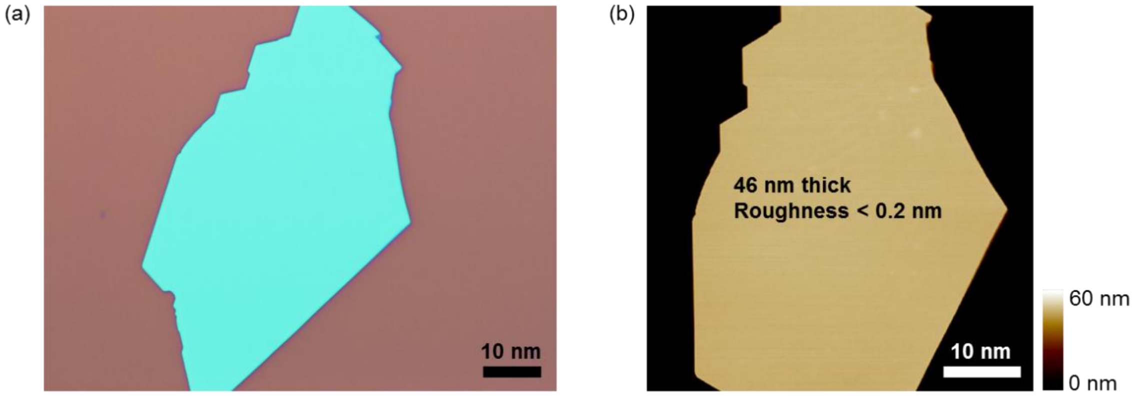

Figure 2.1: (a) Exfoliated hBN on thermally grown 290 nm thick SiO_2 on a Si substrate. The sample is annealed in 350 °C in vacuum for 6 hours to remove the tape residue from the exfoliation process. (b) AFM image of the hBN in (a). This shows ultraclean surface with the roughness lower than 0.2 nm.

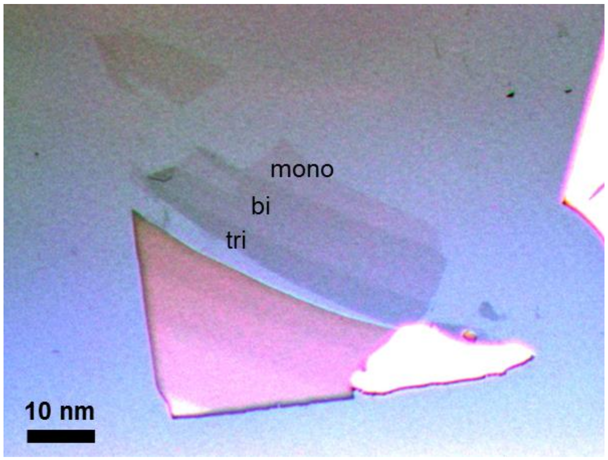

Figure 2.2: Exfoliated graphene on a PMMA/PVA polymer stack spin on a Si substrate. Optical contrast is not very strong, but monolayer, bilayer, and trilayer are distinguishable. Raman spectroscopy further helps the identification of the number of layers.

The identified bilayer graphene/PMMA/PVA/Si sample is then floated on water, which dissolves the PVA layer from the side of the floated sample. Once the PVA is fully dissolved, the PMMA film will be detached from the Si substrate, which sinks into the water while leaving the PMMA layer on water. Using a thin glass slide with a hole, we fish out the PMMA film carefully to situate the graphene flake inside the hole of the glass slide, as described in Ref. [30,31]. After drying the fished PMMA film in the atmosphere for a couple of hours, the graphene flake is carefully aligned and transferred on top of a thick (30 to 50 nm) hBN flake exfoliated on a SiO_2/Si substrate, where a mask aligner and a microscope are used. After the transfer, PMMA is removed in acetone, and annealed at 350 °C in vacuum to remove the PMMA residue. On the transferred graphene on hBN, a number of graphene bubbles are formed in general, and the annealing process helps decreasing the density of bubbles. Figure 2.3 presents the AFM images of an example of transferred graphene on hBN before and after the annealing procedure. This shows the annealing is effective to reduce the density of graphene bubbles, and to remove the process residue.

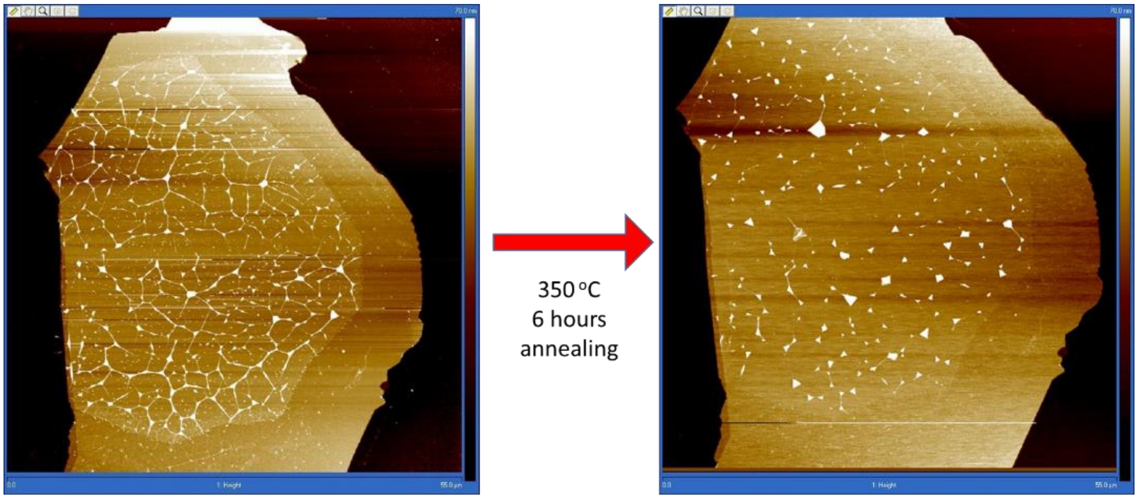

Roughness > 1nm by PMMA residue
Lots of graphene bubbles

Roughness < 0.3 nm
Reduced number of graphene bubbles

Figure 2.3: AFM images before and after 350 °C annealing in vacuum for 6 hours. The transferred graphene on hBN has a number of graphene bubbles and wrinkles, as well as lots of PMMA residue even after cleaning in hot acetone for couple of hours. The roughness is higher than 1 nm. After the annealing, the number of graphene bubbles is reduced, and the PMMA residue is effectively removed, showing the roughness lower than 0.3 nm, which is close to the roughness of bare exfoliated hBN after annealing.

Figure 2.4(a,b) represent the optical micrograph and AFM image after the graphene in Fig. 2.2 is transferred on top of the hBN in Fig. 2.1, respectively, which was annealed before the AFM scanning. From the AFM image, we find a large bubble free area, as marked by the red dashed line in Fig. 2.4(b). Electron-beam lithography and oxygen plasma etching are performed to define a multi-terminal Hall bar on the bubble free area, which can be skip depending on the size and shape of the transferred graphene. Figure 2.4(c,d) are the optical micrograph and AFM image after the trimming. The AFM image shows that the trimming was well performed on the bubble free area accurately. Note that this etched structure does not represent the final shape of the channel area. After having interlayer hBN, top bilayer graphene, and top hBN, which can possibly generate additional bubbles, we trim additionally to have a bubble free double bilayer graphene stack, and to have Hall bar edges of the top and bottom bilayer graphene aligned.

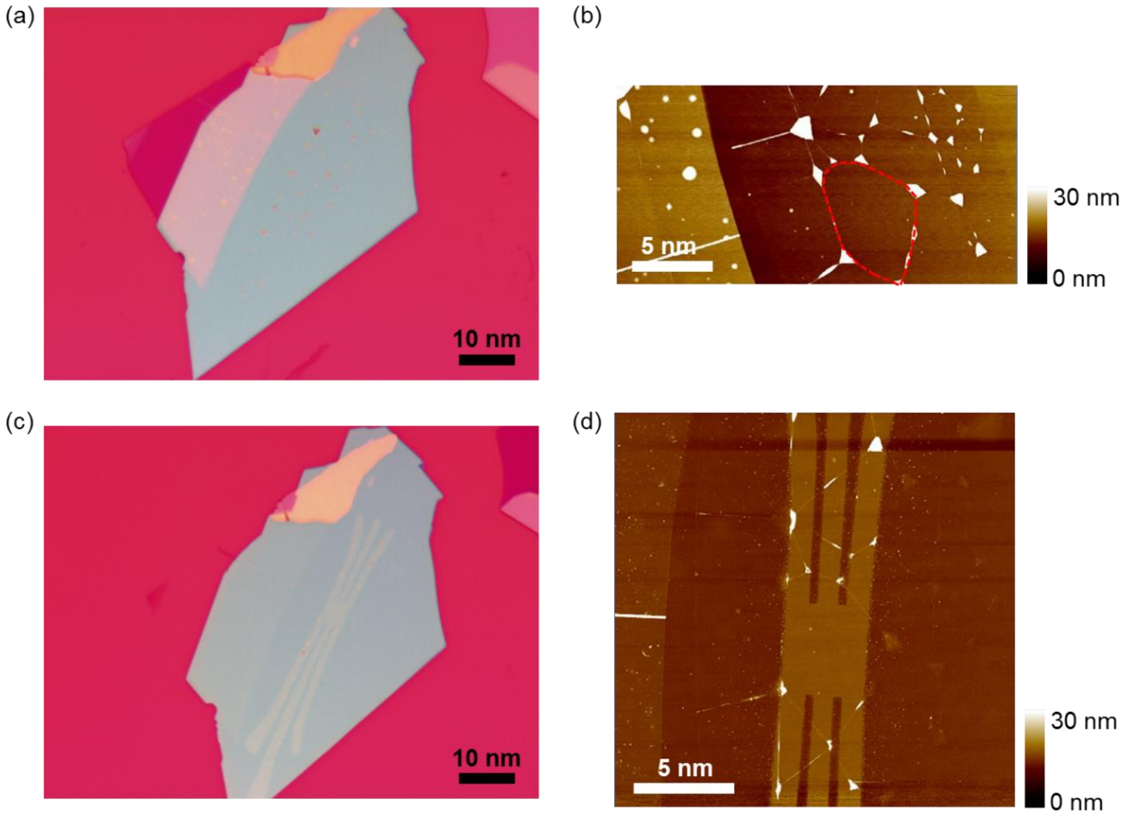

Figure 2.4: (a) Graphene transferred on hBN. After the transfer, the sample was annealed at 350 °C in vacuum for 6 hours to remove PMMA residue. (b) AFM image of the transferred graphene on hBN. Graphene has a number of bubbles on hBN, but we can spot a relatively large bubble free area, marked by the red dashed line. (c) The graphene is trimmed to have the channel area in the bubble free area. (b) AFM image shows that the trimming was well performed on the right position. Note that this trimmed structure does not represent the final shape of the channel area. After having interlayer hBN, top graphene, and top hBN, which can possibly form additional bubbles, we etch through to have a bubble free double bilayer graphene stack.

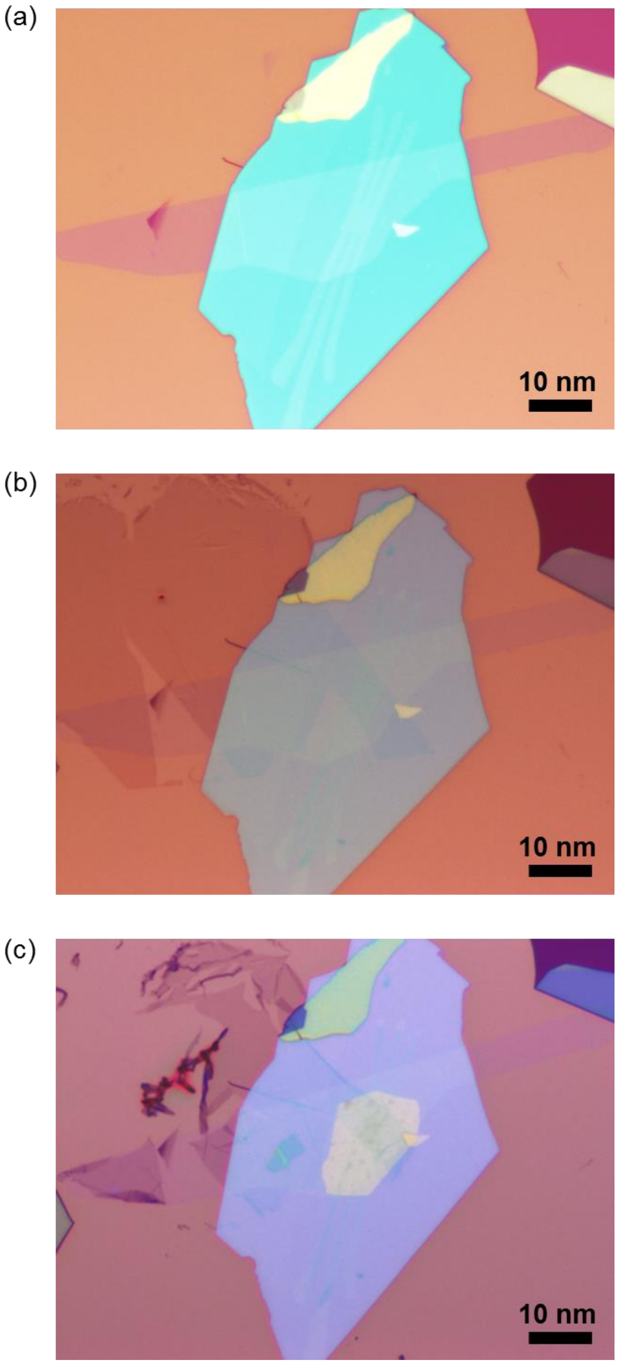

Figure 2.5: Optical micrographs of the stack (a) after interlayer hBN transfer, (b) top bilayer graphene transfer, and (c) top hBN transfer.

The second, relatively thin (2 to 6 nm) hBN crystal, and the top bilayer graphene are successively transferred on top of the bottom bilayer graphene Hall bar. To achieve high mobility top bilayer graphene, we should encapsulate the top bilayer graphene with an additional top hBN flake. Figure 2.5(a,b,c) are the micrographs after hBN transfer, top bilayer graphene transfer, and top hBN transfer, respectively. After the transfer of each layer, ultra-high vacuum annealing at 350 °C is performed to remove process residue. After having either graphene/hBN/graphene/hBN or hBN/graphene/hBN/graphene/hBN heterostructures, the whole stacks are then etched through using CHF_3 plasma to ensure the Hall bar edges of the top and bottom bilayer graphene are aligned. This CHF_3 etching also allow to realize 1-dimensional (edge) contacts to graphene [32] by exposing the etched 1-dimensional region of graphene underneath interlayer and/or top hBN. Electron-beam lithography and the metal deposition are subsequently performed to finalize a double bilayer graphene sample, where each bilayer graphene has independent contacts. To avoid the top and bottom bilayer graphene touching each other, and to have multiple contacts on each bilayer graphene, the device structure design which includes each layer transfer and etching procedures should be implemented very carefully. Figure 2.6 shows an example of a finished sample, after the CHF_3 plasma etching for trimming and edge contacts, as well as Au/Cr metallization.

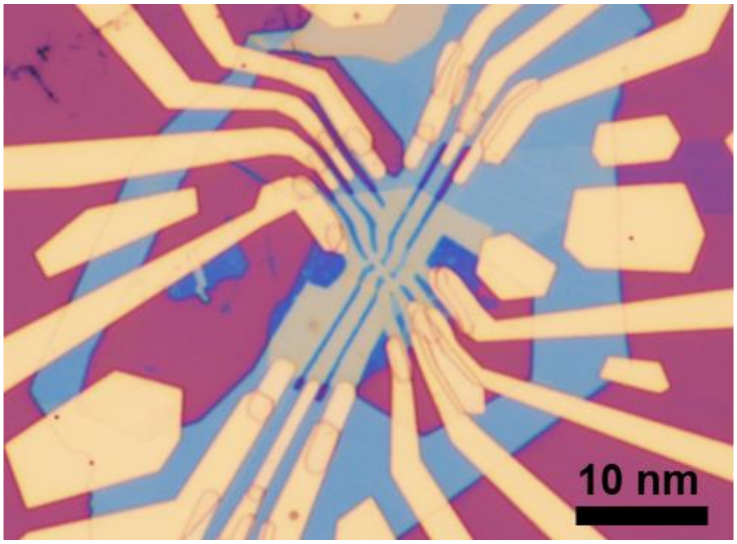

Figure 2.6: Optical micrograph of a double bilayer graphene heterostructures.

2.2.2 Measurements

Two and four-point layer resistance measurements were performed on the top and bottom bilayer graphene as a function of back-gate (V_{BG}), and inter-layer bias (V_{TL}) applied on the top bilayer, by flowing source currents of 1 nA on each layer, using lock-in amplifiers as described in Fig. 2.7. Different lock-in frequencies, ranging between 11 − 17 Hz were chosen for the top and bottom bilayers to exclude cross-talk. A radio-frequency transformer (Jensen Transformers, model JT-SUB-BB) is used to flow an AC current on the top layer, while applying a DC bias VTL, with respect to ground. The samples were measured in a variable-temperature liquid ^{4}He flow cryostat in zero and high magnetic fields up to 14 T. Six samples, labelled #1, #2, #3, #4, #5 and #6, were investigated in this study, and their specifications are provided in Table 2.1. The bottom bilayer graphene in all the samples have mobilities ranging between 100,000 – 290,000 cm^2/Vs, whereas the top bilayers have lower mobilities ranging between 3400 – 68,000 cm^2/Vs.

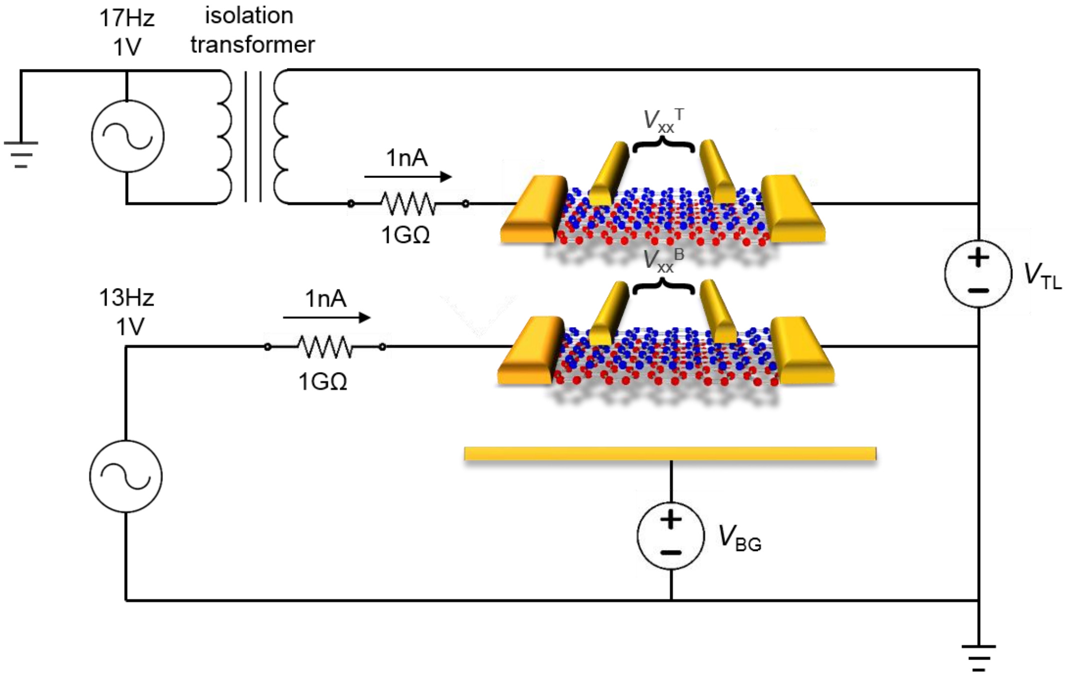

Figure 2.7: Schematic of the circuit used to probe the double bilayer as a function of interlayer (V_{TL}) and back-gate (V_{BG}) bias. The two bilayers are separated for clarity.

Sample	interlayer thickness (nm)	C_{BG} (nF/cm^2)	C_{int} (nF/cm^2)	interlayer resistance (GΩ)	cool down	bottom bilayer mobility (cm^2/Vs)	top bilayer mobility (cm^2/Vs)	E_{B0} (V/nm)	E_{T0} (V/nm)	Note
#1	5.5	10	430	20	1	110,000 – 100,000	3400	0.54	~ 0.5	sample #1 [18], Sample D [33]
#2	2	10.5	1097	1.6	1	210,000 – 180,000	3500	0.21	~ 0.25	sample #2 [18], Sample C [33], Device #1 [34]
#3	5	10.7	410		1	290,000 – 190,000	8100 – 6400	0.46	~ 0.4	sample #3 [18]
#4	3	11	840	5.3	1	260,000 – 180,000	68,000 – 51,000	0.03 – 0.04	~ 0.1	Sample A [33]
					2	95,000 – 68,000	51,000 – 31,000	0.04	~ 0.1	
#5	2	11.58	1085	4	1	120,000 – 62,000	19,000 – 9000	0.11	~ 0	Sample B [33]
#6	1.3	10.5	1200	0.003	1	155,000 – 126,000	17,000	~ 0	~ 0	
#7	2.7	11	900	4	1	24,000	2000			Sample E [33]

Table 2.1: Specifications of our double bilayer graphene samples

2.3 Chemical Potential Mapping in Bilayer Graphene at $B = 0$

Figure 2.8(b,c) show contour plots of the measured top (panel (b)), and bottom (panel (c)) bilayer resistances measured at a temperature $T = 1.4$ K. The top (n_T) and bottom (n_B) bilayer densities depend on V_{BG} and V_{TL} as follows [35]:

$$eV_{BG} = e^2(n_B + n_T)/C_{BG} + \mu_B \qquad (2.1)$$

$$eV_{TL} = -e^2 n_T/C_{int} - \mu_T + \mu_B \qquad (2.2)$$

Here, C_{BG} and C_{int} represent the bottom and interlayer dielectric capacitances, whereas μ_B and μ_T represent the chemical potentials (Fermi energies) of the bottom and top bilayers, respectively; e is the electron charge. We note that μ and n are positive (negative) for electrons (holes), and V_{BG} and V_{TL} in Eqs. (2.1) and (2.2) are referenced with the bias values at which both bilayers are charge neutral, i.e. at the double neutrality point (DNP). The externally applied transverse E-field across the bottom bilayer is written as follows:

$$E = en_B/2\varepsilon_0 + en_T/\varepsilon_0 + E_0 \qquad (2.3)$$

ε_0 is the vacuum permittivity, n_B and n_T are determined using Eqs. (2.1) and (2.2), and E_0 is an additive E-field at DNP, associated with the unintentional doping of the top bilayer.

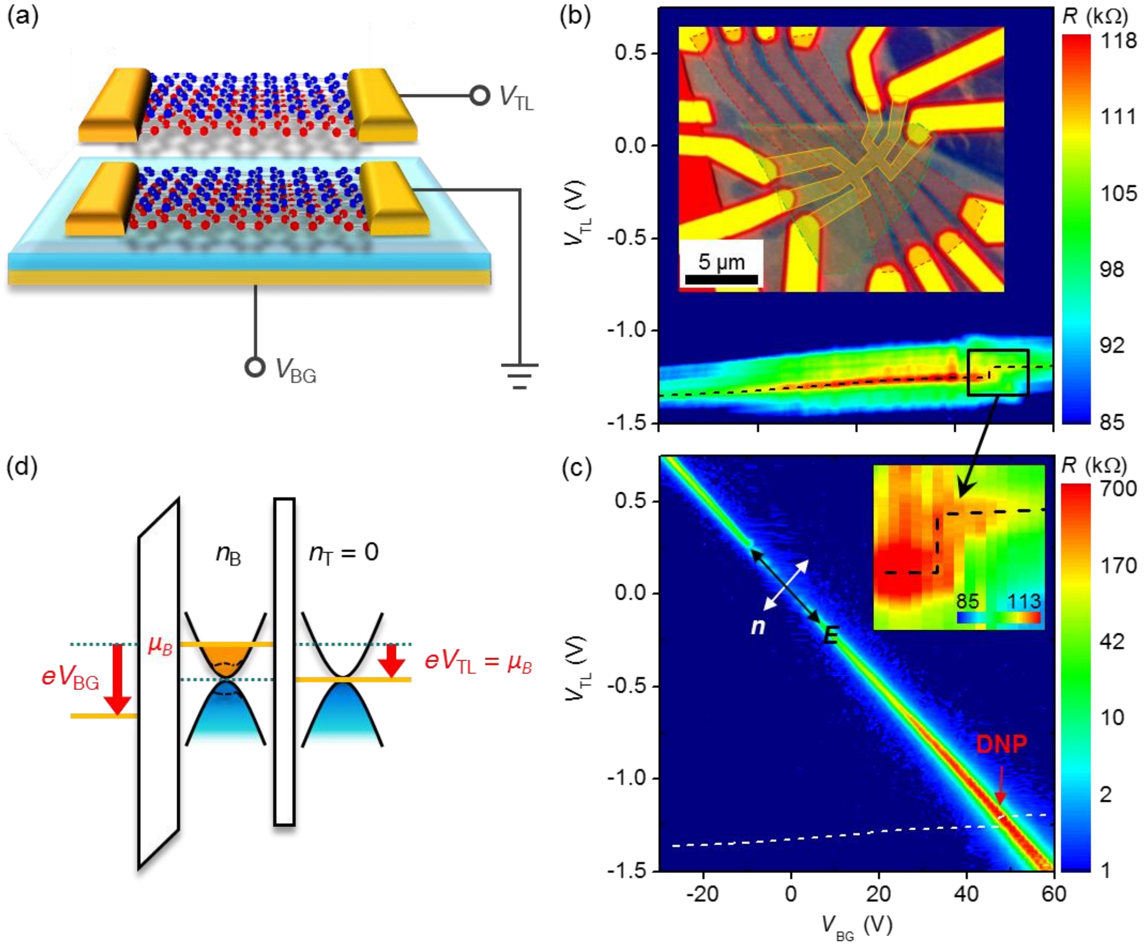

Figure 2.8: Sample schematic and characterization. (a) Schematic representation of the double bilayer heterostructure. (b, c) Top (panel b), and bottom (panel c) layer resistances (R) measured as a function of V_{TL} and V_{BG}. Panel b inset shows a false color optical micrograph of the device. The dashed yellow (dashed red) contour marks the top (bottom) layer; the dashed green line marks the interlayer hBN perimeter. Panel c inset shows a magnified view of the top layer charge neutrality line near the double neutrality point. (d) Energy band profile across the heterostructure with the top layer at charge neutrality.

The bottom bilayer density and resistance dependence on V_{BG} and V_{TL} in Fig. 2.8(c) is similar to that of a dual gated bilayer graphene [36–38], where the charge neutrality point has a linear dependence on V_{BG} and V_{TL}, with a slope controlled by C_{BG} and C_{int}. Along the charge neutrality line of the bottom bilayer, the resistance is minimum at $E = 0$, and increases with the E-field thanks to the E-field induced bandgap in bilayer graphene. By comparison to the bottom bilayer, the top bilayer graphene resistance has a weak dependence on V_{BG} because of the screening by the bottom bilayer, and is controlled primarily by V_{TL}. Interestingly, setting $n_{\mathrm{T}} = 0$ in Eq. 2.2 yields $eV_{\mathrm{TL}} = \mu_{\mathrm{B}}$, which implies that the interlayer bias required to bring the top bilayer to charge neutrality, marked by the dashed lines in Figs. 2.8(b) and 2.8(c) simply represents the chemical potential of the bottom bilayer (Fig. 2.8(d)) in units of eV [35]. Using Eq. 2.1 the n_{B} values along the top bilayer charge neutrality line (dashed lines in Figs. 2.8(b) and 2.8(c)) are given by $n_{\mathrm{B}} = C_{\mathrm{BG}}(V_{\mathrm{BG}} - V_{\mathrm{TL}})/e$. Consequently, the bottom bilayer chemical potential can be fully probed as a function of density.

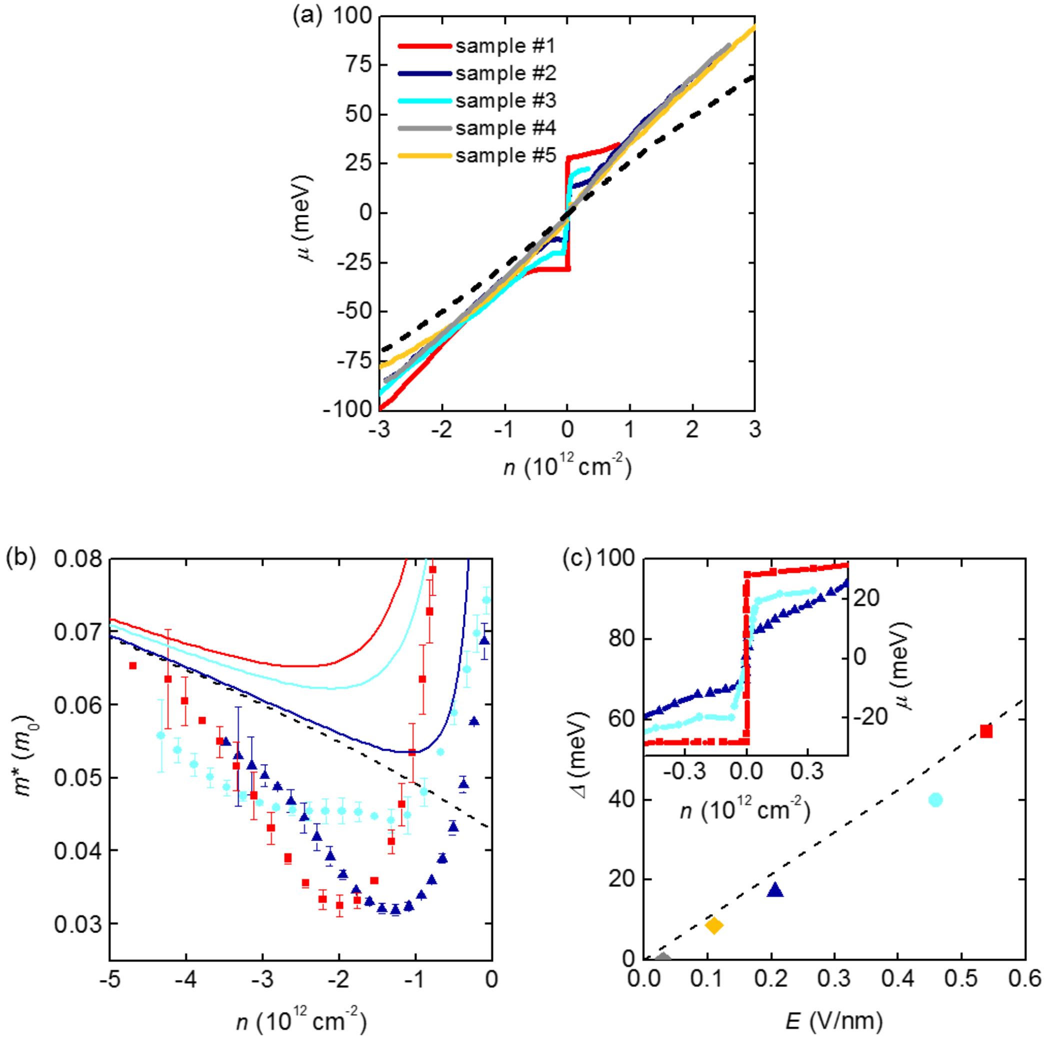

Figure 2.9: (a) Bottom bilayer μ vs. n in samples #1-5. μ vs. n calculated from tight binding approximation using $\upsilon = 8.4\times10^5$ m/s, and $\gamma_1 = 0.34$ eV for $E = 0$ (black dashed) and $E = 0.54$ V/nm (red dashed) are included. (b) Measured (symbols) m^* vs. n. Also included are the m^* vs. n calculated at $E = 0$ (black dashed), 0.54 V/nm (red), 0.21 V/nm (dark blue) and 0.46 V/nm (light blue). (c) Measured (symbols) and calculated [39] (dashed line) Δ values vs. E-field. The inset shows a magnified view of the μ vs. n near charge neutrality.

Figure 2.9(a) shows the bottom bilayer chemical potential (μ) vs. density (n) determined as described above. The finite doping in the top bilayer at $V_{TL} = V_{BG} = 0$ V in our samples leads to a finite E-field across the bottom bilayer at the DNP: 0.54, 0.21, 0.46, 0.03, and 0.11 V/nm for samples #1, #2, #3, #4, and #5, respectively. The μ vs. n for the lowest energy band in bilayer graphene calculated within a tight binding approximation [5] for $E = 0$ and $E = 0.54$ V/nm are included for comparison, using a non-interacting in-plane velocity $\upsilon = 8.4\times10^5$ m/s, and inter-layer hopping $\gamma_1 = 0.34$ eV [39]; the most recent experimental studies indicate a non-interacting Fermi velocity $\upsilon_{F0} = 8.5\times10^5$ m/s [39–41] in monolayer graphene, and $\gamma_1 = 0.38$ eV [42] in bilayer graphene, which is close to $\gamma_1 = 0.36$ eV reported by a recent *ab initio* tight binding model [43] . Here, we neglect trigonal warping, which is relevant only at very low densities. The measured μ values, particularly at high densities, are larger than the band calculations because of the interaction-induced renormalization of electron energies [44] . Moreover, the μ vs. n dependence is nonlinear, evincing a non-parabolic energy momentum dispersion [5,6]. We determine the tight binding hopping parameters, corrected by electron-electron interactions, which is addressed in the following chapter. Figure 2.9(b) shows the effective mass m^* vs. n, extracted from Fig. 2.9(a) data using $m^* = (\pi\hbar^2/2)(d\mu/dn)^{-1}$, $\hbar$ is the reduced Planck's constant. The μ vs. n non-linearity translates into an effective mass with a strong, non-monotonic dependence on density [6,45]. At low densities the measured m^* increases with the transverse E-field, and shows a divergence as a function of n in the proximity of the neutrality point. Note that the bottom bilayer is under a finite *E*-field, and m^* at the band edge increases with the *E*-field as the Mexican hat structure evolves [5].

The measured chemical potential also shows a clear discontinuity as *n* changes its polarity, evincing the *E*-field induced band-gap (Δ) in bilayer graphene [5,6]. Figure 2.9(a) data allow a seamless and accurate extraction of the gap in thermodynamic equilibrium. Figure 2.9(c) shows the measured Δ values, as a function of the *E*-field across the bottom bilayer. The theoretical Δ vs. *E*-field calculated using a tight-binding self-consistent Hartree approach [39] is in a very good agreement with the experimental data.

2.4 Determination of the Tight-binding Coupling Parameters

As addressed in Chapter 1, the electronic structure of bilayer graphene can be captured by the nearest neighbor tight-binding model, where the coupling parameters (Fig. 1.3) impact the spectrum [5,28,46]. The most important parameters are the nearest-neighbor intra-layer A-B hopping amplitude γ_0, which determines the in-plane velocity $\upsilon = -(\sqrt{3}/2)a\gamma_0/\hbar$ in monolayer graphene, a = 2.46 Å is the lattice constant of graphene, and the nearest-neighbor inter-layer coupling γ_1 in a $\widetilde{\mathrm{A}}$-B dimer. Neglecting other parameters except for these strongest γ_0 and γ_1 (minimal tight-binding model of bilayer graphene), the energy vs momentum (p) dispersion is approximated to the simple parabolic dispersion $\mu \approx p^2/2m^*$ at near zero energy, where $m^* = \gamma_1/2\upsilon^2$ is the effective mass [5].

The dashed blue line in Fig. 2.10 represents the measured chemical potential in sample #4, in which the *E*-field induced gap is negligible, whereas the black line shows the μ vs. n calculated within the minimal tight-binding model only using non-interacting $\gamma_0 = -2.61$ eV ($\upsilon = 8.45 \cdot 10^6$ m/s) and $\gamma_1 = 0.361$ eV, the values from the recent local density approximation (LDA) for bilayer graphene [43], to compare with the measured data. First, we note that the measured μ vs. n data are larger than the minimal model calculation in the entire presented range. Tight-binding model basically computes the single electron energy, without many-body considerations. By contrast, the additional energy associated with electron-electron interactions reshape the electronic structure as noted in the experimental data. The interaction driven electron energy increase leads to the reduced m^*, and enhanced Fermi velocity, compared to the non-interacting values. The density dependent Fermi velocity renormalization is reported in monolayer graphene [40,41,47], and reduced m^* is observed in bilayer graphene from temperature dependent Shubnikov–de Haas measurements [6,45].

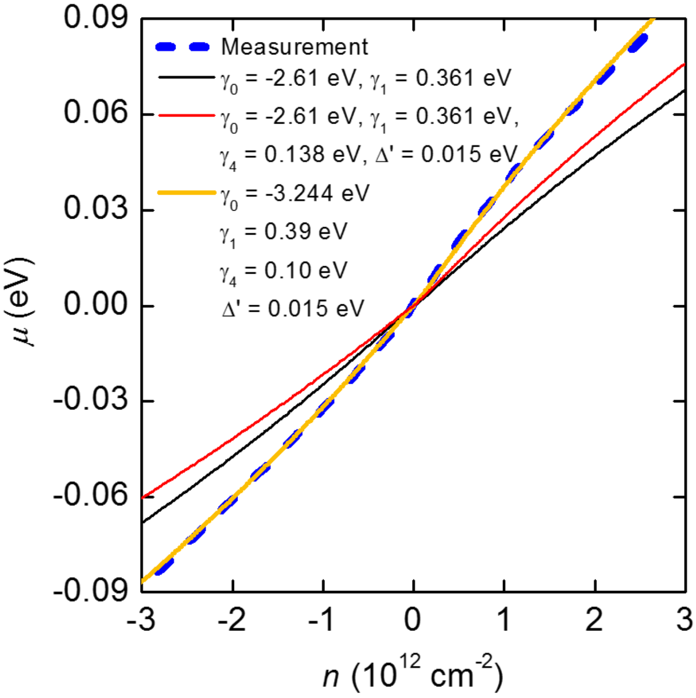

Figure 2.10: Chemical potential dependence on carrier density in bilayer graphene. (dashed blue) μ vs. n measured in our double bilayer graphene heterostructures sample #4. (black) The minimal tight binding model for $E = 0$ using non-interacting $\gamma_0 = -2.61$ eV ($\upsilon = 8.45 \cdot 10^6$ m/s) and $\gamma_1 = 0.361$ eV, and (red) the calculation using non-interacting $\gamma_0 = -2.61$ eV ($\upsilon = 8.45 \cdot 10^6$ m/s), $\gamma_1 = 0.361$ eV, and additional $\gamma_4 = 0.138$ eV. (yellow) The tight binding calculation fitted to our experimental μ vs. n data using $\gamma_0 = -3.244$ eV ($\upsilon = 1.05 \cdot 10^6$ m/s), $\gamma_1 = 0.39$ eV, and $\gamma_4 = 0.12$ eV, in great agreement with our measurement.

Second, in the minimal tight-binding model (the black line in Fig. 2.10) the conduction and valence bands are identical except for the opposite polarities of μ and n, whereas the probed chemical potential reveals an electron-hole asymmetry. Indeed, the measured chemical potential in the conduction band increases faster as a function of carrier density by comparison to the valence band. The electron-hole asymmetric dispersion in bilayer graphene originates from the hopping amplitude γ_4 in either A-$\widetilde{\mathrm{A}}$ or B-$\widetilde{\mathrm{B}}$ [28]. To illustrate the effect of γ_4 on the asymmetry, the calculated μ vs. n including $\gamma_4 = 0.138$ eV (the red line in Fig. 2.10), added to the minimal tight-binding model using $\gamma_0 = -2.61$ eV and $\gamma_1 = 0.361$ eV, values from LDA [43] is provided in Fig. 2.10. This shows that $|\mu|$ calculated including γ_4 (the red trace) is higher than the minimal tight-binding model without γ_4 (the black trace) in the conduction band, whereas $|\mu|$ calculated including γ_4 (the red trace) is smaller than the calculation without γ_4 (the black trace) in the valence band.

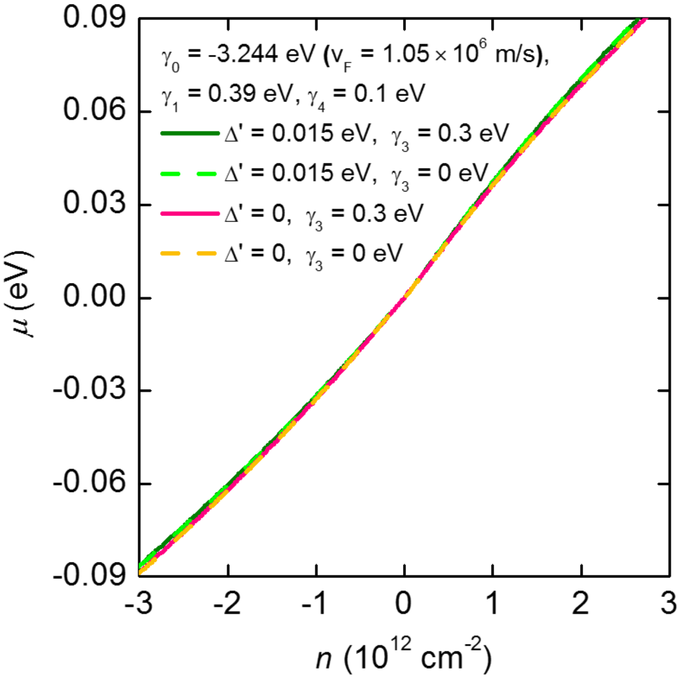

Figure 2.11: The effect of γ_3 and Δ' on the tight-binding calculations. γ_3 does not make any impact on the μ vs. n dispersion in the presented μ and n ranges. Δ' adds a little correction to the dispersion, and we use Δ' = 0.015 eV for fitting, a value from LDA [43].

The interaction induced reduced m^* effectively leads γ_1/υ^2 (in other words, γ_1/γ_0^2) to decrease because $m^* \approx \gamma_1/2\upsilon^2$. By fitting the tight-binding calculations to our measured μ vs. n data, the ratio between γ_1 and γ_0^2, as well as γ_4 can be found. With υ (γ_0) fixed in a range between 1.02×10^6 and 1.1×10^6 m/s, we first determine the values of γ_1 by fitting the tight-binding calculations using γ_1 as the fitting parameter, and then add γ_4 to capture the electron-hole asymmetry. The yellow line in Fig. 2.10 shows the representative fitted tight-binding μ vs. n calculation using $\gamma_0 = -3.244$ eV ($\upsilon = 1.05 \cdot 10^6$ m/s), $\gamma_1 = 0.39$ eV, $\gamma_4 = 0.10$ eV, and $\Delta' = 0.015$ eV, in excellent agreement with our measurement, where Δ' describes the on-site energy difference in sublattices (A and B), which is fixed as suggested by LDA in Ref. [43] in our fitting here. This choice of parameters is not unique for the best fit to the measured μ vs. n dispersion because the ratio between γ_1 and γ_0^2 determines the dispersion. We neglect another parameter γ_3, which describes A-$\widetilde{\mathrm{B}}$ inter-layer hopping and produces the trigonal warping in the range of several meV, too small to be resolved within our measurements. Figure 2.11 shows the effect of γ_3 and Δ' on the tight-binding calculations; γ_3 does not induce any impact on the calculations in the range of our interest, while Δ' adds a little correction to the calculations.

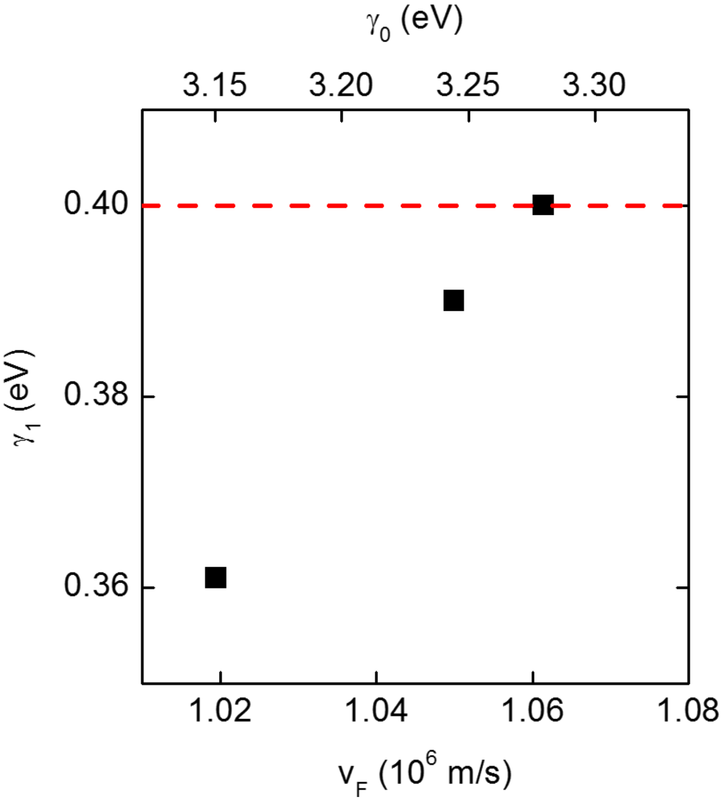

Figure 2.12: Fitted results of γ_1 as a function of υ^2. The presented γ_1 and υ^2 values along with $\gamma_4 = 0.1 - 0.12$ eV provide the tight-binding calculations in excellent agreement to our measured μ vs. n.

Figure 2.12 shows the fitting results of γ_1 as a function of υ (lower x-axis) and γ_0 (upper x-axis). $\upsilon = 1.02 - 1.06 \cdot 10^6$ m/s, coupled with $\gamma_1 = 0.36 - 0.4$ eV as presented in Fig. 2.12 provide near identical tight-binding calculations in the μ and n ranges of our interest, all of which coincide with the experimental data. In literatures the values for γ_1 range between 0.3 eV [48] and 0.4 eV [49,50], with the most recent experimental study suggesting $\gamma_1 = 0.38$ eV [42]. As shown in Fig. 2.12, $\upsilon > 1.06 \times 10^6$ m/s requires $\gamma_1 > 0.4$ eV, which is beyond the reasonable value for γ_1, and thus excluded here. The recent experimental study shows the average interacting Fermi velocity $\upsilon = 1.05 \times 10^6$ m/s in monolayer graphene [40], a constant velocity value fitted for their quantum capacitance measurement data in the density range from -5×10^{12} to 5×10^{12} cm^{-2}. For $\upsilon = 1.05 \times 10^6$ m/s, we obtain $\gamma_1 = 0.39$ eV (the yellow line in Fig. 2.10), which is in agreement with the value reported in infrared spectroscopy [42].

	Graphite Ref. [25]	Bilayer Ref. [43]	Bilayer Ref. [48]	Bilayer Ref. [49]	Bilayer Ref. [42]	Monolayer Ref. [40]
	LDA	LDA	Raman	Infrared spectroscopy	Infrared spectroscopy	Capacitance measurement
γ_0	−2.598	−2.61	−2.9	−3.0	−3.16	−3.244
γ_1	0.377	0.361	0.3	0.40	0.381	
γ_3	0.319	0.283	0.10	0.3	0.38	
γ_4	0.177	0.138	0.12	0.15	0.14	
Δ'	0.024	0.015		0.018	0.022	

Table 2.2: Tight-binding model coupling parameters from theoretical LDA calculations for graphite [25] and bilayer graphene [43], Raman [48] and infrared [42,49] measurements in bilayer graphene, and capacitance measurements in monolayer graphene [40].

Our clearly revealed electron-hole asymmetry allows the hopping parameter γ_4 also to be extracted from transport measurements for the first time. We extract $\gamma_4 = 0.1 \pm 0.01$ eV, values comparable to those suggested from the optical measurements [42,50]. Table 2.2 shows the tight-binding coupling parameters from multiple reports. Note that the electron-electron interaction is not took into account in the LDA calculations, which provide lower γ_0 than the values from experiments in Ref. [42,48,49]. Our non-local transport spectroscopic technique is similar to other spectroscopy through scanning single-electron transistor [22], scanning tunneling microscopy [51], or capacitance measurements [40]. However there have been no detailed studies in electronic structure of bilayer graphene through these methods, except for the local density of state measurement [52]. Optical measurements such as Raman scattering and infrared spectroscopy provide electronic structure information in bilayer graphene [42,48,49], but these methods may not probe the energy-momentum dispersion in equilibrium.

The fitted results of the coupling parameters found from the zero gap bilayer graphene chemical potential are also applied to when there is a gap. Figure 2.13 represents the measured chemical potential in sample #2 (dashed blue), which has a band gap of ~ 27 meV, along with the tight-binding calculation using $\gamma_0 = -3.244$ eV ($\upsilon = 1.05 \cdot 10^6$ m/s), $\gamma_1 = 0.39$ eV, $\gamma_4 = 0.1$ eV, $\Delta' = 0.015$ eV, and a band gap of 27 meV. The calculated μ vs. n dispersion using the parameters found for the zero gap chemical potential, accompanied with the additional gap shows a good agreement with the experimental data.

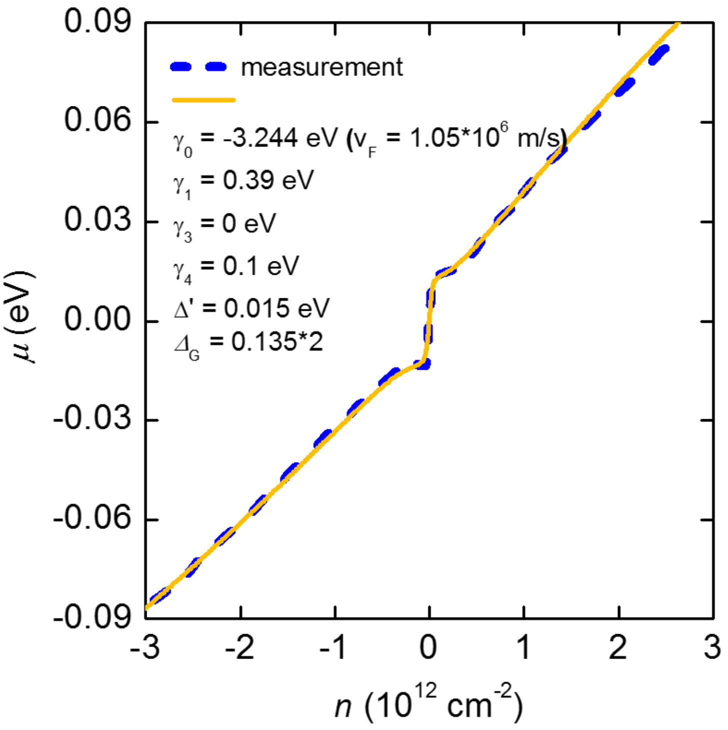

Figure 2.13: The measured chemical potential in sample #2 (dashed blue), which has a band gap of ~ 27 meV, along with the tight-binding calculation using $\gamma_0 = -3.244$ eV ($\upsilon = 1.05 \cdot 10^6$ m/s), $\gamma_1 = 0.39$ eV, $\gamma_4 = 0.1$ eV, $\Delta' = 0.015$ eV, and a band gap of 27 meV, which is in a good agreement with the experimental data.

2.5 Quantum Hall Ferromagnetism in Bilayer Graphene

We now turn to bilayer graphene in high magnetic fields. Figure 2.14(a) shows the longitudinal resistivity (ρ_{xx}) measured as a function of V_{BG} and V_{TL} in a perpendicular magnetic field $B = 14$ T, in sample #1. The clear ρ_{xx} minima reveal QHSs at all integer filling factors (ν) up to $\nu = 15$; the $\nu = 0$ QHS is marked by a ρ_{xx} maximum. The four fold, spin and valley LL degeneracy is lifted by interaction-enhanced Zeeman splitting [8], and the *E*-field induced layer (valley) degeneracy lifting [5–7]. The QHSs stabilized by the spin and valley degeneracy lifting, i.e. $\nu \neq \pm4, \pm8, \pm12$, etc… undergo transitions at finite *E*-field values as a result of the interplay between the LL spin and valley splitting. Specifically, the $\nu = -1, -3, -5, -7, -9, -11$ (odd filling) QHSs are absent at $E = 0$, and emerge as an *E*-field is applied. By contrast, the half fillings $\nu = 0, -6, -10, -14$ of the spin- and valley-degenerate LLs are present at $E = 0$, and collapse at finite *E*-field values. The interplay between the spin and valley splitting explains the transitions at $\nu = -6, -10, -14$ at a finite *E*-field (Fig. 2.14(a)).

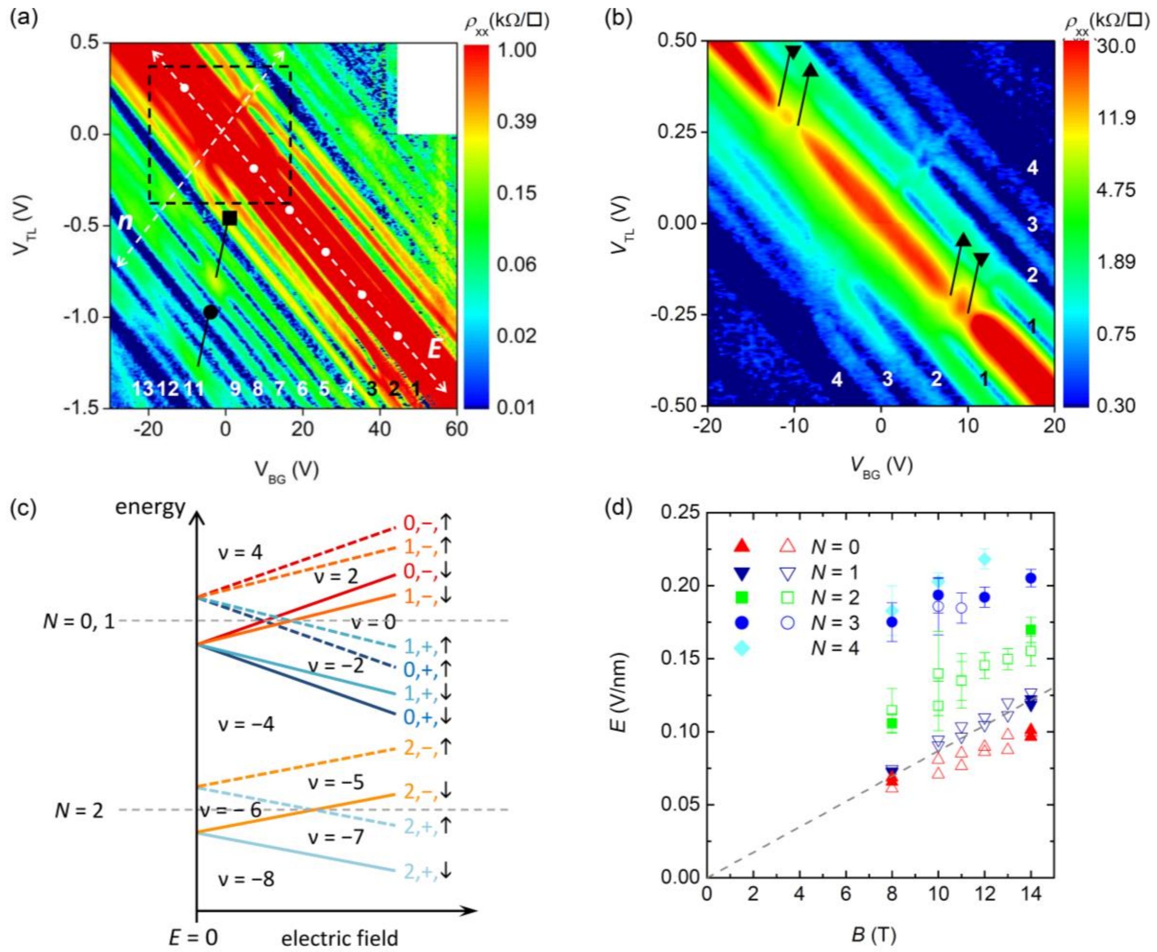

Figure 2.14: Bilayer graphene quantum Hall ferromagnetism. (a) The bottom layer resistivity ρ_{xx} as a function of V_{TL} and V_{BG}, at $B = 14$ T and $T = 1.4$ K in sample #1. The dashed white lines mark the $n = 0$ and $E = 0$ axes; the dots along the $n = 0$ axis mark E-field increments of 0.1 V/nm. The E-field controlled spin-to-valley polarization transitions in the $N = 2$ (square), and $N = 3$ (circle) LLs are marked in the figure. (b) Magnified view of the dashed line rectangle of panel (a). The triangles mark two distinct transitions of the $\nu = 0$ QHS as a function of E -field. (c) Schematic representation of the LL evolution with E-field, and the ensuing QHSs. The solid (dashed) line marks the spin down (up) levels. The orbital index, and layer (+, –) degrees of freedoms are color coded. Assuming the direction of the applied E-field favors energetically the occupation of the bottom layer, the symbols +, – mark the bottom and top layers, respectively. (d) E-field vs. B at which QHS residing in different orbital LLs undergo spin-to-valley polarized transitions in sample #1 (filled symbols), and #2 (open symbols). The $N = 0$, 1 transitions are defined using panel (c) LL diagram.

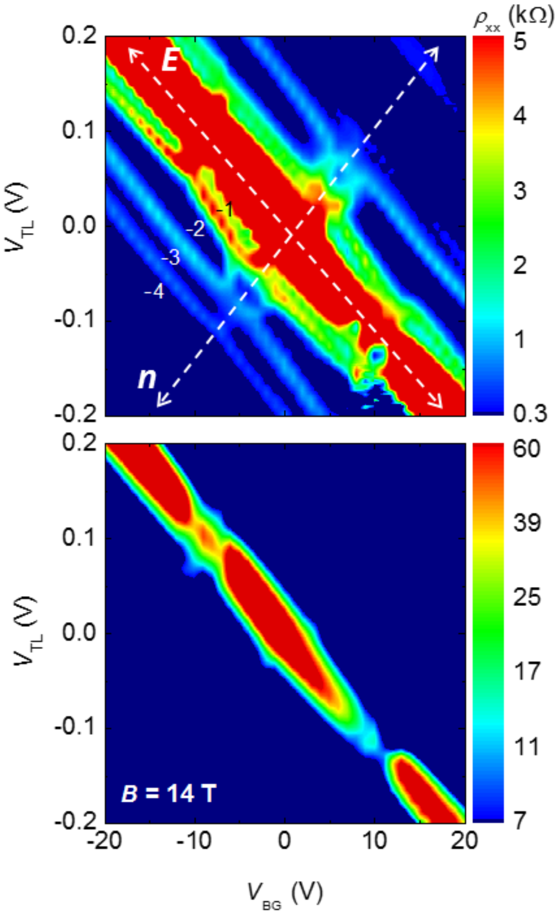

Figure 2.15: Contour plot of the bottom layer resistivity ρ_{xx} as a function of V_{TL} and V_{BG}, measured at B = 14 T and T = 1.4 K in sample #2. Upper and lower panels show the same data, but in different ranges to better illustrate the evolution of ν = −1, −2, −3 QHSs (upper panel), and the insulating ν = 0 QHS (lower panel) as a function of E-field. QHSs at integer filling factor ν = −1, −2, −3 are marked by local ρ_{xx} minima (upper panel), and the QHS at ν = 0 is marked by a ρ_{xx} maximum (lower panel). The dashed white lines in the upper plot represent the n = 0, and E = 0 axes.

Figure 2.14(b), a magnified view of dashed rectangle in Fig. 2.14(a), and the lower panel of Fig. 2.15 shows a strong $\nu = 0$ QHS at $E = 0$, as well as at high E-field, marked by diverging ρ_{xx}, consistent with previous experimental reports [37,38]. Theoretical considerations [9], substantiated by recent experimental data [53] indicate that the insulating $\nu = 0$ QHS in the proximity of $E = 0$ is described by a canted antiferromagnetic (CAF) ground state, where electrons in different valleys have opposite in-plane spin orientation and a net out-of-plane spin polarization, while the $\nu = 0$ state at high E-field is valley (layer) polarized. Surprisingly, as a function of E-field the insulating ρ_{xx} at $\nu = 0$ collapses at *two* distinct E-field values, rather than one [37,38], indicating two distinct transitions and the observation of an intermediate phase in between the CAF and layer-polarized phases. The QHS transitions evinced by Fig. 2.14(a) and 2.14(b) data can be qualitatively understood using the LL energy diagram shown in Fig. 2.14(c), based on tight-binding theoretical considerations [5]. In this picture, the energies of LL with orbital index $N = 0, 1$ have a different dependence on the E-field, which explains the two distinct transitions at $\nu = 0$, as well as the emergence of $\nu = \pm 1$ and ± 3 QHSs at a finite E-field. When electron-electron interactions are included [1], more subtle phase transitions are expected for the $N = 0, 1$ QHSs (see phase diagram in Fig. 2.16) ; the intermediate $\nu = 0$ QHS between the CAF and layer-polarized phases is found to be spin-layer coherent phase (SL_0 phase in Fig. 2.16), where LLs with the same orbital index but different spin and valley degrees of freedom, e.g. solid red (orange) and dashed dark (light) blue LLs in Fig. 2.14(c) form a coherent superposition. In the single-particle picture, at $\nu = 0$, electrons in the $N = 0$, spin down, top-layer LL (solid red line in Fig. 2.14(c)) should move to the $N = 0$, spin up, bottom-layer LL (dashed dark blue in Fig. 2.14(c)) at a finite E-field by changing both spin and valley orientations, while retaining the orbital index. Instead of this definite alteration from one to another different quantum state, the many-body Hartree-Fock formalism predicts electrons favor a coherent superposition (SL_0 phase in Fig. 2.16) of the two quantum states at the transition between the two incoherent CAF (I_0 phase) and layer-polarized phases (I_0^* phase).

The interplay between the spin splitting and the E-field induced valley (layer) splitting at $N = 2$ depicted in Fig. 2.14(c) explains the absence of $\nu = -5$ and -7 QHSs at $E = 0$, their emergence with the applied E-field, as well as the spin-to-valley polarized phase transition at $\nu = -6$ at a finite E-field (Fig. 2.14(a)). Similar phase transitions are observed at $\nu = -10$ and -14, half-filled LL QHSs.

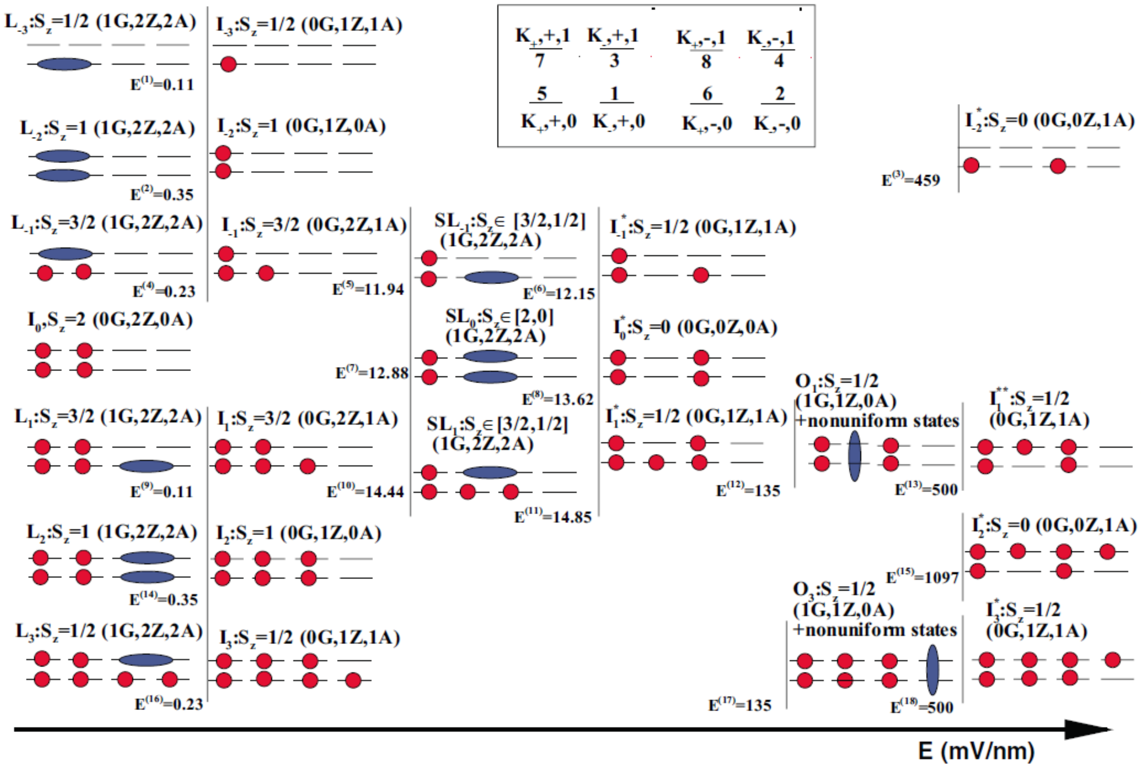

Figure 2.16: Phase diagram of the chiral two-dimensional electron gas in Landau level $N = 0$ at $B = 10$ T and for $\kappa = 5$ as a function of the transverse electric field between the layers for integer filling factors $\nu = -3, -2, -1, 0, 1, 2, 3$ (from top to bottom). A filled (red) circle represents a filled state, while a filled (blue) ellipse indicates a coherent superposition of two levels. The numbering of the levels is indicated in the inset at the top right of the figure. The $E^{(i)}$'s indicate the critical perpendicular electric field (in mV/nm) required for the transition between two phases. Also indicated for each phase are the spin polarization S_z, the number of Goldstone mode (G), of modes gapped at the Zeeman energy (Z), and the number of peaks in the optical absorption spectrum (A). The figure and caption are adapted from [1].

A noteworthy exception from this single-particle picture is the evolution of the ν = ±2 QHSs, which are present at $E = 0$, vanish at a relatively small E-field, and then reemerge (Fig. 2.14(b) and Fig. 2.15 upper panel). These ν = ±2 QHSs at $E = 0$ can be explained as layer-coherent QHSs ($L_{\pm 2}$ phase in Fig. 2.16), where the LLs with the same orbital index and spin orientation but different layer (valley) degrees of freedom, e.g. dashed red (orange) and dashed dark (light) blue LLs of Fig. 2.14(c) form a coherent superposition thanks to the exchange interaction [1]. At a finite E-field the different on-site energies in different layers lead to incoherent ν = ±2 phases with a zero in-plane and a net out-of-plane spin polarization ($I_{\pm 2}$ phase in Fig. 2.16).

Figure 2.14(d) summarizes the critical E-field values at which half filled LL QHSs undergo the spin-to-valley polarized phase transitions discussed above. The E-field values are calculated using Eq. (2.3), and including the layer Fermi energies. Because the $N = 0$, 1 LL wave-functions in different valleys are fully layer polarized [5] we use for comparison the internal electric field in a layer polarized ν = 0 QHS, $E_{int} = 4(e^2B/h)/2\varepsilon_0$ (dashed line) [38]. The critical E-field values at which the LLs become layer polarized are comparable to E_{int} for $N = 0$ and $N = 1$, and increase for higher N as higher LL wave-functions have a reduced layer polarization by comparison to $N = 0$, 1 [7].

Figure 2.17 shows the emergence of the integer QHSs as a function of B-field. The layer-coherent $\nu = \pm 2$ QHSs at $E = 0$ (top row in Fig. 2.17) and the spin-layer coherent $\nu = 0$ QHS at finite E-fields (bottom row in Fig. 2.17) start to emerge at around 11 T. As the B-field increases, the symmetry broken integer QHSs become more evident, and $\nu = \pm 2$ QHSs are more clearly developed than $\nu = \pm 1, \pm 3$ QHSs, because of larger gaps at $\nu = \pm 2$ than those at $\nu = \pm 1, \pm 3$, discussed in the following in detail. B = 14 T was the highest B-field we applied here, and fractional QHSs are also expected to be observed at B-field higher than 20 T.

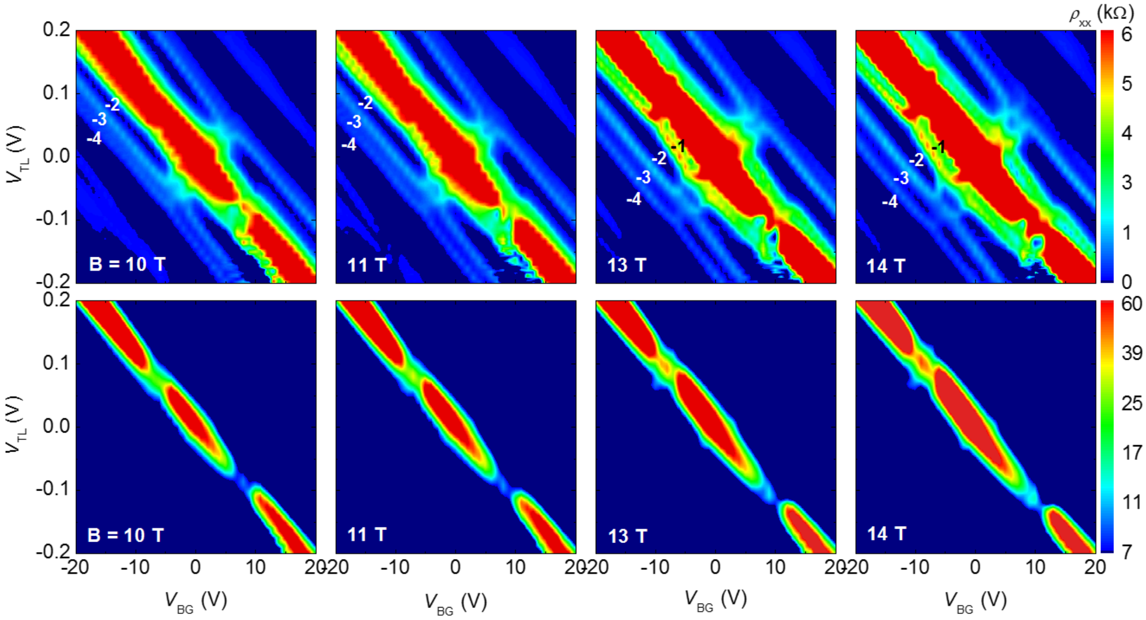

Figure 2.17: Contour plots of the bottom bilayer resistivity ρ_{xx} as a function of V_{TL} and V_{BG}, measured at B = 10, 11, 13, 14 T and T = 1.4 K in sample #2. Upper and lower panels show the same data, but in different ranges to better identify the evolution of integer QHSs (upper panel), and the insulating $\nu = 0$ QHS (lower panel). The QHSs become more evident at higher B-field.

2.6 Mapping the LL Energies in Bilayer Graphene at High Magnetic Fields

2.6.1 LL Energies in Bilayer Graphene at High Transverse *E*-fields

Through the chemical potential mapping technique discussed above, we determine the LL energies in bilayer graphene as a function of filling factor and magnetic field. Figure 2.18(a) shows the bottom bilayer ρ_{xx} measured at B = 12 T, with the top bilayer charge neutrality line transposed on the contour plot (white line). Note that the transverse *E*-field across the bottom bilayer at DNP is 0.54 and 0.21 V/nm for sample #1 and #2 respectively, values higher than the N = 1 LL critical *E*-field. Therefore, along the top bilayer charge neutrality line, the bottom bilayer $\nu = 0$ QHS is layer polarized. At each integer filling of the bottom bilayer, the top bilayer neutrality line displays an abrupt change in the V_{TL} value, which translates into a chemical potential jump in bottom bilayer. The staircases-like discontinuity, particularly sharp at the bottom bilayer $\nu = 0$, −4, −8, −12, −16 testifies to a reduced LL broadening, in contrast to previous measurement in double monolayer graphene heterostructures using metal oxide as an interlayer dielectric [35].

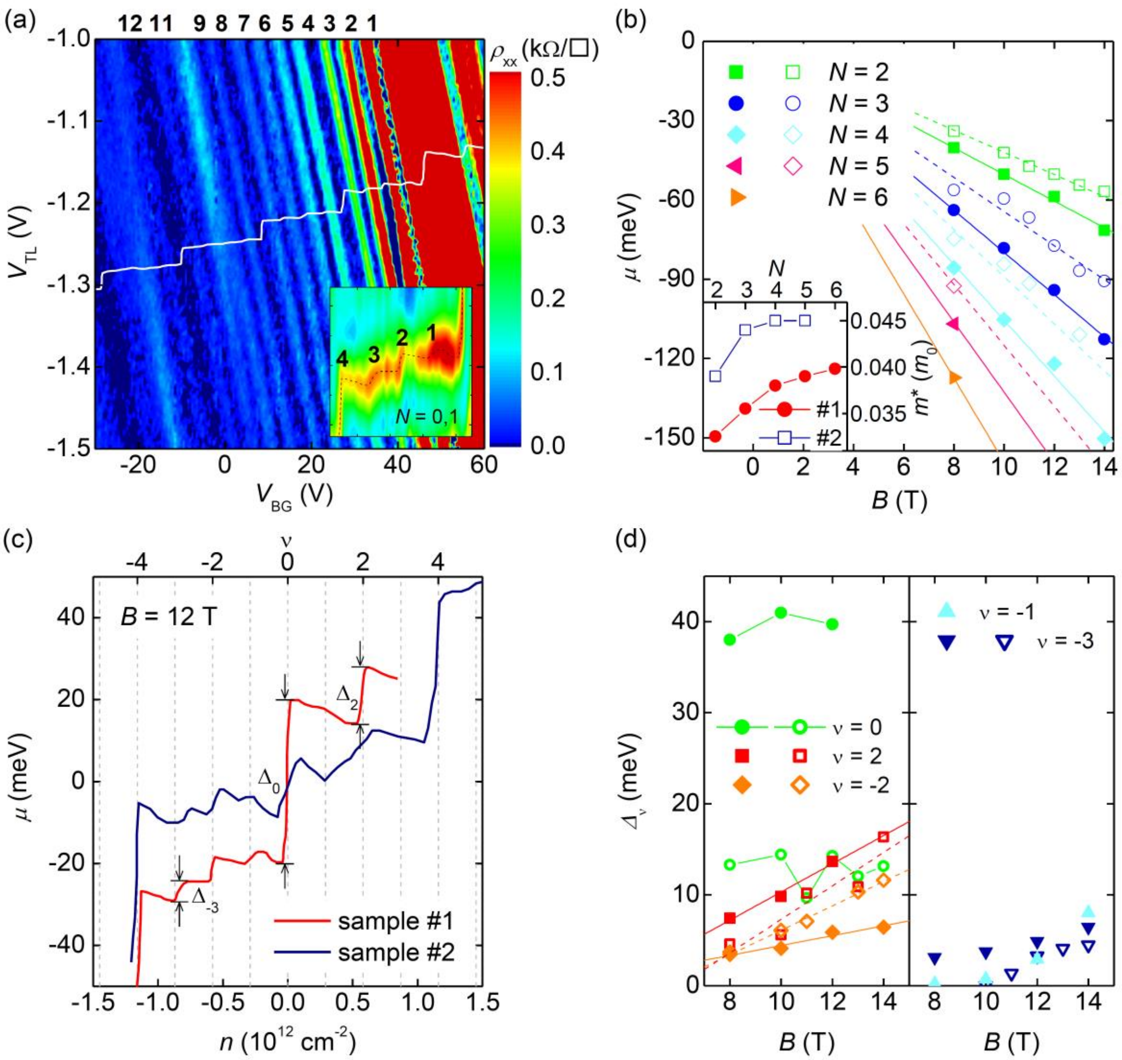

Figure 2.18: Landau level energies and broken symmetry gaps in bilayer graphene. (a) The bottom layer resistivity ρ_{xx} as a function of V_{TL} and V_{BG} at $B = 12$ T and $T = 1.5$ K in sample #1, along with the top layer charge neutrality locus (white line) transposed on the contour plot. The top axis shows the QHS filling factors. The inset shows the top layer resistance as a function of V_{TL} and V_{BG}, as the top layer charge neutrality line crosses the $\nu = 0, -1, -2, -3, -4$ QHSs of the bottom layer. (b) Orbital LL energies as a function of B-field and LL index in samples #1 (filled symbols) and #2 (open symbols). The inset shows the m^* vs. N extracted from the main panel data. (c) Bottom bilayer μ vs. n (bottom axis) and ν (top axis) at $B = 12$ T. (d) QHS gaps at $\nu = 2, 0, -1, -2, -3$ in sample #1 (filled symbols) and #2 (open symbols).

Figure 2.18(b) shows the LL orbital energies as a function of B-field and LL index, determined from the chemical potential at the half filling of each LL orbital index. As an example, on the bottom bilayer ρ_{xx} contour map at $B = 8$ T (Fig. 2.19), with the top bilayer charge neutrality line (white line) superposed on the plot, the points at the half fillings of $N = 2, 3, 4, 5, 6$ LLs (red dots) are marked on the top bilayer charge neutrality line, where the LL orbital energies are measured as guided by the black dashed lines. The LL orbital energies increase linearly with magnetic field, consistent with the theoretical $\mu = \hbar\omega_c\sqrt{N(N-1)}$ dependence [5]; here $\omega_c = eB/m^*$ is the cyclotron frequency. The inset of Fig. 2.18(b) shows the m^* vs. N dependence determined from the slope of μ vs. B at each LL. The m^* increases with the LL index, similar to the observation at $B = 0$ T (Fig. 2.9(b)).

A closer look at the chemical potential of $N = 0, 1$ LL, shown in Fig. 2.18(a) inset and Fig. 2.18(c), reveals chemical potential jumps at integer fillings $\nu = 2, 0, -1, -2$, and -3, as well as a *decreasing* chemical potential vs. filling factor (density) in the proximity of the QHSs stabilized in the $N = 0, 1$ LLs. The decreasing μ vs. n dependence observed in the proximity of QHSs, while counter-intuitive in a single particle picture stems from a strong exchange interaction, and translates into a negative compressibility of the electron system [54]. A similar observation has been reported in monolayer graphene, where the chemical potential was probed through capacitance measurements [40].

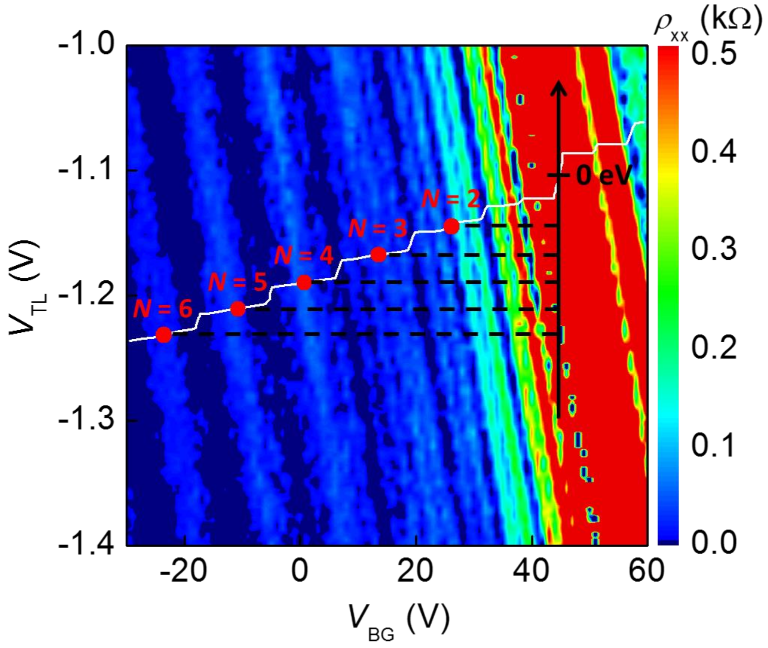

Figure 2.19: ρ_{xx} as a function of V_{TL} and V_{BG} at B = 8 T and T = 1.5 K in sample #1, along with the locus of top bilayer charge neutrality (white line) on the contour plot. On the top bilayer charge neutrality line, which directly represents the LL energies in unit of eV, the half filling point for each LL orbital index is marked (red dot), where the average LL orbital energy is measured, as guided by the black dashed lines.

Using the chemical potential jump at integer fillings, we determine the broken symmetry QHS gaps (Δ_ν) at filling factors ν = −3, −2, −1, 0, 2, as a function of *B*-field, shown in Fig. 2.18(d). Our method to quantify the gap is different from the activation energies determined from the resistivity temperature dependence [55,56], which tends to underestimate the gaps, and is similar to spectroscopic techniques through scanning single-electron transistor [22], scanning probe microscopy [51], or capacitance measurements [40]. However, unlike these latter techniques the measurement discussed here allow control of both density and transverse electric field in the electron system investigated.

We note that the measured Δ_0 is independent of *B*-field. These observations maybe appear to contrast to the linear *B*-field dependence of Δ_0 observed in single-gated bilayer graphene [22,56], however the data in Fig. 2.18(d) represent the ν = 0 gap in the layer polarized phase, whereas Ref. [22,56] probe Δ_0 in the CAF phase. The layer polarized Δ_0 is controlled by the interaction and Zeeman splitting, as well as the *E*-field-induced on-site energy difference. At moderate *E*-fields in the layer polarized ν = 0 phase, the single-particle picture suggests the gap decreases with the *B*-field (see the single-particle LL diagram in Fig. 2.14(c)), and therefore the interaction induced $\propto \sqrt{B}$ dependence is weakened, leading to a Δ_0 weakly dependent on *B*-field and mainly controlled by the *E*-field [1]. This explains the larger (smaller) Δ_0 value in sample #1 (#2), due to the larger (smaller) bottom bilayer *E*-field near the DNP. The Hartree-Fock gaps at ν = 0 as suggested by Ref. [1] are also provided in Fig. 2.20 for comparison.

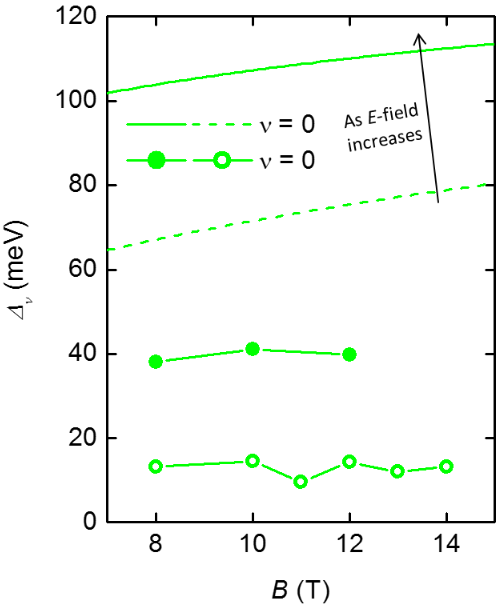

Figure 2.20: Theoretically calculated QHS gaps at ν = 0 as a function of *B*-field [8] at transverse electric fields of 0.54 V/nm (solid line) and 0.21 V/nm (dashed line), which are the *E*-field at DNP in samples #1 and #2, respectively. The symbols are our experimental values, the same as data in Fig. 2.18(d).

The gaps of ν = −3, −1, ±2 have a linear dependence on the *B*-field, a trend similar to results obtained in single-gated suspended bilayer graphene [22]. We compare our experimental data to the values theoretically calculated as suggested by Ref. [1] for two different *E*-field values of 0.54 V/nm (thin solid lines) and 0.21 V/nm meV (thin dashed lines), which are the *E*-field at DNP in samples #1 and #2 respectively, in Fig. 2.21. While theoretical considerations [1,8] suggest a sublinear *B*-field dependence associated with the $\propto\sqrt{B}$ of the interaction energy, the non-linearity is weak particularly in the *B*-field range probed here. Furthermore, the broken symmetry QHSs observed in the N = 0, 1 LLs show a marked electron-hole asymmetry.

Specifically, Δ_2 is larger than Δ_{-2} for both samples #1 and #2, while ν = −1 and −3 have gaps larger than those of ν = 1 and 3, which are too small to be resolved experimentally. The experimentally observed electron-hole asymmetry is consistent with a detailed Hartree-Fock calculations [1] in the broken symmetry QHS gaps, as provided in Fig. 2.21. The calculation also suggests Δ_2 (Δ_{-2}) to increase (decrease) with an applied *E*-field, in agreement with our measurements which show Δ_2 (Δ_{-2}) is larger (smaller) in sample #1 with respect to sample #2. However, the measured QHS gap values are all smaller than the theoretical results, a common thread in Hartree-Fock considerations.

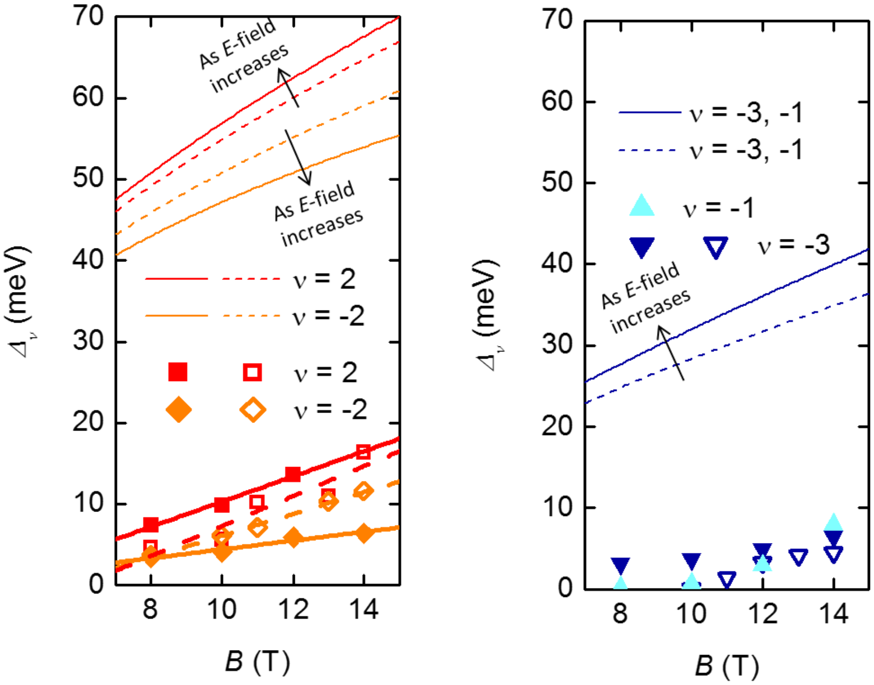

Figure 2.21: Hartree-Fock calculated gap values [1] at ν = ±2 (left panel), −1, −3 (right panel) at the *E*-field of 0.54 V/nm (thin solid line) and 0.21 V/nm (thin dashed line), to compare with the experimental data for sample #1 (filled symbols) and sample #2 (open symbols), respectively.

2.6.2 LL energies in Bilayer Graphene at Small Transverse *E*-fields

For samples #1 and #2, the *E*-field across the bottom bilayer at DNP is 0.54 and 0.21 V/nm, higher than the $N = 1$ LL critical *E*-field, which leads the bottom bilayer $\nu = 0$ QHS at DNP to be layer polarized. By contrast, for samples #4 and #6, the *E*-field in the bottom bilayer at DNP is 0.03 and 0 V/nm, respectively, and therefore the LL energies are probed at relatively smaller *E*-fields. Figure 2.22(a,b) show the contour maps of longitudinal resistances of the bottom (R_{xx}^{B}) and top (R_{xx}^{T}) bilayers, respectively, measured as a function of V_{BG} and V_{TL} at $B = 14$ T in sample #4. The clear R_{xx}^{B} minima display QHSs at all integer fillings up to $\nu = -10$, and the R_{xx}^{B} maximum at charge neutrality reveals the symmetry broken $\nu = 0$ QHS. QHSs are not clearly developed for the electron side, compared to the hole side, and we focus mainly on the hole side QH features here. As observed in samples #1 and #2 (Fig. 2.14 and Fig. 2.15), the four fold, spin, valley (layer), and $N = 0, 1$ orbital degeneracies are lifted by Zeeman splitting [8], and the *E*-field induced on-site energy asymmetry between the two layers [5–7], accompanied with the many-body interactions in graphene. Those broken symmetry QHSs at $\nu \neq -4, -8, \ldots$ show multiple transitions, signifying LL crossing, at finite *E*-field values because of the interplay between the LL spin and valley splitting as a function of the applied *E*-field, also influenced by electron-electron interactions, similarly to Fig. 2.14 and Fig. 2.15 data.

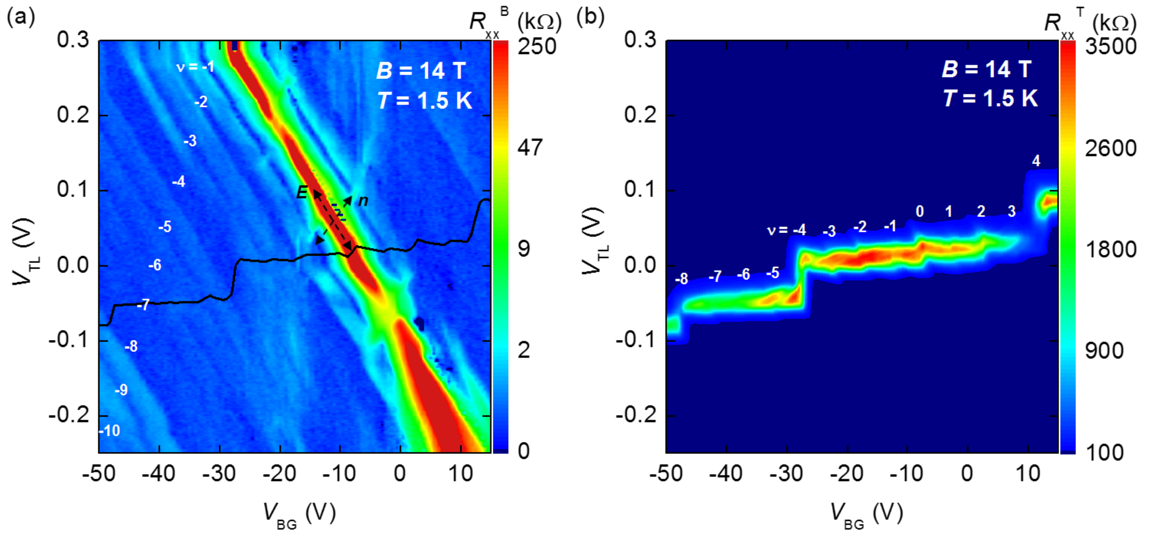

Figure 2.22: (a) The longitudinal bottom bilayer resistance R_{xx}^{B} as a function of V_{TL} and V_{BG}, at $B = 14$ T and $T = 1.5$ K in sample #4. The dashed black arrows mark the $n = 0$ and $E = 0$ axes. Integer filling factors up to −10 are provided on the hole side. The locus of top bilayer charge neutrality (black line) is transposed on the contour map. (b) The longitudinal top bilayer resistance R_{XX}^{T} as a function of V_{TL} and V_{BG} at $B = 14$ T and $T = 1.5$ K in sample #4. The changes of V_{TL} along the charge neutrality line represent the chemical potential change in the bottom bilayer graphene, in unit of eV.

From the clearly developed charge neutrality of the top bilayer (Fig. 2.22(b)), defined as a maximum resistance point at each V_{BG} value, LL energies of the bottom bilayer can be mapped as performed for samples #1 and #2 above. The top bilayer charge neutrality line is superposed on the R_{xx}^B contour plot in Fig. 2.22(a) (black line). The V_{TL} value of the neutrality line shows clear jumps at finite V_{BG} values, where the bottom bilayer QHSs are developed, because V_{TL} is used to move the bottom bilayer chemical potential to the next quantized LL, as discussed in the previous chapter (Fig. 2.18(a)). The large V_{TL} jumps represent the bottom bilayer gaps at $\nu = 4, -4$, and -8, and smaller jumps are also visible at the bottom bilayer $\nu = \pm1, \pm2$, and ±3 gaps.

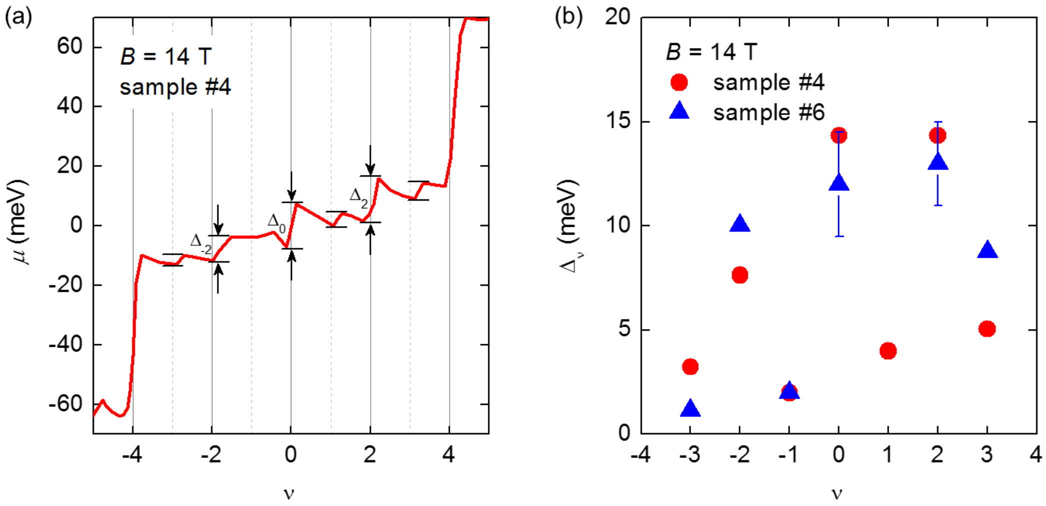

Figure 2.23: (a) Bottom bilayer μ vs. ν (bottom axis), measured in sample #4 at B = 14 T. (b) Integer QHS gaps at $\nu = 2, 0, \pm1, \pm2, \pm3$ in sample #4 (red) and #6 (blue) extracted from the chemical potential jumps as seen in (a).

Figure 2.23(a) shows the bottom bilayer μ (LL energies) as a function of ν, measured from the top bilayer charge neutrality in sample #4, at B = 14 T, and we observe the negative compressibility clearly, as noted in samples #1 and #2. Figure 2.23(b) represents the broken symmetry QHS gaps at ν = 0, ±1, ±2, and ±3, at B = 14 T for samples #4 and #6, extracted from the chemical potential jump at each integer QHS. For samples #4 and #6, we probe the LL energies at relatively low E-field regime, including the spin-polarized ν = 0 QHS, because the top bilayer charge neutrality line (the black line superimposed in the R_{xx}^{B} contour map (Fig. 2.22(a)) passes the low E-field regime of the bottom bilayer, in contrast to samples #1 and #2, in which the LL energies at higher E-fields and the layer-polarized ν = 0 phase were explored.

In the proximity of E = 0, the QH states in the N = 0, 1 LLs are very sensitive to the small changes of E-field because of multiple LL crossing occurring at E = 0, and near the N = 0, 1 critical E-fields, as simply described in the single-electron LL diagram in Fig. 2.24(a). There are additional many-body induced phases at ν = 0 and ν = ±2 (see Ref. [1] and Fig. 2.16), not presented in the single-particle LL diagram. To better display which QH phases are probed (crossed) in the bottom bilayer by the top bilayer charge neutrality in samples #4 and #6, the estimated loci of the top bilayer neutrality lines when the bottom bilayer E-field at DNP is 0.03 and 0 V/nm, which are for samples #4 and #6 respectively, are depicted on a good example of bottom bilayer resistivity contour plot in Fig. 2.24(b), where all the broken symmetry integer QHSs as well as their phase transitions are well presented (the data from sample #2 at B = 14 T).

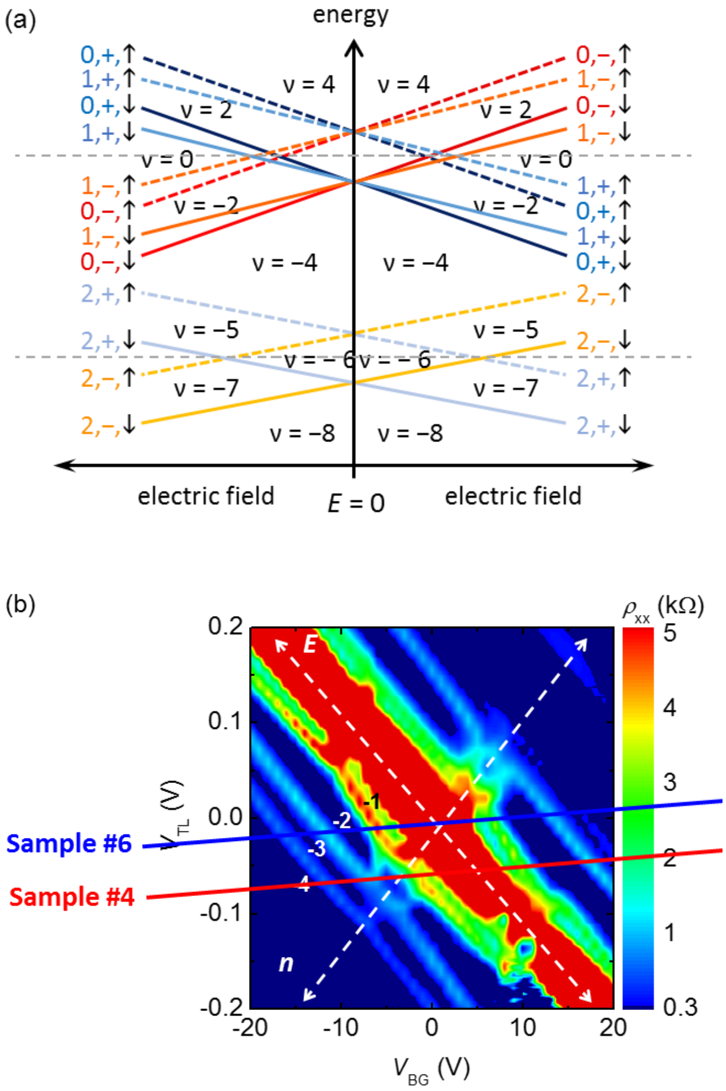

Figure 2.24: (a) Schematic representation of single electron LLs, which change as a function of *E*-field, and the ensuing QHSs. The solid (dashed) line marks the spin down (up) levels. The orbital index (N = 0, 1, 2) and layer (+, –) degrees of freedom are color coded. Assuming the direction of the applied *E*-field energetically favors the occupation of the bottom-layer, the symbols +, – mark the bottom- and top-layers, respectively. (b) The resistivity contour map of bottom bilayer graphene in sample #2 at B = 14T, accompanied with the estimated loci of the top bilayer neutrality lines for the bottom bilayer *E*-field at DNP of 0.03 (for sample #4) and 0 V/nm (for sample #6).

In Fig. 2.23, Δ_0 in samples #4 and #6 are both in the CAF incoherent phase (I_0 phase in Fig. 2.16) because the *E*-field at DNP is smaller than the $N = 0$ LL critical *E*-field, revealing similar gap values for both samples. As discussed in Chapter 2.5, we observe two different $\Delta_{\pm2}$ phases, which are layer-coherent states at zero *E*-field ($L_{\pm2}$ phase) and incoherent $\nu = \pm2$ states with a zero in-plane and a net out-of-plane spin polarization ($I_{\pm2}$ phase) at a finite *E*-field (see which phase is passed by the top bilayer charge neutrality in Fig. 2.24). For both samples #4 and #6, Δ_2 is measured in the incoherent phase, whereas Δ_{-2} is measured in different phases; Δ_{-2} in sample #4 is at the layer-layer coherent phase at zero *E*-field, whereas Δ_{-2} in sample #6 is at the incoherent phase at a finite *E*-field. Δ_2 in samples #4 and #6 are close each other, whereas Δ_{-2} in sample #6 is slightly larger than Δ_{-2} in sample #4. Δ_1 in sample #6 is not seen presumably because $\nu = 1$ QHS does not emerge at zero *E*-field as seen in the single-particle LL diagram (Fig. 2.24(a,b)), while Δ_1 in sample #4 shows a finite QHS gap. Δ_{-1} is measured in the same type of phase in both samples, at the small *E*-field lower than the phase changing $N = 0$ critical *E*-field, albeit the *E*-field direction is opposite, and the probed values in both samples are near identical. The $\nu = \pm3$ QHSs emerge at a non-zero *E*-field as seen in the LL diagram, and our measured $\Delta_{\pm3}$ values are at small finite *E*-fields in both samples. Δ_3 of samples #4 and #6 are comparable, and Δ_{-3} of both samples are also comparable.

Figure 2.25 shows the Δ_ν as a function of *B*, measured in sample #6. Compared to the layer-polarized $\nu = 0$ phase at high *E*-field, where Δ_0 is less-dependent on *B*-field,

Δ_0 measured in the spin-polarized phase here increases linearly as *B*-field increases, similar to the previous reports [22,55]. In Fig. 2.23 and Fig. 2.25, we also note Δ_0 is comparable to $\Delta_{\pm 2}$, and $\Delta_{\pm 2}$ is larger than $\Delta_{\pm 1, \pm 3}$, in agreement with a detailed Hartree-Fock analysis [1].

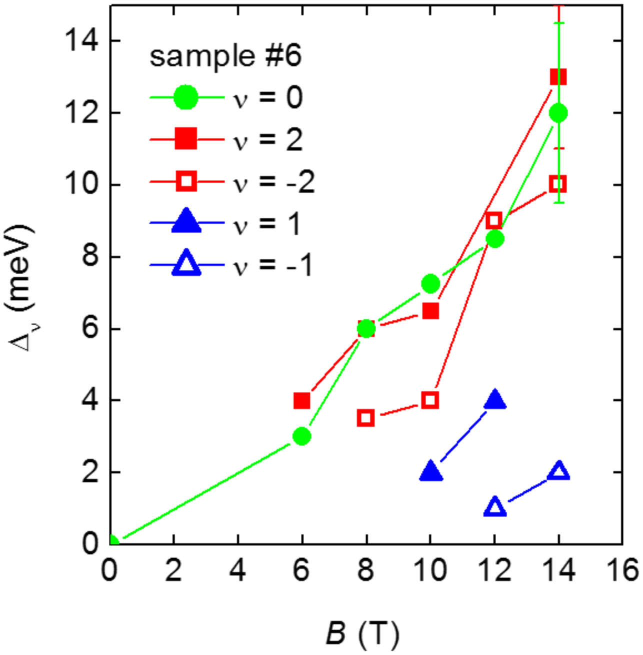

Figure 2.25: QHS gaps at ν = 0, ±1, ±2, measured as a function of magnetic field in sample #6.

2.7 Summary

In summary, we present a comprehensive study of the chemical potential and QH ferromagnetism in bilayer graphene using double bilayer graphene heterostructures. By using the top bilayer as a resistively detected Kelvin probe we map the chemical potential in zero and high magnetic fields, which sheds light on the role of interaction at $B = 0$ T, and the interplay between spin and valley degrees of freedom in the QH regime. The chemical potential vs. density dependence is strongly non-linear, allows a seamless extraction of the transverse electric field-induced band gap, as well as the quantum Hall state gaps. The quantum Hall data reveal spin-to-valley polarized transitions in all orbital Landau levels, as well as new phases at filling factors $\nu = 0$ and $\nu = \pm 2$, theoretically expected to possess spin-layer or layer-layer coherent superpositions between LLs.

Chapter 3

Giant Frictional Drag in Double Bilayer Graphene Heterostructures[†]

We study the frictional drag between carriers in two bilayer graphene flakes separated by a $2 - 5$ nm thick hexagonal boron nitride dielectric. At temperatures (T) lower than ~ 10 K, we observe a large anomalous negative drag emerging predominantly near the drag layer charge neutrality. The drag resistivity increases dramatically with reducing T, and becomes comparable to the layer resistivity at the lowest measured T = 1.5 K. At low T the drag resistivity exhibits a breakdown of layer reciprocity. A comparison of the drag resistivity to the drag layer Peltier coefficient suggests a thermoelectric origin of this anomalous, giant drag.

3.1 Introduction

Interactions between isolated electron systems in close proximity can produce a wealth of novel phenomena. A particularly interesting example is frictional drag where

---

[†] Portions of this chapter were published previously: Kayoung Lee, Jiamin Xue, David C. Dillen, Kenji Watanabe, Takashi Taniguchi, and Emanuel Tutuc, "Giant frictional drag in double bilayer graphene heterostructures," arXiv:1603.00757 (2016) [33].

Kayoung Lee performed the sample fabrication, and the low temperature measurements. Jiamin Xue assisted in sample fabrication, and Emanuel Tutuc assisted in low temperature measurements. David C. Dillen built the magnet and cryostat systems, and Takashi Taniguchi and Kenji Watanabe synthesized the hBN crystals. Kayoung Lee and Emanuel Tutuc analyzed the data and wrote the paper with input from all authors.

charge current (I_{Drive}) flowing in one (drive) layer induces a voltage drop in the opposite (drag) layer, $V_{\mathrm{Drag}} = I_{\mathrm{Drive}}\ R_{\mathrm{D}}$, R_{D} is called drag resistance. At the heart of the transresistance are inter-layer couplings without particle exchange which can be mediated by e.g., momentum exchange [57,58], energy transfer [59], or phonons [60]. While R_{D}, a sensitive probe of inter-layer interactions, is controlled by the drag mechanism, layer density, layer mobility, interlayer spacing, and temperature, the R_{D} values are generally much smaller than the layer resistance.

An exception occurs when the carriers in the two layers with opposite polarities form strongly bound electron-hole pairs, which are called as indirect excitons, as schematically described in Fig. 3.1 [61]. If such quantum correlation is made, R_{D} can reach values comparable to the layer resistance. Strongly correlated states in double layers with negligible interlayer tunneling have been experimentally verified in high mobility GaAs two-dimensional electron [14], or hole [15] double layer systems in magnetic fields such that each layer has one half-filled Landau level (LL) [13], illustrated schematically in Fig. 3.2 [13]. In a strong magnetic field, the kinetic energy of electrons is quantized into specifically allowed energy levels, which are LLs. Each LL can be occupied by a number of degenerate electrons circulating in cyclotron orbits, which fill up the 2-dimensional layer. The checkerboard represents a LL with the degenerate orbital sites. In this illustration each layer is half filled, which is the most favorable condition for the strong correlation in a double layer electron system in equilibrium.

Figure 3.3 shows Hall resistance R_{xy}^{*}, and Hall drag resistance $R_{xy,\mathrm{D}}$ as a function of the inverse of total filling factor, ν_{T}^{-1}, measured in GaAs-AlGaAs heterostructures by

M. Kellogg *et. al.* [14], where the layer densities in drive and drag layer are equal. Interestingly, $R_{xy}{}^{*}$ at $\nu_T = 1$ ($\nu = 1/2$ in each layer) shows the quantum of resistance h/e^2, a value conventionally measured at $\nu = 1$ in a two-dimensional electron system. Besides, $R_{xy,D}$ at $\nu_T = 1$ clearly reaches the same value as $R_{xy}{}^{*}$, the quantized value at h/e^2, when d/ℓ is small, where $d = 27.9$ nm is the interlayer separation and $\ell = (\hbar/eB)^{1/2}$ is the magnetic length, which is proportional to the average electron spacing within each layer. This is a clear signature of a strong interlayer correlation. As d/ℓ increases, $R_{xy,D}$ collapses and $R_{xy}{}^{*}$ shows the classical Hall resistance behavior.

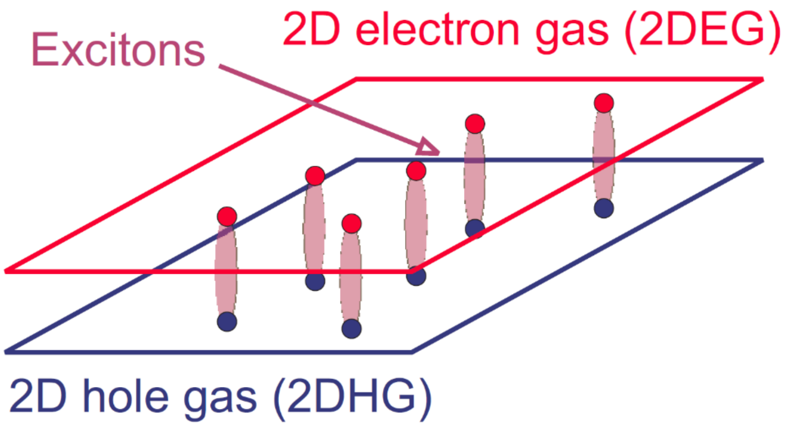

Figure 3.1: Schematic of electron-hole pairs, which are indirect excitons, formed in a two-dimensional electron (2DEG)-hole (2DHG) system. The figure is adapted from Ref. [61].

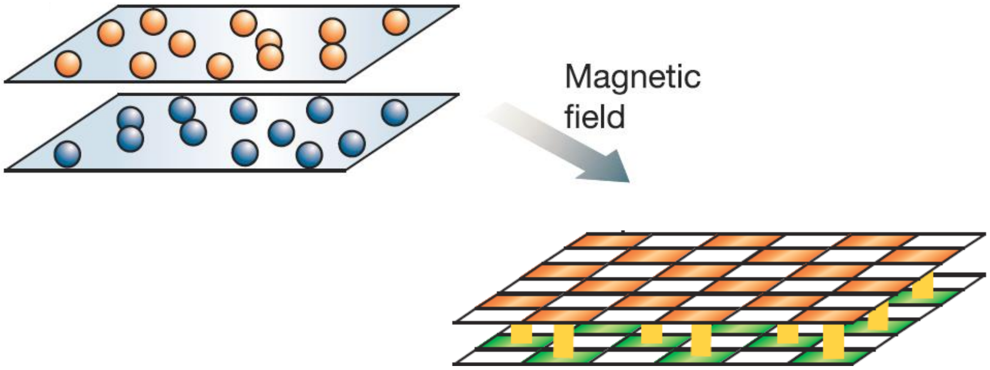

Figure 3.2: In a strong magnetic field, electron energies are quantized into highly degenerate, specifically allowed energy levels, LLs. The checkerboard represents a LL with the degenerate, cyclotron orbit sites. In this illustration each layer is half filled, a favorable condition for the exciton condensation. The figure is adapted from Ref. [13].

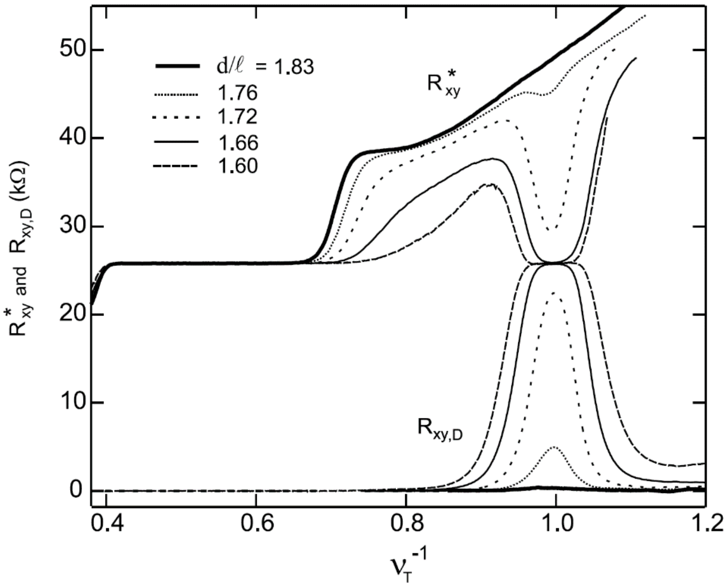

Figure 3.3: Hall resistance R_{xy}^* and Hall drag resistance $R_{xy,D}$ of a low density GaAs-AlGaAs double layer, measured at T = 30 mK. Layer densities are $n_B = n_T$ = 2.6, 2.8, 3.0, 3.2, and 3.4 × 10^{10} cm^{-2}, giving d/ℓ = 1.6, 1.66, 1.72, 1.76, and 1.83, respectively, at $\nu_T = 1$. The figure is adapted from [14].

Extensive experimental effort has been devoted to the drag measurements in electron-hole double layers, using GaAs electron-hole double layers [62,63], graphene double layers [64,65], and most recently graphene-GaAs double layers [66], motivated in part by the search for equilibrium indirect exciton condensates. A common thread in these experiments is the observation of an anomalous R_D that increases with reducing T, accompanied with a breakdown of layer reciprocity when interchanging the drive and drag layers [62,63,66]. For instance, Fig. 3.4 presents Coulomb drag measured in a GaAs-AlGaAs electron-hole double layer by Croxall *et. al.* [62], where the interlayer barrier spacing is 25 nm. In Fig. 3.4, drag resistivity were measured in the hole layer ($\rho_{D,h}$), and in the electron layer ($\rho_{D,e}$), individually, by inter-changing the drive and drag layers. When both layer densities are $n = p = 7 \times 10^{10}$ cm^{-2}, $\rho_{D,h}$ shows an upturn at ~ 1 K, followed by a downturn at ~ 0.5 K, whereas $\rho_{D,e}$ keeps decreasing as T decreases, which reveals Onsager's reciprocity breakdown. For the densities at $n = p = 1 \times 10^{11}$ cm^{-2}, $\rho_{D,h}$ changes its polarity at ~ 0.5 K, and the negative drag increases as T decreases, whereas $\rho_{D,e}$ shows upturn at ~ 0.5 K, where the layer-reciprocity is still not valid. The increasing drag, along with a breakdown of layer reciprocity observed at low T is not clearly explained. At T higher than 1 K, $\rho_{D,h} \approx \rho_{D,h} \propto T^2$ is satisfied, which is well understood based on the momentum transfer rate between a couple of parallel 2-dimensional electron systems [58].

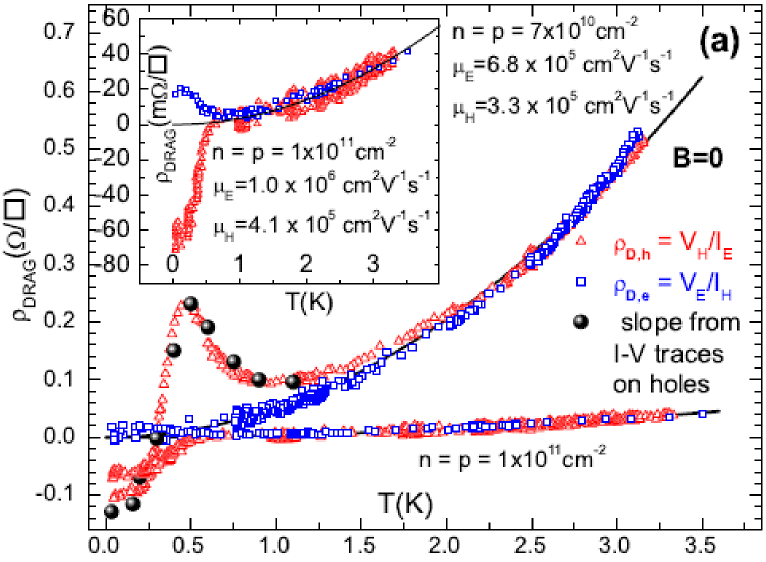

Figure 3.4: Drag resistivity measured in the hole layer ($\rho_{D,h}$, red triangle) and the electron layer ($\rho_{D,e}$, blue rectangular), when both layer densities are $n = p = 7 \times 10^{10}$ cm^{-2} and at $n = p = 1.0 \times 10^{11}$ cm^{-2}, in a GaAs-AlGaAs electron-hole double layer. The inset shows an expanded view of the lower traces at $n = p = 1.0 \times 10^{11}$ cm^{-2}. The upturn was no longer observed at this density on the holes, but the downturn is seen. The solid black lines are best-fits to a T^2 behavior. The figure and caption are adapted from [62].

In this regard, double bilayer graphene separated by a thin hexagonal boron nitride (hBN) is a particularly compelling system. The near parabolic energy-momentum dispersion in bilayer graphene allows the Coulomb to kinetic energy ratio to be tuned via density, unlike monolayer graphene where this ratio is fixed [16]. Moreover, the availability of ultra-thin dielectrics allows double layers to be realized with interlayer spacing down to a few nm, granting access to the strong coupling regime $d \ll l$, where l is the inter-particle distance. This effectively nests the two isolated electronic systems in the same plane. Here, we investigate the frictional drag in double bilayer graphene heterostructures, consisting of two bilayer graphene separated by a $2 - 5$ nm thick interlayer hBN dielectric, which allows us to explore the drag in a wide range of layer densities, and for all combinations of carrier polarity. Strikingly, we find a giant and negative drag resistivity at charge neutrality, comparable to the layer resistivity at the lowest T.

The samples are fabricated using a layer-by-layer transfer process, as discussed in Chapter 2.2. The top and bottom bilayer resistivities, as well as the frictional drag in both layers are probed using small signal, low frequency lock-in techniques, as a function of back-gate (V_{BG}), and interlayer bias applied on the top bilayer (V_{TL}), discussed further in Chapter 3.2.1. We investigated four samples, #1, #2, #4, #5, with different interlayer spacing and layer mobilities, and their specifications are given in Table 2.1. The interlayer resistance values are in the range 1.6 – 20 GΩ. The drag resistance measurement errors associated with finite interlayer resistance are of the order 1%. The key features of the drag data presented here are similar in all samples.

3.2 Methods

3.2.1 Layer and Drag Measurements in Double Bilayer Graphene

The layer densities are tuned using a combination of back-gate (V_{BG}), and interlayer bias applied on the top bilayer (V_{TL}) [67]. Four-point resistance measurements were performed on the bottom and top bilayer graphene by flowing source currents of 1 nA in each bilayer using lock-in amplifiers, as described in Fig. 3.5(a) [67]. Different lock-in frequencies, ranging between 7 – 17 Hz were chosen for the bottom and top bilayers to exclude the cross-talk between the two bilayers. A radio-frequency transformer (Jensen Transformers, model JT-SUB-BB) is used to flow AC currents in the top bilayer, while applying a DC bias V_{TL} with respect to ground. The samples were measured in a variable-temperature liquid ^{4}He flow cryostat, which provides temperature (T) down to 1.5 K.

Coulomb drag measurements were performed either on the bottom or top bilayer graphene, individually. While flowing an AC drive current I_{Drive} of 1 – 10 nA in the drive layer, we measure the four-point drag voltage V_{Drag} in the opposite, drag layer [67]. The drag resistance R_{Drag} is then defined as $V_{\mathrm{Drag}}/I_{\mathrm{Drive}}$. Conventional lock-ins are used to flow AC drive currents, and to measure the AC drag voltages, where the lock-in frequencies for the bottom and top bilayers are synchronized. Figure 3.5(b) describes the drag measurements on the top bilayer, while flowing an AC drive current in the bottom bilayer.

The drag resistances were also probed by flowing DC drive currents; we flow DC drive current by applying a DC voltage along the drive layer, and measure the voltage drop (drag voltage) along the opposite, drag layer, as described in Fig. 3.5(c). R_{Drag} is then defined as $dV_{\text{Drag}}/dI_{\text{Drive}}$ in the limit of $I_{\text{Drive}} = 0$. Another schematic, which shows how the contacts are selected for the drag measurement, accompanied with the sample micrograph is presented in Fig. 3.6. Figure 3.7 shows an example of the measured V_{Drag} as a function of I_{Drive}. V_{Drag} shows a linear response to I_{Drive} in the current range of interest.

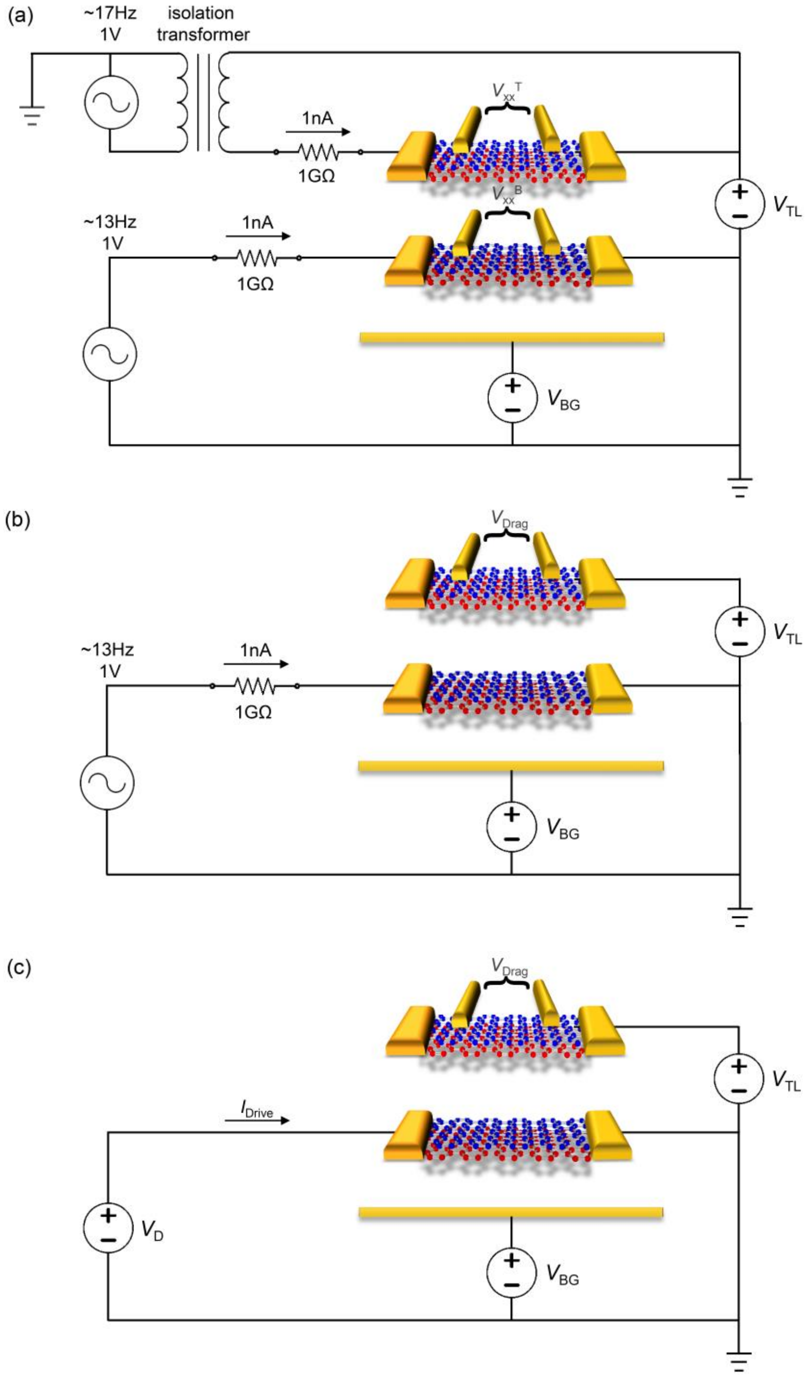

Figure 3.5: Schematics of the circuits used to probe (a) layer resistances of both bottom and top bilayer simultaneously, and (b,c) drag resistance of the top bilayer using AC drive current (panel b), and using DC drive current (panel c) as a function of back-gate (V_{BG}) and interlayer bias (V_{TL}). The distance between the two bilayers are exaggerated for clarity.

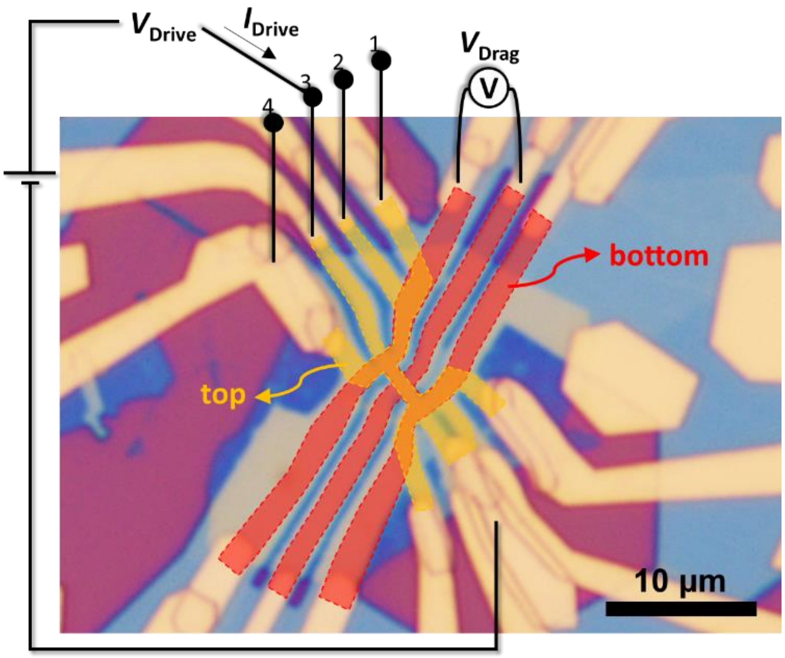

Figure 3.6: Optical micrograph of a representative double bilayer graphene sample (sample #4), and schematics describing the drag measurement in the bottom bilayer. The red (yellow) contour represents the bottom (top) bilayer. The drive current (I_{Drive}) is applied to one of top bilayer contacts 1, 2, 3, 4, marked on the schematic, and one of opposite side of top bilayer contacts is grounded. The drag voltage (V_{Drag}) is measured in the bottom bilayer.

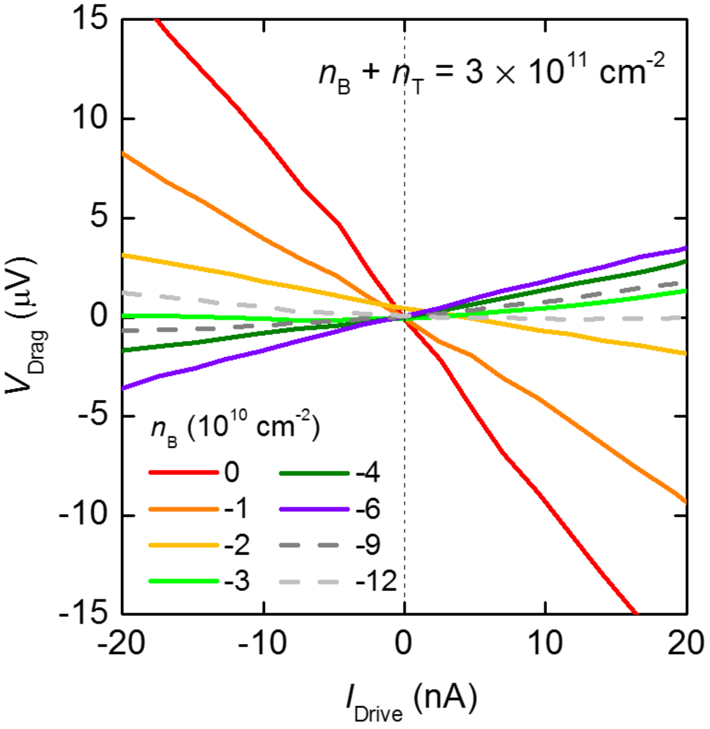

Figure 3.7: Example of the drag voltage (V_{Drag}) measured in the bottom bilayer as a function of drive current (I_{Drive}) in the top bilayer. The different traces are acquired at a fixed total density $n_B + n_T = 3 \times 10^{11}$ cm^{-2}, but at different each layer density. The bottom bilayer density (n_B) is indicated. Data are acquired in sample #4, at $T = 1.5$ K.

3.2.2 Carrier Density Calculation

The detailed gate-depending characteristics of each bilayer graphene, without the crosstalk between the two bilayers, in double bilayer graphene heterostructures are discussed in Chapter 2. The bottom (n_B) and top (n_T) bilayer densities and gate biases have the following relations:

$$eV_{BG} = e^2(n_B + n_T)/C_{BG} + \mu_B \qquad (3.1)$$

$$eV_{TL} = -e^2 n_T/C_{int} - \mu_T + \mu_B \qquad (3.2)$$

Here, C_{BG} and C_{int} are the back-gate and interlayer dielectric capacitances, whereas μ_B and μ_T are the chemical potentials (Fermi energies, μ) of the bottom and top bilayers, respectively; e is the electron charge. μ and n are positive (negative) for electrons (holes), and V_{BG} and V_{TL} in Eqs. 3.1 and 3.2 are referenced with respect to the bias values at $n_B = n_T = 0$ (double neutrality point, DNP). The C_{BG} and C_{int} values are determined using magnetotransport measurements of individual bilayers [34].

Our previous studies in double bilayer graphene heterostructures probe experimentally the chemical potential in bilayer graphene [18]. Figure 3.8 shows the μ vs. n measured in multiple double bilayer graphene samples. Fitting to the measured μ in sample #4 using a polynomial function provides the following formula describing μ as a function of carrier density n.

$$\mu(n) = 0.357n + 0.208n^2 - 0.884n^3 - 2.23n^4 + 2.98n^5 \qquad (3.3)$$

valid in the range of $-0.3 < n < 0.3$, where n is expressed in unit of 10^{13} cm^{-2}, and μ is in unit of eV. While only a fit to the experimental data, this μ vs. n dependence for bilayer graphene in Eq. (3.3) is useful in solving Eqs. (3.1) and (3.2) self-consistently. Figure 3.9(a,b) presents the calculated n_B and n_T as a function of V_{BG} and V_{TL} for sample #4.

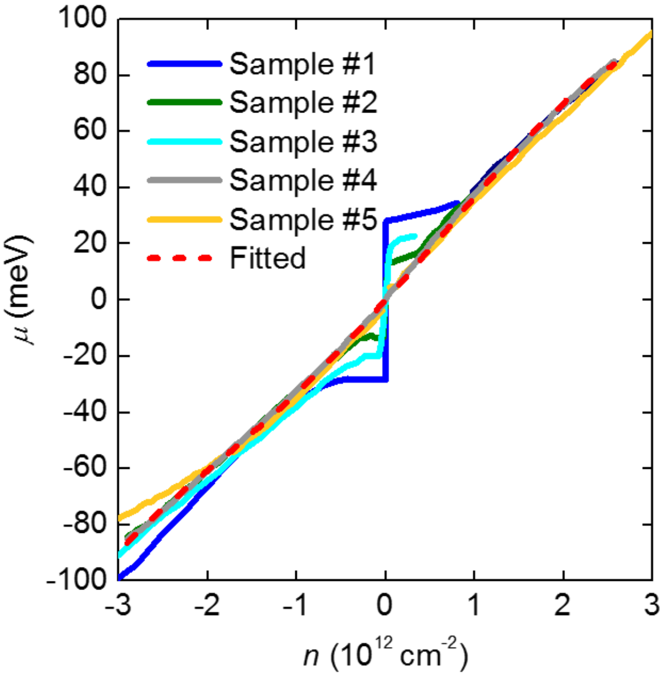

Figure 3.8: μ vs. n in bilayer graphene, measured using our double bilayer graphene heterostructures as presented in Ref. [18].

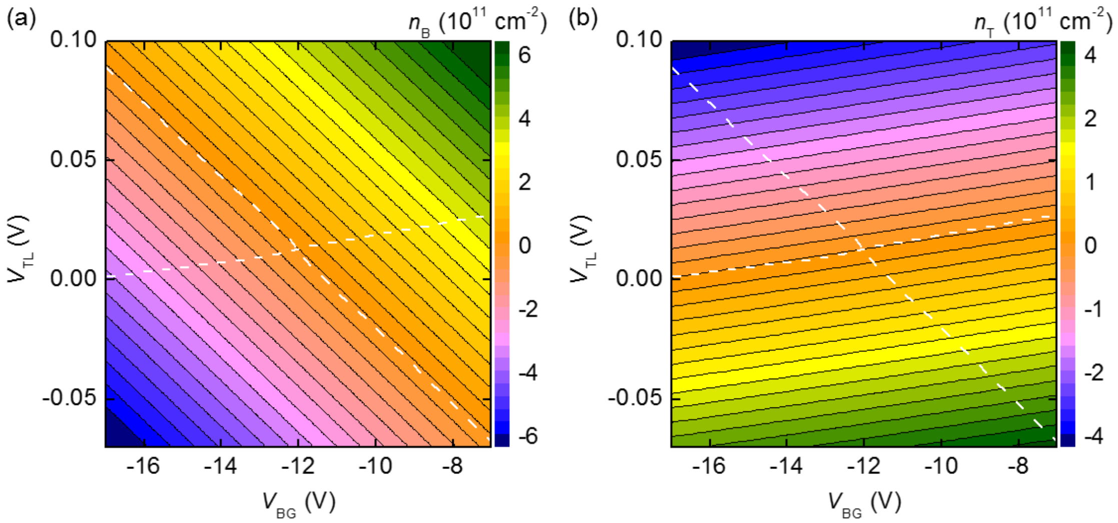

Figure 3.9: (a) n_B and (b) n_T calculated as a function of V_{BG} and V_{TL} for sample #4. The white dashed lines represent the measured charge neutrality of the bottom and top bilayer graphene.

3.2.3 Electric Field Calculation

The transverse electric fields (E) across the bottom (E_B) and top (E_T) bilayer graphene can be described as [34]

$$E_B = en_B/2\varepsilon_0 + en_T/\varepsilon_0 + E_{B0} \qquad (3.4)$$

$$E_T = en_T/2\varepsilon_0 + E_{T0} \qquad (3.5)$$

using Eq. (3.1), where ε_0 is the vacuum permittivity, and E_{B0} (E_{T0}) is the E value in the bottom (top) bilayer graphene at DNP by an unintentional doping. In the bottom bilayer graphene, $n_B = 0$ and $E_B = 0$ point is identified by the Dirac point with the lowest resistance. Eq. (3.4) at $n_B = 0$ and $E_B = 0$ can be written as

$$E_{B0} = -en_T/\varepsilon_0 = C_{BG}\Delta V_{BG}/\varepsilon_0 \qquad (3.6)$$

, where ΔV_{BG} is the difference between the V_{BG} values at DNP and at the $n_B = 0$ and $E_B = 0$ point. However, E_{T0} cannot be calculated in the similar manner.

We estimate E_{T0} using two different methods. For the low mobility top bilayer graphene, not encapsulated by hBN, E_{T0} is approximated as discussed in Ref. [34]. Here, we presume the dopants, which move DNP from $V_{BG} = 0$ and $V_{TL} = 0$, are mostly located on top of the top bilayer graphene. Gauss law then provides

$$E_{T0} = C_{BG}V_{BG\_DNP}/\varepsilon_0 \qquad (3.7)$$

where V_{BG_DNP} is the V_{BG} value at DNP. For the higher quality double bilayer graphene heterostructures, where both bottom and top bilayer graphene are encapsulated by hBN, and have high top and bottom bilayer mobilities, we estimate the E-field by measuring transport gaps as discussed in Ref. [68], addressed in detail in the following chapter.

3.2.3.1 Transport Gap Measurement in Bilayer Graphene

Bernal stacked bilayer graphene exhibits a transverse *E*-field induced band gap (Δ) [5]. At a finite *E*-field, bilayer graphene conductivity shows finite threshold voltages along the electron and hole branches, analogous to the threshold voltages seen in a conventional bulk semiconductor with a band gap, and the transport gap can be extracted from the threshold voltages. Ref. [68] shows the gap extraction in dual-gated bilayer graphene with oxide dielectrics at different *E*-fields. This method is employed here to estimate the transport gap, and corresponding *E*-field value at DNP in the bottom and top bilayer graphene in our double bilayer graphene heterostructures with hBN dielectrics.

Figure 3.10(a) shows conductivity (σ) of the bottom bilayer graphene, at different E_B, measured at $T = 1.5$ K, in sample #1; E_B is calculated using Eq. (3.4). At zero *E*-field, σ is non-zero at $n_B = 0$ because of thermally excited carriers and disorder in graphene. By contrast, at a finite *E*-field σ becomes vanishing at $n_B = 0$ and up to a finite $|n_B|$, which increases with the *E*-field. We note n_B here denotes the mobile carrier density calculated for the zero gap bottom bilayer graphene. When there is a finite E-field and corresponding band gap, the actual mobile carrier density will be smaller than the presented n_B value because a finite gate bias, which is the threshold bias, is consumed to move the Fermi energy to either conduction or valence band edge. Therefore, the threshold n_B value at the threshold bias presented here is related to band gap value, rather than the actual charge carrier density in graphene.

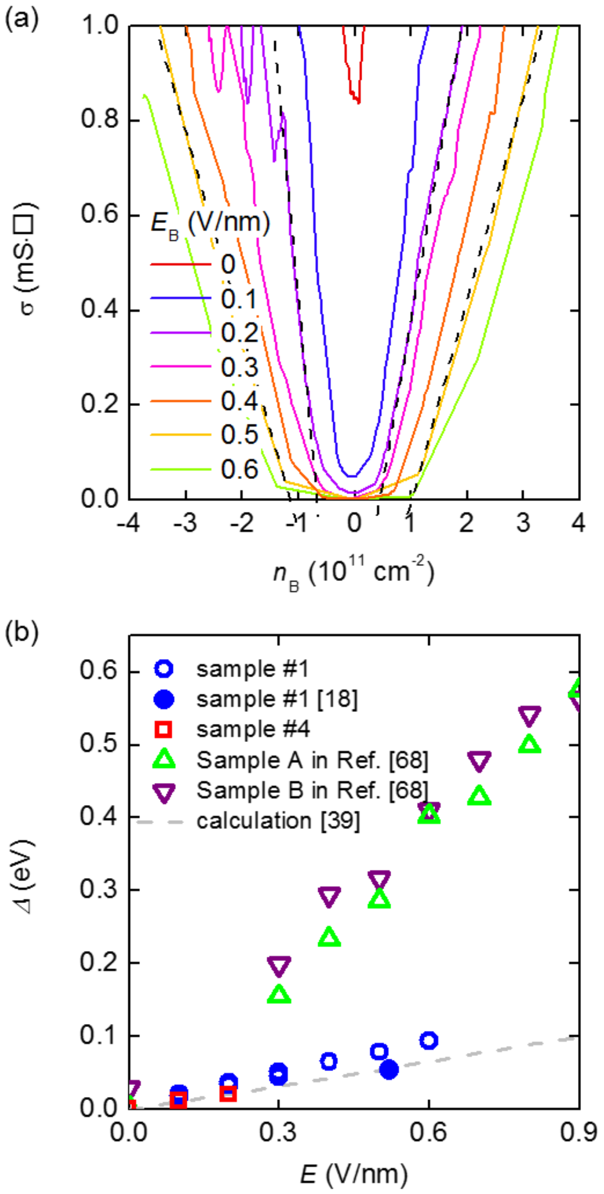

Figure 3.10: (a) Conductivity of the bottom bilayer graphene as a function of n_B at different E_B, measured in the bottom bilayer of sample #1, at T = 1.5 K. (b) The extracted band gap values as a function of E-field. Transport gaps were measured in the bottom bilayer of sample #1 (blue open circle) and sample #4 (red open rectangular). Gap values measured using our chemical potential probing technique in Chapter 2 (blue closed circle) [18], as well as the transport gaps measured in dual-gated bilayer graphene samples with oxide dielectrics, Sample A and Sample B in Ref. [68], (green and purple triangles) are also included for comparison. Dashed line represents the theoretically calculated values [39].

By considering the top bilayer graphene as a top gate, the transport gap extraction procedure, used for the dual-gated bilayer graphene [68] can be directly applied here to measure the gap of the bottom bilayer in our double bilayer graphene heterostructures. The transport gap values (Δ) are extracted from the measured two threshold voltages, V_{BG}' or V_{TL}', which is the difference between the V_{BG} or V_{TL} values at $n_B = 0$ point and at the threshold point:

$$\Delta = \frac{2e}{C_{BG} + C_{int}} (C_{BG} V_{BG}' + C_{int} V_{TL}') \qquad (3.8)$$

Figure 3.10(b) shows the transport gap extracted from the conductivity thresholds in samples #1 (blue open circle) and #4 (red open rectangular), without taking into account disorder induced interface and gap states. For sample #1, the bottom bilayer band gap at DNP was also probed using our chemical potential probing technique presented in Chapter 2 and Ref. [18], also included in Fig. 3.10(b) (blue filled circle). Transport gaps measured in two dual-gated bilayer graphene samples with oxide dielectrics [68] (Sample A and Sample B, green and purple triangles, respectively), as well as theoretically expected gap values [39] (dashed line), are also included for comparison. The gaps extracted from the samples with oxide dielectrics are significantly larger than the theoretically calculated values, and this is because of a large density of localized states inside the gap (D_{it}) [69–73]. In contrast, the transport gap values measured in samples with hBN dielectrics are very close to the theoretically expected values. The transport gaps measured in sample #4 are in perfect agreement with the calculation, indicating negligible disorder and gap states. Sample #1 shows transport gap values slightly larger than the calculation.

Taking into account the density of gap states, the transport gap is written as:

$$\mathit{\Delta} = \frac{2e}{C_{\mathrm{BG}} + C_{\mathrm{int}} + e^2 D_{\mathrm{it}}} \left(C_{\mathrm{BG}} V_{\mathrm{BG}}' + C_{\mathrm{int}} V_{\mathrm{TL}}'\right) \qquad (3.9)$$

By assuming $\mathit{\Delta}$ is the same as the theoretically expected gap value using D_{it} as the fitting parameter, we extract D_{it} values as a function of *E*-field. Figure 3.11(a) shows the calculated D_{it} (red) and total gap states (yellow), which is given by $D_{\mathrm{it}} \times \mathit{\Delta}$, as a function of *E*-field for the two dual-gated bilayer graphene samples with oxide dielectrics; closed and open symbols mark different two samples. The obtained D_{it} values vary between ~ 6×10^9 and ~ 9×10^9 cm^{-2}/meV, and the *E*-field dependence (band gap dependence) is not observed. This indicates the energy-independent D_{it}, which leads linearly increasing total gap-states with increasing the *E*-field (band gap), as seen in Fig. 3.11(a). In contrast, Fig. 3.11(b) shows the D_{it} and total gap states as a function of *E*-field for sample #1, double bilayer graphene sample encapsulated with hBN dielectrics. Interestingly, the extracted D_{it} in sample #1 keeps decreasing, and appears to be saturated as the *E*-field increases, distinct from the behavior seen in samples with oxide dielectrics. This suggests that D_{it} is mostly concentrated at the edge of the band. Besides, we note that the total gap states linearly increase as the *E*-field increases with the offset of ~ 1.6×10^{10} cm^{-2} at $E = 0$, which is translated into the localized states concentrated at the conduction and valence band edges. The linearly increasing total gap states with increasing *E-field* shows that the D_{it} is near energy-independent as 10^8 cm^{-2}/meV except for at the band edges.

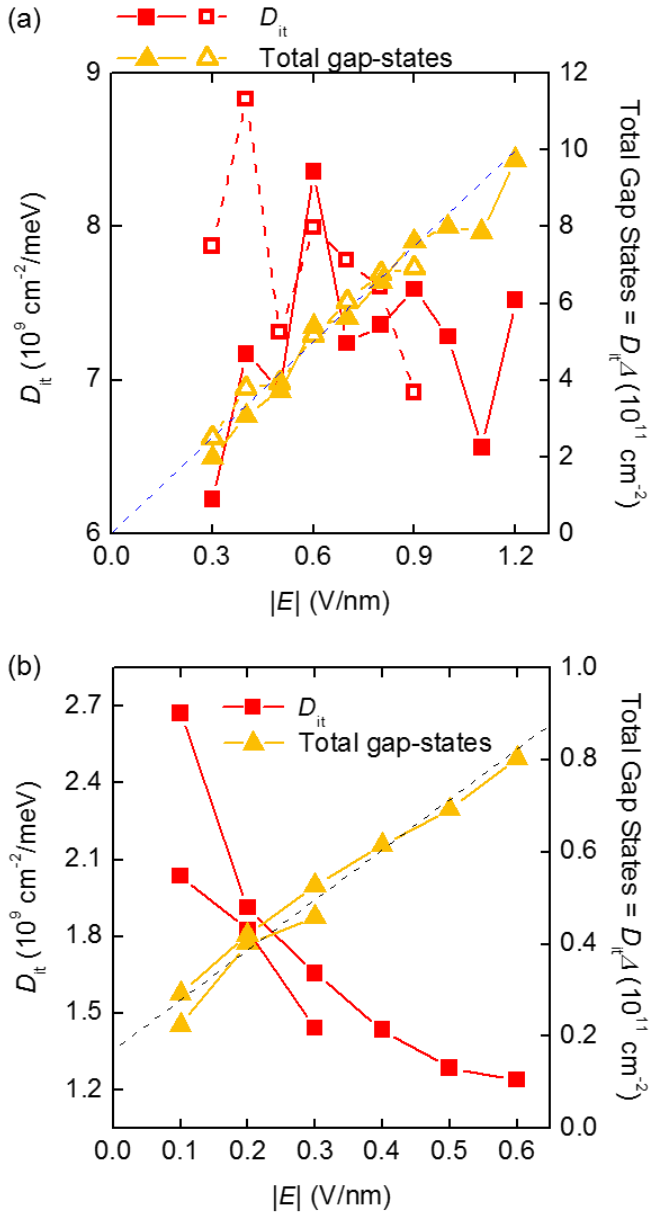

Figure 3.11: (a) D_{it} (left axis) and total gap states (right axis) as a function of |*E*|, in the two different dual-gated bilayer graphene samples with oxide dielectrics. Closed and open symbols mark different samples. (b) D_{it} (left axis) and total gap states (right axis) in sample #1, which is a double bilayer graphene sample with hBN dielectrics.

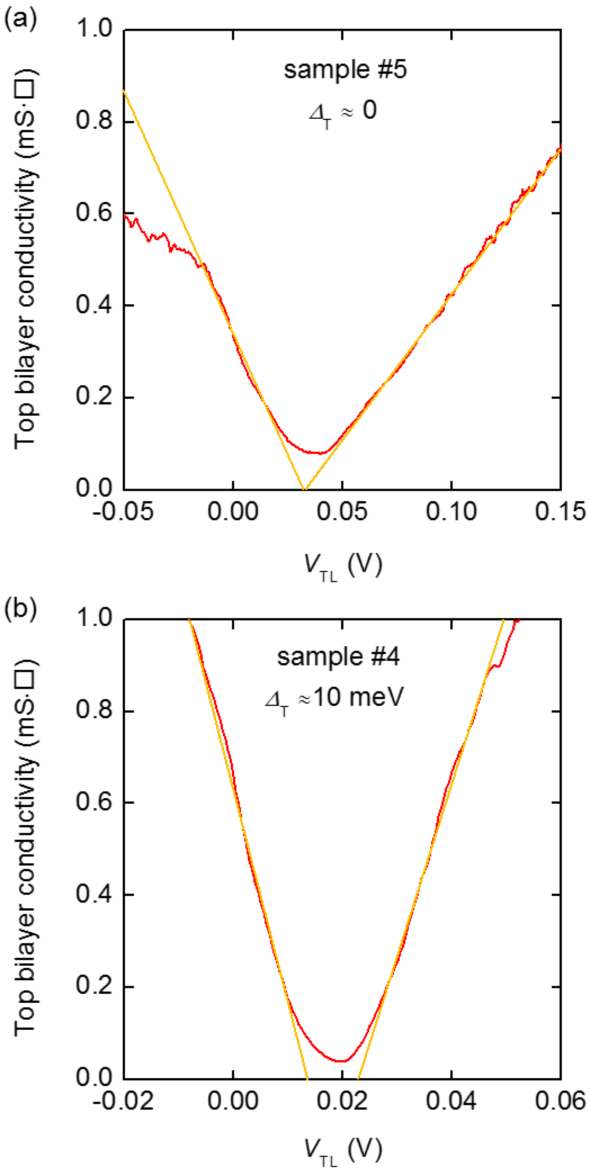

Figure 3.12: Top bilayer conductivity as a function of V_{TL} in the proximity of DNP (a) in sample #5 which shows almost zero transport gap, and (b) in sample #4, which shows the transport gap of 10 meV.

For the top bilayer graphene, we measure the transport gap from the conductivity thresholds, and then inversly estimate E_{T0}, assuming D_{it} is insignificant. From Eq. (3.2), we obtain the transport gap Δ_T in the top bilayer in the proximity of DNP, simply as

$$\Delta_T = 2eV_{TL}' \qquad (3.10)$$

neglecting the minor variations of μ_B and E_T in the proximity of DNP.

Figure 3.12(a,b) shows the top bilayer conductivity of sample #5 and sample #4, in the proximity of DNP. The threshold voltage measurements suggest $\Delta_T = 0$ in sample #5, and $\Delta_T = 10$ meV in sample #4. Using the transport gap vs E-field dependence, measured in the bottom bilayer (Fig. 3.10(b)), we estimate $E_{T0} \approx 0$ in sample #5, and $E_{T0} \approx 0.1$ V/nm in sample #4. The obtained E_{B0} and E_{T0} are given in Table 2.1. Using Eq. (3.4) and Eq. (3.5), along with the E_{B0} and E_{T0} values, E_B and E_T can be calculated as a function of n_B and n_T, which are converted from the applied V_{BG} and V_{TL} as presented in Fig. 3.9. Figure 3.13(a,b) shows the calculated E_B and E_T as a function of V_{BG} and V_{TL} in sample #4.

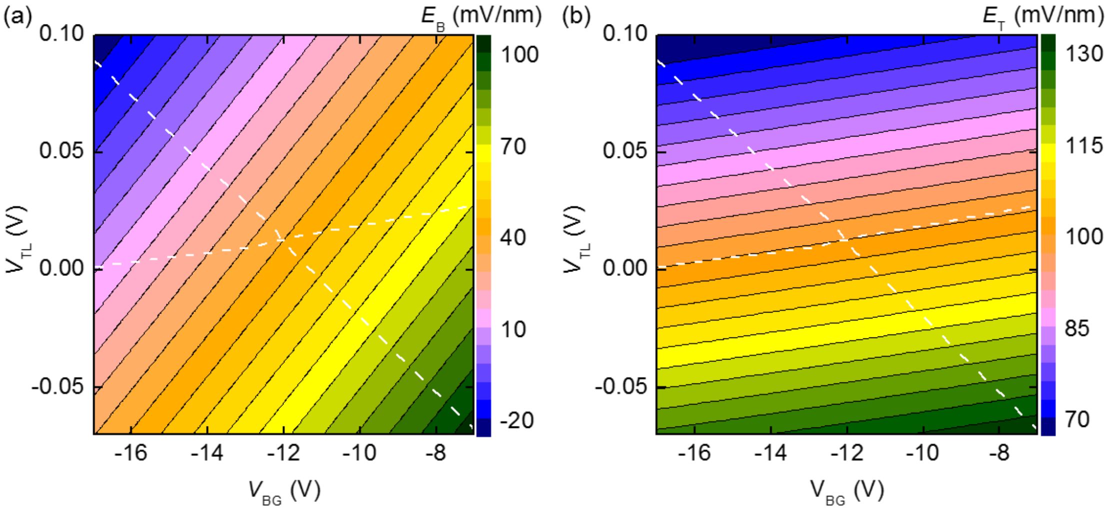

Figure 3.13: (a) E_B and (b) E_T in sample #4 calculated as a function of V_{BG} and V_{TL}. The white dashed lines show the measured charge neutrality of the bottom and top bilayer graphene.

3.3 Frictional Drag in Double Bilayer Graphene

3.3.1 Giant Drag in the Proximity of Drag Layer Charge Neutrality

Figures 3.14(b) and 3.14(c) show the top (ρ_T) and bottom (ρ_B) bilayer resistivities measured in sample #4 (Fig. 3.14(a)) at T = 1.5 K. The bottom bilayer responds to V_{BG} and V_{TL} similar to a dual-gated bilayer graphene, in which the density and transverse electric field (E) are controlled independently [18]. The locus of high resistance points in Figs. 3.14(b,c) marks the charge neutrality lines for both bilayers. Figure 3.14(c) also shows the carrier type in each of the four quadrants defined by the two charge neutrality lines. To examine variations in the drag resistance when interchanging the drag and drive layers, we probe both the bottom ($\rho_{D,B}$) and top ($\rho_{D,T}$) drag resistivities, with the top or bottom bilayers serving as the drive layers, respectively. Figures 3.14(d) and 3.14(e) show $\rho_{D,B}$ and $\rho_{D,T}$, respectively, measured as a function of V_{BG} and V_{TL} in sample #4, at T = 1.5 K. A comparison of Fig. 3.14(b,c) data on one hand, and Fig. 3.14(d,e) data on the other, shows a large, negative drag resistivity emerging predominantly near or at the drag layer charge neutrality.

To better visualize Fig. 3.14(d,e) data, in Fig. 3.15 we plot $\rho_{D,B}$ [panel (a)] and $\rho_{D,T}$ [panel (b)] as a function of top (n_T) and bottom (n_B) bilayer densities, converted from V_{BG} and V_{TL}. Figure 3.15 reveals a number of interesting features. First, $\rho_{D,B}$ is large in the proximity of $n_B = 0$ line in Fig. 3.15(a), while $\rho_{D,T}$ is large near $n_T = 0$ line in Fig. 3.15(b). Near the double neutrality point (DNP), $n_B = n_T = 0$, $\rho_{D,B}$ and $\rho_{D,T}$ reach values close to 1 kΩ. Second, the reciprocity with respect to interchanging the drag and drive layers breaks down, i.e. $\rho_{\mathrm{D,B}}(n_{\mathrm{B}}, n_{\mathrm{T}}) \neq \rho_{\mathrm{D,T}}(n_{\mathrm{B}}, n_{\mathrm{T}})$ in Fig. 3.15.

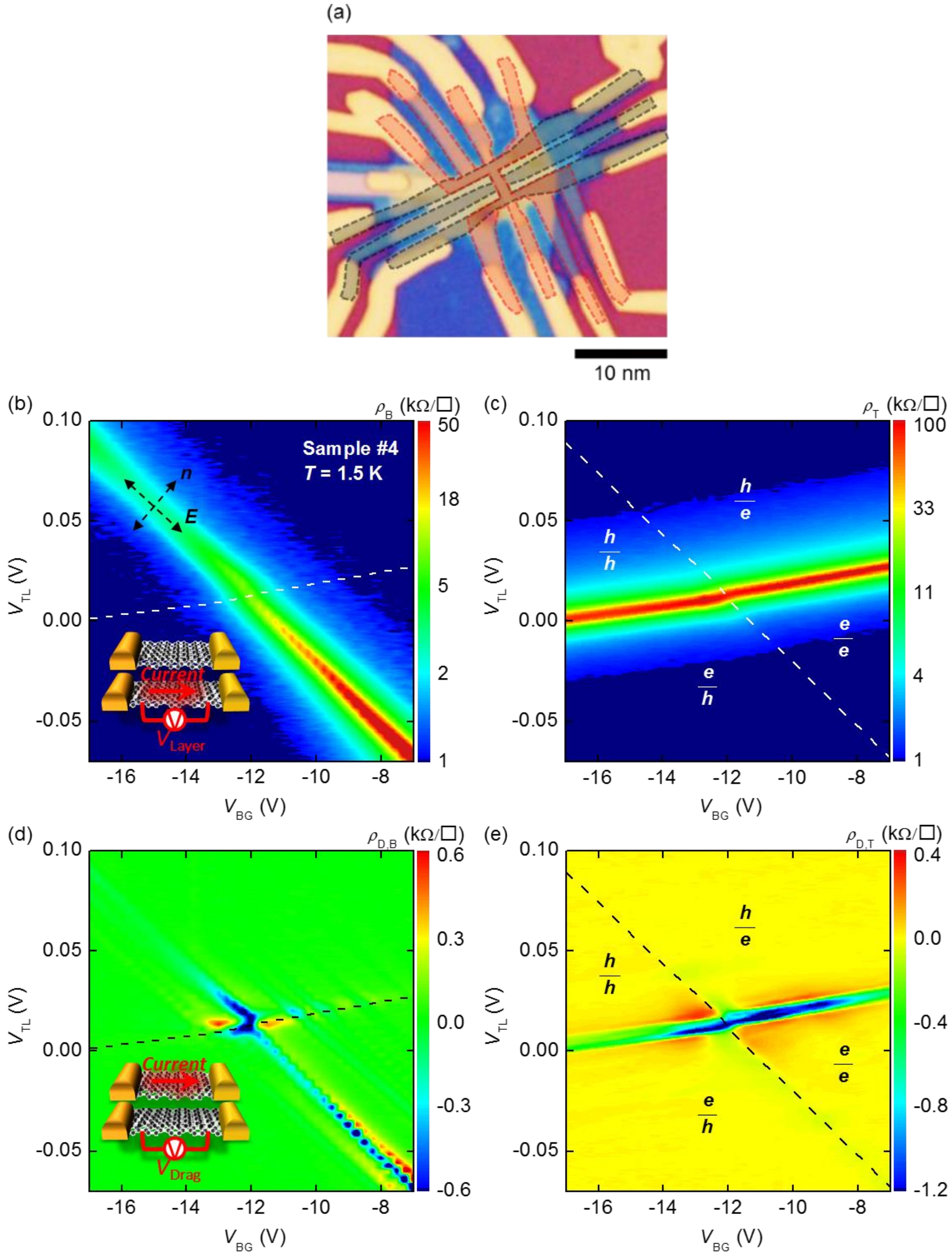

Figure 3.14: (a) Optical micrograph of a double bilayer graphene heterostructure. The red (gray) dashed contour lines mark the top (bottom) bilayer. (b) ρ_B, and (c) ρ_T measured in sample #4 as a function of V_{BG} and V_{TL} at $T = 1.5$ K. Panel (b) inset shows the sample and measurement schematic. The white dashed lines in panels (b) and (c) mark the charge neutrality lines of the top and bottom bilayers, respectively. Panel (c) shows the carrier type in the two bilayers in the four quadrants defined by the two charge neutrality lines. (d) $\rho_{D,B}$ and (e) $\rho_{D,T}$ measured as a function of V_{BG} and V_{TL} at $T = 1.5$ K.

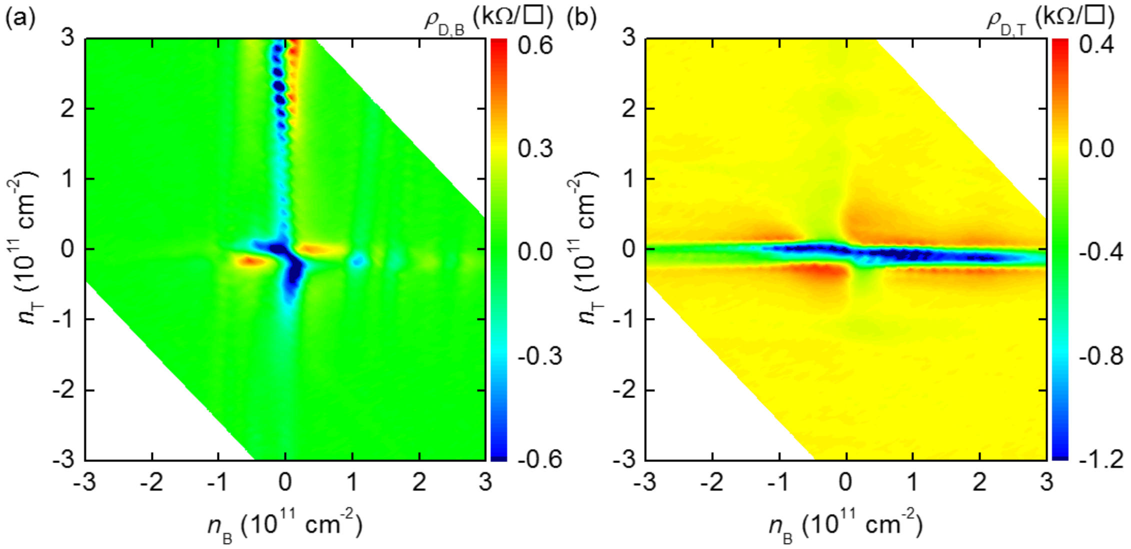

Figure 3.15: (a) $\rho_{D,B}$ and (b) $\rho_{D,T}$ as a function of n_B and n_T, measured in sample #4, and at T = 1.5 K. The data show a large drag resistivity emerging along the drag layer charge neutrality, relatively insensitive to the drive layer density.

In light of the anomalous drag observed in Figs. 3.14 and 3.15, in the following we examine the drag layer resistivity in more detail, concentrating on the drag layer density, and transverse electric field (E) dependencies. The latter is relevant for bilayer graphene as the energy-momentum dispersion changes with E, concomitant with gap opening at charge neutrality [5]. Figure 3.16(a) shows ρ_{B}, $\rho_{\mathrm{D,B}}$, and the corresponding normalized drag $\rho_{\mathrm{D,B}}/\rho_{\mathrm{B}}$ as a function of $n_{\mathrm{B}} = -n_{\mathrm{T}}$, namely at equal density in the two bilayers, with opposite polarity carriers, in sample #4. $\rho_{\mathrm{D,B}}$ shows a very strong, negative peak at DNP, which surprisingly becomes comparable to ρ_{B} at $T = 1.5$ K. As $n_{\mathrm{B}} = -n_{\mathrm{T}}$ increases $\rho_{\mathrm{D,B}}$ changes sign, becomes positive at a finite $|n_{\mathrm{B}}|$, and then vanishes as $|n_{\mathrm{B}}|$ increases further.

Figure 3.16(b) shows ρ_{B}, $\rho_{\mathrm{D,B}}$ (left panel), and $\rho_{\mathrm{D,B}} = \rho_{\mathrm{B}}$ (right panel) vs. n_{B} in the proximity of $n_{\mathrm{B}} = 0$ and $n_{\mathrm{T}} = 0$. The negative $\rho_{\mathrm{D,B}}$ at $n_{\mathrm{B}} = 0$ is notable, similar to the large, negative $\rho_{\mathrm{D,B}}$ peak at DNP in Fig. 3.16(a). However, the magnitude of $\rho_{\mathrm{D,B}}/\rho_{\mathrm{B}}$ at $n_{\mathrm{B}} = 0$ and $n_{\mathrm{T}} \neq 0$ is smaller than that at DNP. As $|n_{\mathrm{B}}|$ increases, $\rho_{\mathrm{D,B}}$ changes polarity, and becomes positive, consistent with the observed trend at DNP, albeit with a lower magnitude. An examination of the electrostatics in double layers shows that at $n_{\mathrm{B}} = 0$, the E value across the bottom bilayer changes as n_{T} changes as indicated in Fig. 3.16(b) legend. We observe that $\rho_{\mathrm{D,B}}$ at $n_{\mathrm{B}} = 0$ grows as ρ_{B} increases with increasing E-field, leading to a relatively constant $\rho_{\mathrm{D,B}} = \rho_{\mathrm{B}}$ ratio.

Figure 3.17 shows $\rho_{\mathrm{D,B}}$ as a function of $n_{\mathrm{B}} = -n_{\mathrm{T}}$ at different T in sample #4, showing a large, negative drag at DNP. We note that Fig. 3.16(a,b) and Fig. 3.17 were collected in separate cooldowns. Similar to Fig. 3.16(a) data, $\rho_{D,B}$ becomes positive as $|n_B|$ increases, and subsequently decreases towards zero with increasing density. The inset of Fig. 3.17 summarizes the T-dependence of the negative peak of both $\rho_{D,B}$ and $\rho_{D,T}$ at DNP, showing a decrease of the drag resistivity with increasing T. At the lowest T, mesoscopic fluctuations [67] are also noticeable in the proximity of DNP in Fig. 3.17, superimposed onto the large negative drag.

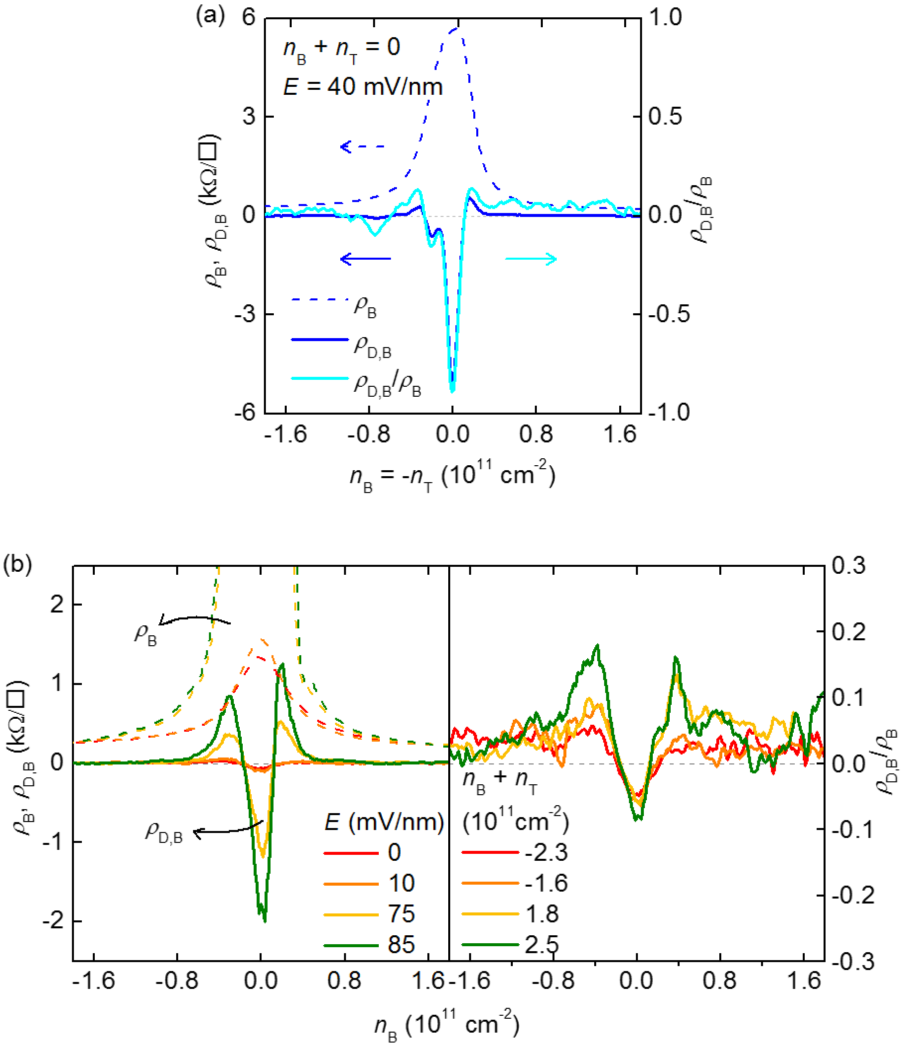

Figure 3.16: (a) ρ_B, $\rho_{D,B}$ (left axis), and $\rho_{D,B}/\rho_B$ (right axis) as a function of $n_B = -n_T$, measured at T = 1.5 K in sample #4. The $\rho_{D,B}$ and ρ_B values are comparable at DNP. The E-field across the bottom bilayer (drag layer) is 40 mV/nm at DNP. (b) Left panel: ρ_B (dashed lines), and $\rho_{D,B}$ (solid lines) vs. n_B in sample #4 at different E values in the bottom bilayer at T = 1.5 K. Right panel: $\rho_{D,B}/\rho_B$ vs. n_B corresponding to the left panel data. The data were acquired at constant $n_B + n_T$ total density values. (c) $\rho_{D,B}$ as a function of $n_B = -n_T$, in the proximity of DNP at different T, measured in sample #4 in a separate cooldown. The inset shows $\rho_{D,B}$ and $\rho_{D,T}$ vs. T at the DNP.

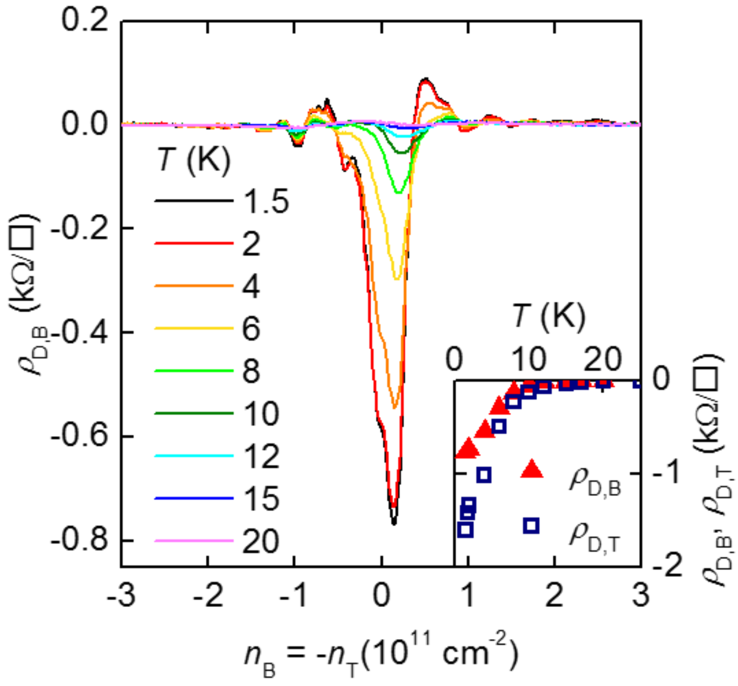

Figure 3.17: $\rho_{D,B}$ as a function of $n_B = -n_T$, in the proximity of DNP at different T, measured in sample #4 in a separate cooldown. The inset shows $\rho_{D,B}$ and $\rho_{D,T}$ vs. T at the DNP.

3.3.2 Drag in double bilayer graphene heterostructures without top hBN

For the samples with a relatively low mobility top bilayer graphene, not encapsulated by hBN, drag was probed mainly in the bottom bilayer which has higher mobility, while flowing a drive current in the top bilayer. Figure 3.18(a) shows the drag resistance ($R_{D,B}$) in the bottom bilayer, when the bottom and top bilayer carrier densities are balanced as $n_B = -\underline{n}_T$, measured at various T from 1.75 to 50 K in sample #7. The layer resistance (black trace) at 1.75 K, and the normalized drag (light blue trace) are also included. $R_{D,B}$ displays the strong, negative peak at DNP, marked by the blue triangle, changes its polarity as the density increases, and shows positive peaks at finite densities at both carrier types, marked by the red rectangle and orange circle. At higher carrier density, the drag resistance disappears. The overall behavior is similar to the observation in sample #4 (Fig. 3.16 and Fig. 3.17). The positive peaks of $R_{D,B}$ at finite densities in Fig. 3.18(a) are surprisingly strong, comparable to the negative peak at DNP, and the normalized drag of those peaks reaches ~35 %, even larger than the negative normalized drag at DNP here. As T increases, the drag peaks subside.

Figure 3.18(b) summarizes the T-dependence of the negative peak of $R_{D,B}$ at DNP (blue triangle), and the two positive peaks of $R_{D,B}$ at finite densities (red rectangle and orange circle), showing a decrease of the drag resistance with increasing T, as seen in sample #4 (Fig. 3.17 inset).

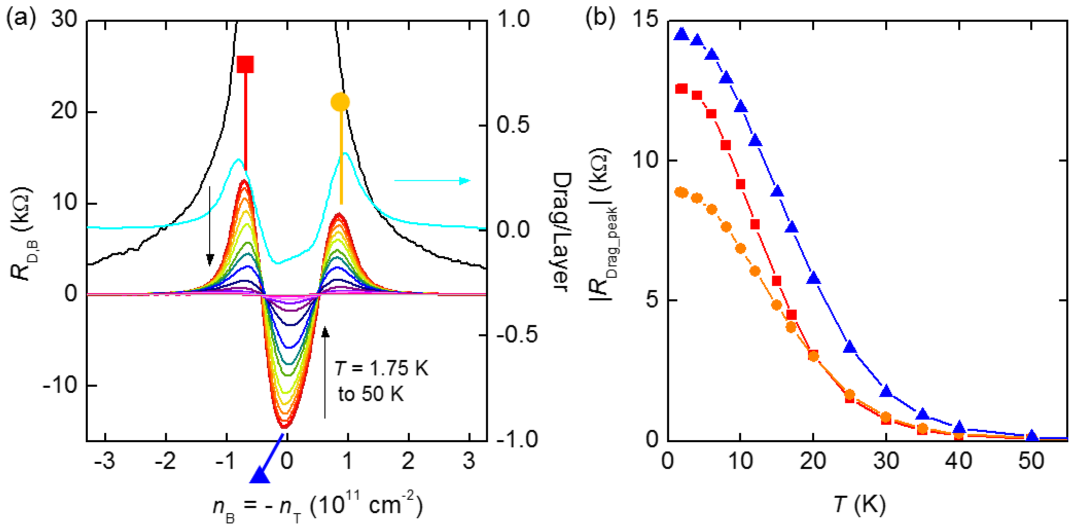

Figure 3.18: (a) $R_{D,B}$ as a function of $n_B = -n_T$, in the proximity of DNP at different T from 1.75 to 50 K (from red to pink color traces) measured in sample #7. The layer resistance (black trace) at 1.75 K, and the normalized drag (light blue trace) are also included. (b) T-dependence of the negative peak of $R_{D,B}$ at DNP (blue triangle), and the positive peaks of $R_{D,B}$ at finite densities (red rectangular and orange circle).

3.4 Possible Origins of the Anomalous Giant Drag

The experimental observations in Figs. 3.14 − 3.18 have several anomalous features at variance with existing Coulomb drag theories. It is tempting to interpret the giant drag that develops at DNP at low *T* as a signature of a correlated state of the two layers. However, the fact that the drag voltage is negative, namely opposite to the electric field in the drive layer, coupled with the layer reciprocity breakdown casts doubt on this interpretation. Moreover, the increasing ρ_D observed with decreasing T [Fig. 3.17 and Fig. 3.18] is opposite to the expected dependence for momentum transfer mediated drag [57,58]. The increasing drag at the lowest *T*, coupled with the apparent breakdown of reciprocity bears similarity with data reported in electron-hole double layers in GaAs-AlGaAs [62] or GaAs-graphene heterostructures [66]. We note that the interlayer separations in [62,66] were larger than 10 nm, and the magnitude of the measured drag resistivity was two orders of magnitude smaller than the values probed in the double bilayer graphene heterostructures investigated here. Indeed, the $\rho_{D,B} \approx \rho_B$ is a dramatic signature of the strong coupling regime in double layers.

3.4.1 Thermoelectric Origin for the Drag

To gain insight into the origin of the anomalous drag we first note that the $\rho_{D,B}$ and ρ_B peaks in Fig. 3.16(a) have similar widths. The giant peak at the DNP is reminiscent of energy drag near charge neutrality in double monolayer graphene heterostructures [59,65], where Coulomb mediated vertical energy transfer coupled with correlated density inhomogeneity in the two layers yields a drag resistivity of thermoelectric origin, with the polarity determined by interlayer correlations $\langle \delta\mu_B \delta\mu_T \rangle$. To assess the role of thermoelectricity in our measurements we use the Mott relation for the Peltier coefficient [74,75]:

$$Q = \frac{\pi^2 k_B{}^2 T^2}{3e} \frac{d\sigma/d\mu}{\sigma} \qquad (3.11)$$

where k_B is the Boltzmann constant, and σ the layer conductivity. Using Eq. (3.11) along with $\sigma = 1/\rho_B$ measured in the bottom bilayer graphene, the experimental μ_B vs. n_B data (Fig. 3.8) [18], and n_B vs. V_{BG} and V_{TL} (Fig. 3.9), we obtain Q_B vs. μ_B.

In Fig. 3.19(a) (main panel) we compare the drag layer chemical potential (μ_{Drag}) dependence of ρ_D and drag layer $-\partial Q/\partial\mu$, in samples #4, #2, and #5 at $T = 1.5$ K. The bottom (top) layer serve as drag layer in sample #4 and #2 (#5). The data of samples #4 and #5 were measured while sweeping the layer densities such that $n_B = -n_T$, whereas the data of sample #2 were measured while the bottom and top bilayer densities are not balanced as $n_B \neq -n_T$. A main difference between the three samples is that the drag layer mobility is 260,000 cm^2/Vs in sample #4 (bottom bilayer), 210,000 cm^2/Vs in sample #2 (bottom bilayer), and 19,000 cm^2/Vs in sample #5 (top bilayer). Remarkably, both ρ_D and $-\partial Q/\partial\mu$ show a peak at charge neutrality, change polarity as $|\mu_{Drag}|$ increases, and vanish at even larger $|\mu_{Drag}|$ values. Interestingly, the peak structure of energy drag in Ref. [59] arises from $\partial Q/\partial\mu$.

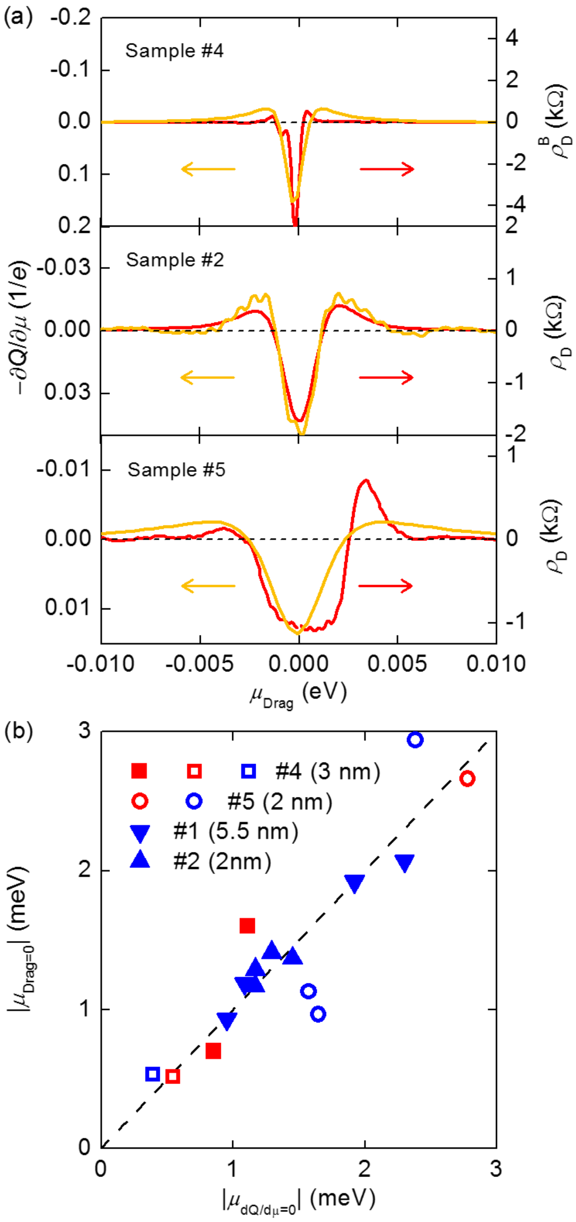

Figure 3.19: (a) Drag layer $-\partial Q/\partial \mu$ (yellow) and ρ_D (red) vs. μ_{Drag} in samples #4, #2, and #5 at T = 1.5 K. The data were acquired by sweeping the layer densities such that $n_B = -n_T$. (b) $|\mu_{Drag=0}|$ as a function of $|\mu_{\partial Q/\partial \mu=0}|$ of the drag layer for four samples, with different interlayer spacing shown in the legend. The open (closed) symbols mark data measured using the top (bottom) bilayer as drag layer. The red (blue) symbols represent data measured at zero (finite) drive layer density.

The striking similarity between the μ_{Drag}-dependence of ρ_{D} and $-\partial Q/\partial\mu$ strongly suggests a thermoelectric origin for the large frictional drag observed at low T in our double bilayer graphene. To further test this hypothesis, in Fig. 3.19(b) we compare the μ_{Drag} value at which ρ_{D} changes polarity ($|\mu_{\text{Drag}=0}|$), and the μ value at which the drag layer $\partial Q/\partial\mu$ changes its polarity ($|\mu_{dQ/d\mu=0}|$) for multiple samples. The $|\mu_{\text{Drag}=0}|$ and $|\mu_{dQ/d\mu=0}|$ are averaged over the μ values on both electron and hole branches, and represent the half width of the ρ_{D} peak and the drag layer $\partial Q/\partial\mu$ peak, respectively. The $|\mu_{\text{Drag}=0}|$ and $|\mu_{dQ/d\mu=0}|$ values are determined using frictional drag measurements in either bottom or top bilayer graphene from four samples with different interlayer thickness and layer mobility. Furthermore, the data are collected at different drive layer densities, not only at DNP. Figure 3.19(b) clearly indicates that $|\mu_{\text{Drag}=0}|$ agrees very well with $|\mu_{dQ/d\mu=0}|$, suggesting that the overall behavior of the anomalous drag at low T is governed by the drag layer $\partial Q/\partial\mu$. Consistent with Figs. 3.14 and 3.15 data showing that ρ_{D} depends largely on the drag layer density, we do not find a correlation between the drag resistivity and the drive layer $\partial Q/\partial\mu$.

While reminiscent of energy drag, the giant drag measured here deviates from the simple energy drag picture presented in Ref. [59]. Also striking is the layer non-reciprocity, amplified by the giant drag at DNP [Fig. 3.16(a)]. We note that Ref. [59] assumes fully overlapping layers with identical geometries, and contact configurations. In contrast, in the actual devices examined here the geometry and contact configurations of the drive/drag layers are different [Fig. 3.14(a)]. As a result, anisotropic heat flow due to sample geometry [76] as well as Peltier heating outside of the active layers may contribute to the layer non-reciprocity in our drag measurements. A second ingredient that may lead to non-reciprocity is drive current-induced density gradient in both layers proportional to C_{int}, and to drive layer resistivity. The charge density gradient is not symmetric when interchanging the drive and drag layers, and is largest when the layer with the lower density is used as a drive layer. A fuller understanding of the origin of broken layer reciprocity at low T is the subject of intense current research.

The polarity of the energy drag is determined by the sign of potential fluctuations in graphene, $\langle \delta\mu_{\mathrm{B}}\delta\mu_{\mathrm{T}} \rangle$ [59]. A negative drag of thermoelectric origin measured at DNP indicates that $\langle \delta\mu_{\mathrm{B}}\delta\mu_{\mathrm{T}} \rangle < 0$. This suggests that strain [77], rather than charged impurities [78] dominates the density inhomogeneity. For impurity induced inhomogeneity $\langle \delta\mu_{\mathrm{B}}\delta\mu_{\mathrm{T}} \rangle > 0$, and a positive drag is expected at charge neutrality. The clearly developed, broken symmetry integer quantum Hall states in our samples (see the data shown in Chapter 2) also prove the high sample quality with low level of impurities.

3.4.2 Expected Difference in Energy Drag Between Monolayer and Bilayer Graphene

Lastly, we discuss similarities and differences between the energy drag previously observed in double monolayer graphene heterostructures [65,79], and the drag in double bilayer graphene heterostructures. The drag in monolayer graphene shows a peak at the DNP, has a positive value, and is maximum at higher temperatures, $T \approx 70$ K. The positive drag at DNP is understood as energy drag where impurity induced disorder creates a positive correlation of the layer chemical potential fluctuations $\langle \delta\mu_{\mathrm{B}}\delta\mu_{\mathrm{T}} \rangle$ [59].

Here, we briefly discuss how the band structure differences between monolayer and bilayer graphene impact the energy drag. We approximate $\sigma = ne\mu_{\mathrm{FE}} + \sigma_0$, where μ_{FE} is the layer mobility, and σ_0 is the conductivity at charge neutrality, determined by sample disorder and temperature. Using the linear energy-momentum dispersion for monolayer graphene, and the parabolic dispersion for bilayer graphene, Eq. (3.11) then can be written as

$$Q = \alpha \frac{\pi^2 k_{\mathrm{B}}{}^2 T^2}{3e} \frac{\mu}{\mu^2 + \delta^2} \qquad (3.12)$$

Here, $\alpha = 2$ and $\delta^2 = \sigma_0 \hbar^2 \upsilon^2 \pi / e\mu_{\mathrm{FE}}$ for monolayer graphene, υ is Fermi velocity and $\hbar$ is the reduced Planck's constant, and $\alpha = 1$ and $\delta^2 = \sigma_0 \hbar^2 \pi \mu / 2e\mu_{\mathrm{FE}} m^*$ for bilayer graphene, $m^* = 0.034\ m_{\mathrm{e}}$ is effective mass. Assuming nominal values $\sigma_0 = 2e^2/h$, $\upsilon = 10^6$ m/s, and $\mu_{\mathrm{FE}} = 100{,}000\ \mathrm{cm}^2/\mathrm{Vs}$ provide $\delta^2 = 66\ \mathrm{meV}^2$ for monolayer graphene. By contrast, δ^2 vanishes for bilayer graphene at charge neutrality. Consequently, for $T = 1.5$ K we obtain $\partial Q/\partial\mu|_{\mu=0} = -0.0017\ \mathrm{e}^{-1}$ in monolayer graphene, whereas $\partial Q/\partial\mu|_{\mu=0} = -1.9\ \mathrm{e}^{-1}$ in bilayer graphene, a value more than 1000 times larger compared to monolayer graphene.

The larger $\partial Q/\partial\mu$ leads to the large energy drag at charge neutrality in bilayer graphene, a striking difference which originates from the larger density of states in bilayer graphene by comparison to monolayer graphene. We note that the value of $\partial Q/\partial\mu$ at charge neutrality, calculated using the measured σ in bilayer graphene (Fig. 3.19(a)) is smaller than the above example, where the disorder-induced chemical potential fluctuations are neglected. To account for density fluctuations at charge neutrality, we substitute μ with an approximate potential fluctuation $\delta\mu = 5$ meV [78], which yields $\delta^2 = 0.85\ \mathrm{meV}^2$ and $\partial Q/\partial\mu|_{\mu=0} = 0.06\ \mathrm{e}^{-1}$ for bilayer graphene, close to the value presented in Fig. 3.19(a).

The T-dependence of $\partial Q/\partial\mu$ can be simply written as T^2/δ^2, where δ^2 includes the T-dependency of σ_0. Approximating to $\delta^2 \approx \delta_0^2 + 6.25(k_\mathrm{B}T)^2$ for both monolayer [59], and zero gap bilayer graphene provides several order smaller $\delta_0^2 = 0.7\ \mathrm{meV}^2$ for bilayer graphene compared to that of monolayer graphene $\delta_0^2 = 66\ \mathrm{meV}^2$ at $T = 1.5$ K. The simple picture in energy drag, assuming the layer reciprocity in the active region as in [59] and identical $\partial Q/\partial\mu$ for both bottom and top bilayer suggests the drag resistivity

$$\rho_{\mathrm{D,B}} = \rho_{\mathrm{D,T}} = \frac{1}{2T\kappa}\left(\frac{\partial Q}{\partial\mu}\right)^2 \sum_{\mathbf{q}} \frac{<\delta\mu_\mathrm{B}(-\mathbf{q})\delta\mu_\mathrm{T}(\mathbf{q})>}{1+\ell^2\mathrm{q}^2}, \qquad (3.13)$$

κ is thermal conductivity, and ℓ is the interlayer cooling length, which is close to the inelastic mean free path. Using the Widemann-Franz law $\kappa \propto \delta^2 T$, we obtain a T-dependence of drag resistivity at charge neutrality as $T^2/(\delta_0^2 + 6.25(k_\mathrm{B}T)^2)^3$, a non-monotonic function which reaches a maximum at a temperature T^*, where a lower value of δ^2 leads to a lower T^*. This estimate yields $T^* \sim 3$ K for double bilayer graphene system by comparison to $T^* \sim 30$ K for monolayer graphene, as shown in Fig. 3.20. We note that in monolayer graphene $\kappa \propto \delta^2/T$ [59] is a better approximation for $T > 50$ K, which further increases the T^* value.

We emphasize that while this estimation explains the sharp increase of the energy drag for $T < 10$ K in double bilayer graphene, along with a much larger magnitude, this calculation assumes reciprocity, where the drag resistivity depends on $\partial Q/\partial\mu$ values for both drive and drag layers. In contrast, our experimental data shows a much weaker dependence on the drive layer $\partial Q/\partial \mu$ at low temperature, which remains to the understood theoretically.

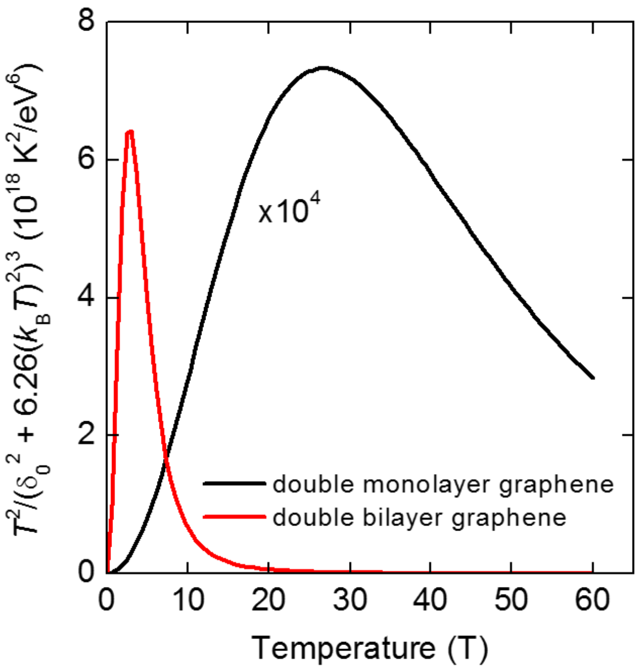

Figure 3.20: Expected temperature dependence of the energy drag in double monolayer and double bilayer graphene. The difference in energy-momentum dispersion between monolayer and bilayer graphene leads to a dramatic difference in the temperature dependence.

3.5 Magnetodrag and Hall Drag in Double Bilayer Graphene Heterostructures

Longitudinal drag (magnetodrag) and Hall drag measurements in weak magnetic (B) fields were also performed in our double bilayer graphene heterostructures. Figure 3.21 shows magnetodrag resistivity ($\rho_{xx,D}$) at $n_B = -n_T$, measured in the bottom bilayer at different B-fields and at T = 1.5 K, in sample #4. A negative peak in $R_{xx,D}$ is notable at DNP, which increases as the B-field increases. Figure 3.22(a,b) represent the magnitude of the negative peak of the magnetodrag resistivity (ρ_{xx,D_Peak}), and the peak of normalized magnetodrag at DNP ($\rho_{xx,D\_Peak}/\rho_{xx\_Peak}$), respectively, as a function of B-field. The negative peaks of both magnetodrag and normalized magnetodrag increase as the B-field increases up to ~ 1 T. At B-fields higher than 1 T, quantum Hall features emerge, the regime beyond our scope. In addition to the magnetodrag, we also measure Hall drag. Figure 3.23(b) shows Hall drag ($R_{xy,D}$) and Hall (R_{xy}) resistances measured in the bottom bilayer as a function of $n_B = -n_T$, at B = 0.6 T and at T = 1.5 K. $R_{xy,D}$ and R_{xy} were acquired using the same set of contacts in the bottom bilayer while flowing current in the top and bottom bilayer, respectively, in the same direction. The polarity of the Hall drag resistance is opposite to that of Hall resistance, which suggests our observed drag does not originate from electron-hole pairing.

The negative magnetodrag at charge neutrality, and its increasing magnitude with increasing B-field suggest that the energy-driven drag mechanism predicted by Song and Levitov [76,80] as the possible origin. As depicted schematically in Fig. 3.24(a,b) [76], in a weak magnetic field the trajectory of charge carriers is deflected in the drive layer (layer 1), which leads to a density gradient and, as a result, a temperature gradient (∇T_1), perpendicular to the drive current (**j**) flow. The efficient vertical heat transfer between the two bilayers induces the temperature gradient (∇T_2) also in the drag layer (layer 2), in the same direction as ∇T_1. This then leads charges to diffuse in the direction of ∇T_2, yielding voltage drops transversely and longitudinally by Lorentz force, which are Hall drag voltage V_H in Fig. 3.24(b) and magnetodrag voltage $V_{\parallel}$ in Fig. 3.24(a), respectively. The theoretically expected magnetodrag (Fig. 3.24(c)) and Hall drag (Fig. 3.24(d)) for a double monolayer graphene system with anisotropic heat flow [76] are analogous to our observation, although in our drag measurements the density regime other than $n_B = -n_T$ were not explored.

For the energy-driven drag in the double monolayer graphene, investigated theoretically [76] and experimentally [65,79], the energy-driven drag is expected to be observed at temperature higher than ~ 100 K. In contrast, we note our giant magnetodrag is observed at T = 1.5 K. For the full understanding of the temperature dependence, further theoretical studies are required. We suspect the estimated T-dependence difference in the zero field energy drag between monolayer and bilayer graphene, presented in Chapter 3.4.2 (Fig. 3.20), is related to the T-dependence of the energy-driven magnetodrag as well.

The magnetodrag was measured also in the top bilayer by interchanging the drive and drag layers. Magnetodrag in the top bilayer shows a negative peak at DNP as seen in the bottom bilayer, which increases with the magnetic field.

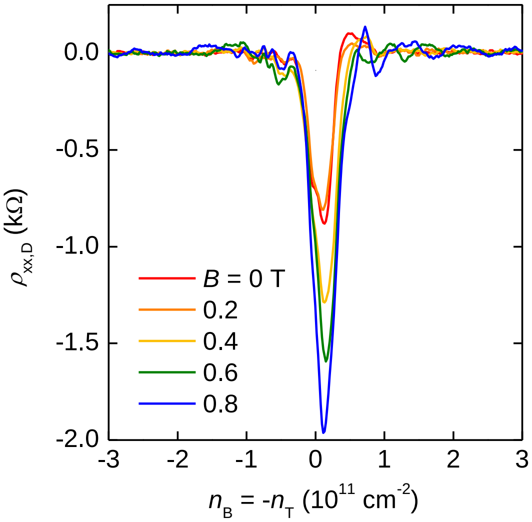

Figure 3.21: Magnetodrag ($\rho_{xx,D}$) as a function of $n_B = -n_T$, measured in the bottom bilayer at different B-fields and at T = 1.5 K, in sample #4. The negative peak is distinctive, which increases with increasing B-field.

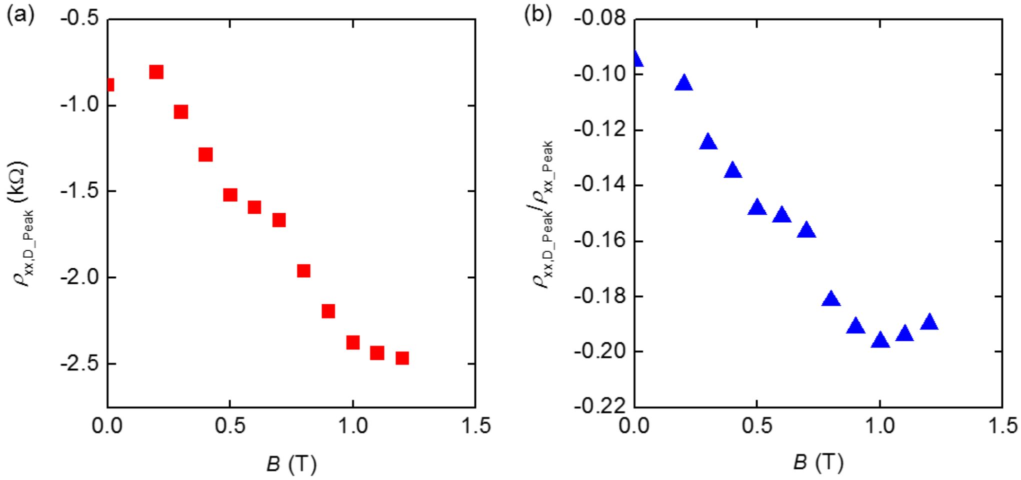

Figure 3.22: The magnitude of the negative peaks of magnetodrag (ρ_{xx,D_Peak}, panel (a)), and the normalized magnetodrag ($\rho_{xx,D\_Peak}/\rho_{xx\_Peak}$, panel (b)) as a function of B-field.

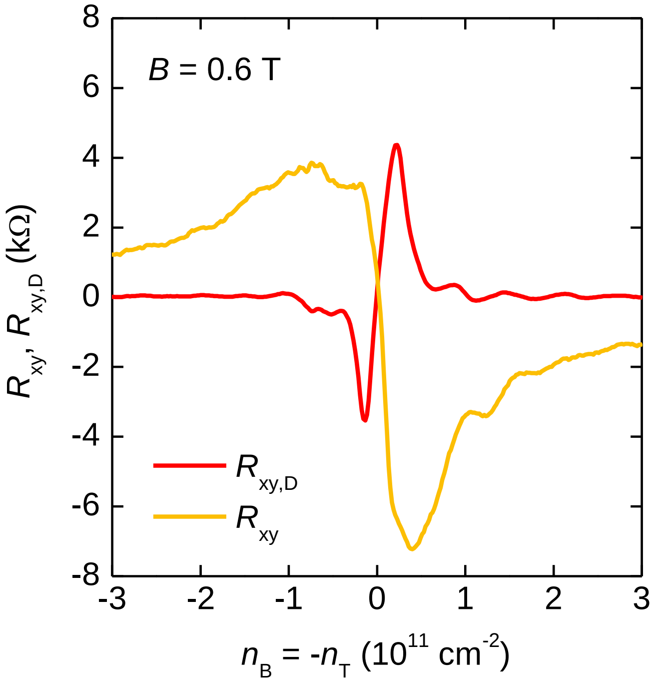

Figure 3.23: Hall resistance (R_{xy}) and Hall drag resistance ($R_{xy,D}$) as a function of $n_B = -n_T$, measured in the bottom bilayer at B = 0.6 T and at T = 1.5 K, in sample #4.

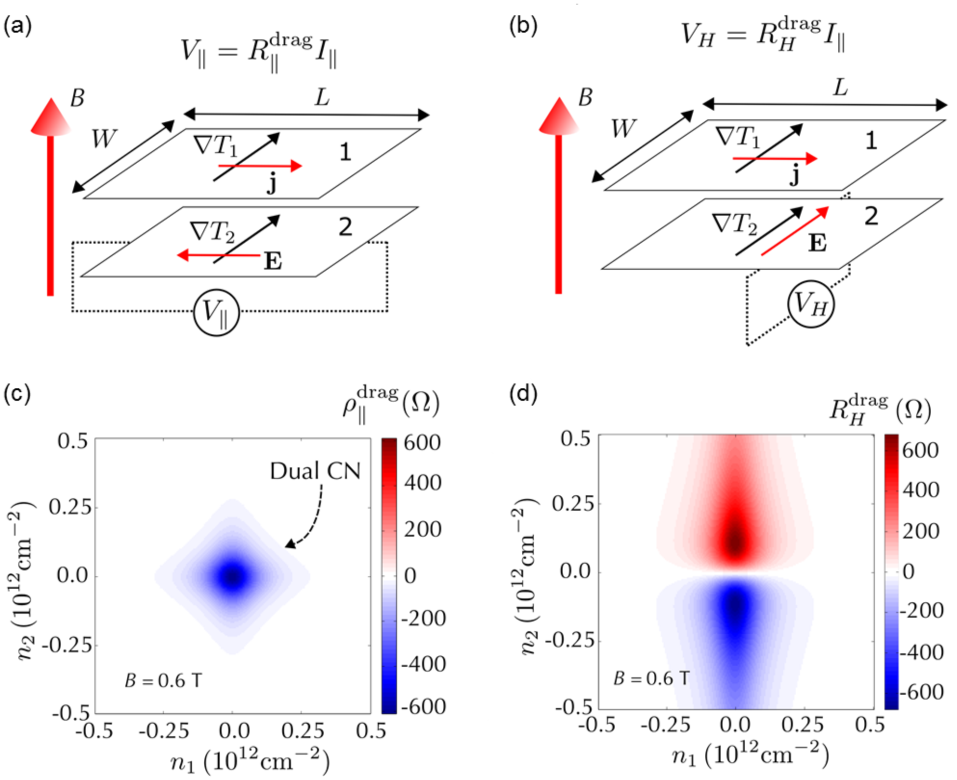

Figure 3.24: (a,b) The mechanism of energy-driven magnetodrag in a double layer system. In a weak magnetic field, the charge carriers in the drive layer (layer 1) are deflected, which causes temperature gradient (∇T_1). If the two layers are close enough for the interlayer thermal coupling, temperature gradient (∇T_2) is induced in the drag layer (layer 2), in the same direction as ∇T_1. This then leads charges to diffuse in the direction of ∇T_2, yielding a Hall drag voltage (V_H) and magnetodrag ($V_\parallel$) by the Lorentz force. Theoretically calculated energy-driven (c) magnetodrag resistivity ($\rho_\parallel^{\rm drag}$), and (d) Hall drag resistance ($R_H^{\rm drag}$) as a function of drive layer and drag layer densities, n_1 and n_2, respectively. The figures are adapted from [76].

3.6 Diffusive Drag at High Temperature

We measure the drag at zero magnetic field also at elevated temperatures, higher than 100 K. Figure 3.25 shows the drag resistances measured in the bottom ($R_{D,B}$) and top ($R_{D,T}$) bilayers as a function of n_B and n_T, at elevated T = 215 K in sample #4. We observe positive (negative) drag when the drive and drag layer carrier types are opposite (equal), and similar magnitudes in $R_{D,B}$ and $R_{D,T}$, which are much smaller than layer resistances. This Coulomb drag at high temperature is explained by the momentum transfer from the drive layer to drag layer, mediated by Coulomb scattering [58], as schematically described in Fig. 3.26 [61]. The illustration shows that electrons in the two-dimensional drive layer (bottom layer, red) push the holes in the drag layer (top layer, blue) to the direction opposite to the drive current by transferring their momenta ($m_e^* v_D$), and this gives rise to a positive drag. This phenomenon is called as diffusive drag, and was observed in AlGaAs-GaAs [57,58], and double monolayer graphene heterostructures [64,65,67]. Multiple samples were investigated, and we observe this high temperature drag (diffusive drag) increases as T increases in general, a conventional trend of diffusive drag [58,64,67,81]. Figure 3.25 also represents that the layer reciprocity is obeyed.

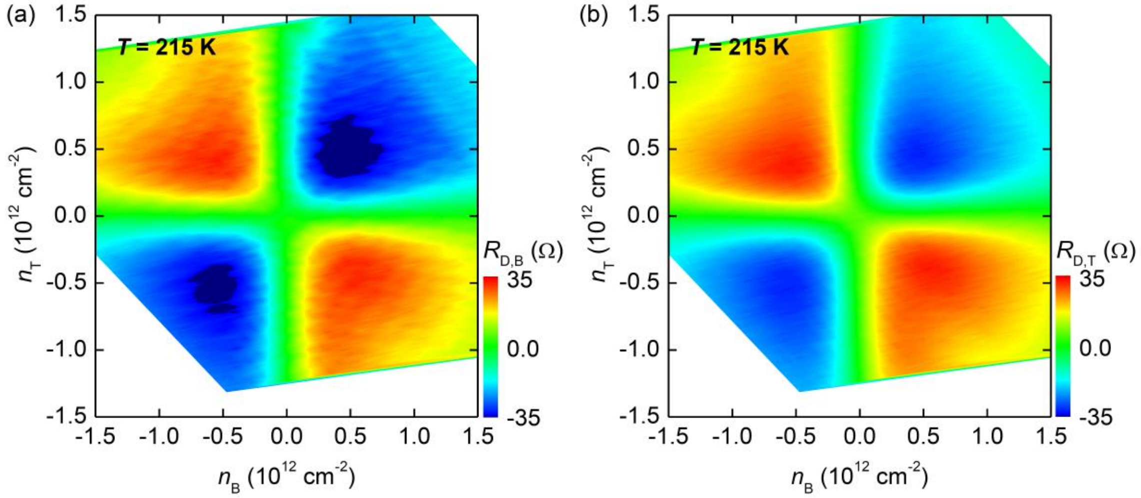

Figure 3.25: Momentum exchange induced drag at elevated temperatures in double bilayer graphene heterostructures: Drag resistances measured in the bottom ($R_{D,B}$) and top ($R_{D,T}$) bilayer as a function of n_B and n_T, at elevated T = 215 K in sample #4. We observe positive (negative) drag when the drive and drag layer carrier types are opposite (equal), and similar magnitudes in $R_{D,B}$ and $R_{D,T}$, indicating that the layer reciprocity is obeyed.

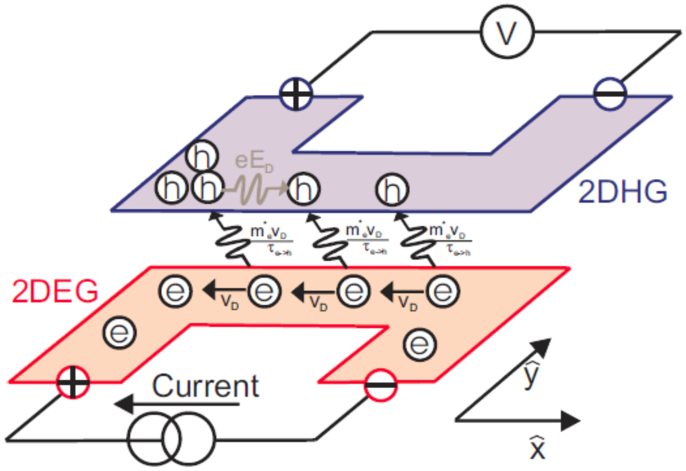

Figure 3.26: Schematic showing the momentum transfer from the drive layer (bottom layer, red) to drag layer (top layer, blue). The figure is adapted from Ref. [61].

3.7 Summary

In summary, we report an anomalous giant, negative frictional drag ≈ 1 kΩ in high mobility double bilayer graphene near the drag layer charge neutrality at temperatures lower than 10 K, with values approaching that of layer resistivity. The drag increases with decreasing T down to T = 1.5 K, and does not obey the layer reciprocity. While mimicking the dependencies expected for drag of thermoelectric origin, current theories of drag cannot account fully for all its anomalous features. This opens an unanticipated playground for exploring and controlling new electron-interaction mediated phenomena in double layer systems even at zero field.

Chapter 4

Conclusion

In this dissertation, we experimentally studied various physical phenomena in bilayer graphene and its heterostructures, which are two-dimensional quantum confined systems. In a high magnetic field, bilayer graphene shows quantum Hall effect, where the electron energy is quantized into highly degenerate energy levels, called Landau levels (LLs). We investigate the quantum Hall ferromagnetism in bilayer graphene, along with our accurate global LL energy measurement technique. A full (spin, valley, and LL orbital) degeneracy breaking is observed, and corresponding QH phases and their transitions are studied comprehensively as a function of magnetic and electric fields. In particular, new quantum Hall phases at $\nu = 0$ and at $\nu = \pm 2$ are observed, both of which states can be theoretically explained by the superposition of two different single-electron LLs. We measure LL energies, and QHS gaps in different phases, e.g. spin- or layer-polarized, and at different electric fields. We discuss the interplay between Zeeman splitting, electric field induced layer asymmetry, and electron-electron interaction, which leads to various phases of the quantum Hall states in bilayer graphene.

This thesis also investigates experimentally the role of many-body interaction in bilayer graphene, and double bilayer graphene heterostructures. At zero magnetic field, the chemical potential dependence on carrier density in bilayer graphene is reshaped by interaction, resulting in effective mass values lower than theoretical values calculated using the local density approximation. In the quantum Hall regime we observe the decreasing chemical potential as a function of density in the N = 0, 1 LLs, except for integer fillings where the chemical potential shows discontinuities because of QHS gaps, a counter-intuitive behavior called negative compressibility.

In double bilayer graphene heterostructures, where the inter-layer particle spacing can be smaller than the intra-layer particle spacing, we measure frictional drag in wide ranges of drive and drag densities to probe for quantum correlated states. A giant drag resistivity, comparable to layer resistivity was observed at zero magnetic field, which may be explained by an efficient energy transfer from the drive to drag layer. Although the phenomenon does not originate from electron-hole pair, a sought after phenomenon, our results are intriguing and inspire further investigation. Our double bilayer graphene heterostructures also show gate-tunable resonant quantum tunneling when the two bilayers are rotationally aligned [34,82]. We believe that these in-depth experimental transport studies in bilayer graphene and its heterostructures contribute to fundamental understanding of quantum behavior of quantum confined, low-dimensional electron systems.

The measurements of electronic structure, including band gap, effective mass, and Fermi velocity are fundamental for electronic and optical materials, indispensable to the design of applications based on them. We also show transport gap extraction technique, applied to probe the gaps in bilayer graphene tunable as a function of transverse electric fields. This technique is highly accurate especially for high mobility samples, such as graphene encapsulated by hBN, and simple and straightforward, compared to the gap extraction method based on temperature dependence measurements [55]. These transport spectroscopic techniques can be employed to explore new electronic and optical materials, and to examine the modified electronic structures, for instance, by using different dielectric interfaces [44,83], applying strain [84–87], reducing dimensions [88–90], or adding periodic potentials [91,92] by means of Moiré pattern [93–97] or periodic metal gates [98].

Appendix: List of Publication

1. Kayoung Lee, Jiamin Xue, David C. Dillen, Kenji Watanabe, Takashi Taniguchi, and Emanuel Tutuc, “Giant frictional drag in double bilayer graphene heterostructures,” *submitted* (2016).

2. Raluca I. Gearba, Minjung Kim, Kory M. Mueller, Peter A. Veneman, Kayoung Lee, Bradley J. Holliday, Calvin K. Chan, James R. Chelikowsky, Emanuel Tutuc, and Keith J. Stevenson, “Atomically-resolved elucidation of electrochemical covalent molecular grafting mechanism of single layer graphene,” *submitted* (2016).

3. Kyounghwan Kim, Stefano Larentis, Babak Fallahazad, Kayoung Lee, Jiamin Xue, David C. Dillen, Chris M. Corbet, and Emanuel Tutuc, “Band alignment in WSe_2-graphene heterostructures,” *ACS Nano* **9**, 4527 (2015).

4. Sangwoo Kang, Babak Fallahazad, Kayoung Lee, Hema C. P. Movva, Kyounghwan Kim, Chris M. Corbet, Takashi Taniguchi, Kenji Watanabe, Luigi Colombo, Leonard F. Register, Emanuel Tutuc, and Sanjay K. Banerjee, “Bilayer graphene-hexagonal boron nitride heterostructure negative differential resistance interlayer tunnel FETs,” *IEEE Electron Device Letters* **36**, 405 (2015).

5. Babak Fallahazad†, Kayoung Lee†, Sangwoo Kang†, Jiamin Xue, Stefano Larentis, Chris M. Corbet, Kyounghwan Kim, Hema C. P. Movva, Takashi Taniguchi, Kenji Watanabe, Leonard F. Register, Sanjay K. Banerjee, and Emanuel Tutuc, “Gate-tunable resonant tunneling in double bilayer graphene heterostructures,” *Nano Letters* **15**, 428 (2015). (†equal contribution)

6. Kayoung Lee, Babak Fallahazad, Jiamin Xue, David C. Dillen, Kyounghwan Kim, Takashi Taniguchi, Kenji Watanabe, and Emanuel Tutuc, “Chemical potential and quantum Hall ferromagnetism in bilayer graphene,” *Science* **345**, 58 (2014).

7. Kayoung Lee, Babak Fallahazad, Hongki Min, and Emanuel Tutuc, “Transport gap in dual-gated graphene bilayers using oxides as dielectrics,” *IEEE Transactions on Electron Devices* **60**, 103 (2013).

8. Babak Fallahazad, Yufeng Hao, Kayoung Lee, Seyoung Kim, Rodney S. Ruoff, and Emanuel Tutuc, “Quantum Hall effect in Bernal stacked and twisted bilayer graphene grown on Cu by chemical vapor deposition,” *Phys. Rev. B* **85**, 201408 (2012).

9. Babak Fallahazad, Kayoung Lee, Guoda Lian, Seyoung Kim, Domingo Ferrer, Luigi Colombo, and Emanuel Tutuc, “Scaling of the Al_2O_3 top dielectric in graphene field-effect transistors,” *Appl. Phys. Lett.* **100**, 093112 (2012).

10. Kayoung Lee, Seyoung Kim, Micha S. Point, T. E. Beechem, Taisuke Ohta, and Emanuel Tutuc, “Magnetotransport properties of quasi-free standing epitaxial graphene bilayer on SiC: evidence for Bernal stacking,” *Nano Letters* **11**, 3624 (2011).

11. Seyoung Kim, Kayoung Lee, and Emanuel Tutuc, “Spin-polarized to valley-polarized transition in graphene bilayers at $\nu = 0$ in high magnetic fields,” *Phys. Rev. Lett.* **107**, 016803 (2011).

12. Kayoung Lee, Sangwook Lee, Dahl-Young Khang, and Taeyoon Lee, “Wrinkling evolution of a growing bubble: the wonders of petal-like patterns in amorphous silicon membranes,” *Soft Matter* **6**, 3249 (2010).

13. W. J. Maeng, Gil Ho Gu, C. G. Park, Kayoung Lee, and Taeyoon Lee, and Hyungjun Kim, “$HfO_2/HfO_xN_y/HfO_2$ gate dielectric fabricated by in situ oxidation of plasma-enhanced atomic layer deposition HfN middle layer,” *Journal of The Electrochemical Society* **156**, G109 (2009).

References

[1] J. Lambert and R. Côté, Phys. Rev. B **87**, 115415 (2013).

[2] A. H. Castro Neto, F. Guinea, N. M. R. Peres, K. S. Novoselov, and A. K. Geim, Rev. Mod. Phys. **81**, 109 (2009).

[3] K. S. Novoselov, V. I. Falʹko, L. Colombo, P. R. Gellert, M. G. Schwab, and K. Kim, Nature **490**, 192 (2012).

[4] K. S. Novoselov, E. McCann, S. V. Morozov, V. I. Fal'ko, M. I. Katsnelson, U. Zeitler, D. Jiang, F. Schedin, and A. K. Geim, Nat. Phys. **2**, 177 (2006).

[5] E. McCann and V. I. Fal'ko, Phys. Rev. Lett. **96**, 086805 (2006).

[6] E. V. Castro, K. S. Novoselov, S. V. Morozov, N. M. R. Peres, J. M. B. L. dos Santos, J. Nilsson, F. Guinea, A. K. Geim, and A. H. C. Neto, Phys. Rev. Lett. **99**, 216802 (2007).

[7] M. Nakamura, E. V. Castro, and B. Dóra, Phys. Rev. Lett. **103**, 266804 (2009).

[8] Y. Barlas, R. Côté, K. Nomura, and A. H. MacDonald, Phys. Rev. Lett. **101**, 097601 (2008).

[9] M. Kharitonov, Phys. Rev. Lett. **109**, 046803 (2012).

[10] C.-H. Zhang and Y. N. Joglekar, Phys. Rev. B **77**, 233405 (2008).

[11] H. Min, R. Bistritzer, J.-J. Su, and A. H. MacDonald, Phys. Rev. B **78**, 121401 (2008).

[12] R. Bistritzer, H. Min, J. J. Su, and A. H. MacDonald, ArXiv08100331 Cond-Mat (2008).

[13] J. P. Eisenstein and A. H. MacDonald, Nature **432**, 691 (2004).

[14] M. Kellogg, I. B. Spielman, J. P. Eisenstein, L. N. Pfeiffer, and K. W. West, Phys. Rev. Lett. **88**, 126804 (2002).

[15] E. Tutuc, M. Shayegan, and D. A. Huse, Phys. Rev. Lett. **93**, 036802 (2004).

[16] A. Perali, D. Neilson, and A. R. Hamilton, Phys. Rev. Lett. **110**, 146803 (2013).

[17] D. S. L. Abergel, M. Rodriguez-Vega, E. Rossi, and S. Das Sarma, Phys. Rev. B **88**, 235402 (2013).

[18] K. Lee, B. Fallahazad, J. Xue, D. C. Dillen, K. Kim, T. Taniguchi, K. Watanabe, and E. Tutuc, Science **345**, 58 (2014).

[19] E. A. Henriksen and J. P. Eisenstein, Phys. Rev. B **82**, 041412(R) (2010).

[20] A. F. Young, C. R. Dean, I. Meric, S. Sorgenfrei, H. Ren, K. Watanabe, T. Taniguchi, J. Hone, K. L. Shepard, and P. Kim, Phys. Rev. B **85**, 235458 (2012).

[21] G. M. Rutter, S. Jung, N. N. Klimov, D. B. Newell, N. B. Zhitenev, and J. A. Stroscio, Nat. Phys. **7**, 649 (2011).

[22] J. Martin, B. E. Feldman, R. T. Weitz, M. T. Allen, and A. Yacoby, Phys. Rev. Lett. **105**, 256806 (2010).

[23] R. Saito, G. Dresselhaus, and M. S. Dresselhaus, *Physical Properties of Carbon Nanotubes* (Imperial College Press, 1998).

[24] M. S. Dresselhaus and G. Dresselhaus, Adv. Phys. **51**, 1 (2002).

[25] J.-C. Charlier, X. Gonze, and J.-P. Michenaud, Phys. Rev. B **43**, 4579 (1991).

[26] J. W. McClure, Phys. Rev. **104**, 666 (1956).

[27] J. W. McClure, Phys. Rev. **108**, 612 (1957).

[28] M. Mucha-Kruczyński, E. McCann, and V. I. Fal'ko, Semicond. Sci. Technol. **25**, 033001 (2010).

[29] K. Lee, S. Kim, M. S. Points, T. E. Beechem, T. Ohta, and E. Tutuc, Nano Lett. **11**, 3624 (2011).

[30] C. R. Dean, A. F. Young, I. Meric, C. Lee, L. Wang, S. Sorgenfrei, K. Watanabe, T. Taniguchi, P. Kim, K. L. Shepard, and J. Hone, Nat. Nanotechnol. **5**, 722 (2010).

[31] C. R. Dean, A. F. Young, P. Cadden-Zimansky, L. Wang, H. Ren, K. Watanabe, T. Taniguchi, P. Kim, J. Hone, and K. L. Shepard, Nat. Phys. **7**, 693 (2011).

[32] L. Wang, I. Meric, P. Y. Huang, Q. Gao, Y. Gao, H. Tran, T. Taniguchi, K. Watanabe, L. M. Campos, D. A. Muller, J. Guo, P. Kim, J. Hone, K. L. Shepard, and C. R. Dean, Science **342**, 614 (2013).

[33] K. Lee, J. Xue, D. C. Dillen, K. Watanabe, T. Taniguchi, and E. Tutuc, ArXiv160300757 Cond-Mat (2016).

[34] B. Fallahazad, K. Lee, S. Kang, J. Xue, S. Larentis, C. Corbet, K. Kim, H. C. P. Movva, T. Taniguchi, K. Watanabe, L. F. Register, S. K. Banerjee, and E. Tutuc, Nano Lett. **15**, 428 (2015).

[35] S. Kim, I. Jo, D. C. Dillen, D. A. Ferrer, B. Fallahazad, Z. Yao, S. K. Banerjee, and E. Tutuc, Phys. Rev. Lett. **108**, (2012).

[36] J. B. Oostinga, H. B. Heersche, X. Liu, A. F. Morpurgo, and L. M. K. Vandersypen, Nat. Mater. **7**, 151 (2008).

[37] R. T. Weitz, M. T. Allen, B. E. Feldman, J. Martin, and A. Yacoby, Science **330**, 812 (2010).

[38] S. Kim, K. Lee, and E. Tutuc, Phys. Rev. Lett. **107**, 016803 (2011).

[39] H. Min, B. Sahu, S. K. Banerjee, and A. H. MacDonald, Phys. Rev. B **75**, (2007).

[40] G. L. Yu, R. Jalil, B. Belle, A. S. Mayorov, P. Blake, F. Schedin, S. V. Morozov, L. A. Ponomarenko, F. Chiappini, S. Wiedmann, U. Zeitler, M. I. Katsnelson, A. K. Geim, K. S. Novoselov, and D. C. Elias, Proc. Natl. Acad. Sci. **110**, 3282 (2013).

[41] D. C. Elias, R. V. Gorbachev, A. S. Mayorov, S. V. Morozov, A. A. Zhukov, P. Blake, L. A. Ponomarenko, I. V. Grigorieva, K. S. Novoselov, F. Guinea, and A. K. Geim, Nat. Phys. **7**, 701 (2011).

[42] A. B. Kuzmenko, I. Crassee, D. van der Marel, P. Blake, and K. S. Novoselov, Phys. Rev. B **80**, (2009).

[43] J. Jung and A. H. MacDonald, Phys. Rev. B **89**, 035405 (2014).

[44] G. Borghi, M. Polini, R. Asgari, and A. H. MacDonald, Phys. Rev. B **82**, 155403 (2010).

[45] K. Zou, X. Hong, and J. Zhu, Phys. Rev. B **84**, (2011).

[46] E. McCann, Phys. Status Solidi B **244**, 4112 (2007).

[47] J. Chae, S. Jung, A. F. Young, C. R. Dean, L. Wang, Y. Gao, K. Watanabe, T. Taniguchi, J. Hone, K. L. Shepard, P. Kim, N. B. Zhitenev, and J. A. Stroscio, Phys. Rev. Lett. **109**, (2012).

[48] L. M. Malard, J. Nilsson, D. C. Elias, J. C. Brant, F. Plentz, E. S. Alves, A. H. Castro Neto, and M. A. Pimenta, Phys. Rev. B **76**, (2007).

[49] L. M. Zhang, Z. Q. Li, D. N. Basov, M. M. Fogler, Z. Hao, and M. C. Martin, Phys. Rev. B **78**, (2008).

[50] Z. Q. Li, E. A. Henriksen, Z. Jiang, Z. Hao, M. C. Martin, P. Kim, H. L. Stormer, and D. N. Basov, Phys. Rev. Lett. **102**, (2009).

[51] Y. J. Song, A. F. Otte, Y. Kuk, Y. Hu, D. B. Torrance, P. N. First, W. A. de Heer, H. Min, S. Adam, M. D. Stiles, A. H. MacDonald, and J. A. Stroscio, Nature **467**, 185 (2010).

[52] M. Yankowitz, J. I.-J. Wang, S. Li, A. G. Birdwell, Y.-A. Chen, K. Watanabe, T. Taniguchi, S. Y. Quek, P. Jarillo-Herrero, and B. J. LeRoy, APL Mater. **2**, 092503 (2014).

[53] P. Maher, C. R. Dean, A. F. Young, T. Taniguchi, K. Watanabe, K. L. Shepard, J. Hone, and P. Kim, Nat. Phys. **9**, 154 (2013).

[54] J. P. Eisenstein, L. N. Pfeiffer, and K. W. West, Phys. Rev. B **50**, 1760 (1994).

[55] Y. Zhao, P. Cadden-Zimansky, Z. Jiang, and P. Kim, Phys. Rev. Lett. **104**, 066801 (2010).

[56] B. E. Feldman, J. Martin, and A. Yacoby, Nat. Phys. **5**, 889 (2009).

[57] P. M. Solomon, P. J. Price, D. J. Frank, and D. C. La Tulipe, Phys. Rev. Lett. **63**, 2508 (1989).

[58] T. J. Gramila, J. P. Eisenstein, A. H. MacDonald, L. N. Pfeiffer, and K. W. West, Phys. Rev. Lett. **66**, 1216 (1991).

[59] J. C. W. Song and L. S. Levitov, Phys. Rev. Lett. **109**, 236602 (2012).

[60] H. Noh, S. Zelakiewicz, T. J. Gramila, L. N. Pfeiffer, and K. W. West, Phys. Rev. B **59**, 13114 (1999).

[61] C. P. Morath, Low Temperature Transport and Coulomb Drag Studies of Undoped Electron-Hole Bilayers, The University of New Mexico, 2009.

[62] A. F. Croxall, K. Das Gupta, C. A. Nicoll, M. Thangaraj, H. E. Beere, I. Farrer, D. A. Ritchie, and M. Pepper, Phys. Rev. Lett. **101**, 246801 (2008).

[63] J. A. Seamons, C. P. Morath, J. L. Reno, and M. P. Lilly, Phys. Rev. Lett. **102**, 026804 (2009).

[64] S. Kim, I. Jo, J. Nah, Z. Yao, S. K. Banerjee, and E. Tutuc, Phys. Rev. B **83**, 161401 (2011).

[65] R. V. Gorbachev, A. K. Geim, M. I. Katsnelson, K. S. Novoselov, T. Tudorovskiy, I. V. Grigorieva, A. H. MacDonald, S. V. Morozov, K. Watanabe, T. Taniguchi, and L. A. Ponomarenko, Nat. Phys. **8**, 896 (2012).

[66] A. Gamucci, D. Spirito, M. Carrega, B. Karmakar, A. Lombardo, M. Bruna, L. N. Pfeiffer, K. W. West, A. C. Ferrari, M. Polini, and V. Pellegrini, Nat. Commun. **5**, 5824 (2014).

[67] S. Kim and E. Tutuc, Solid State Commun. **152**, 1283 (2012).

[68] K. Lee, B. Fallahazad, H. Min, and E. Tutuc, IEEE Trans. Electron Devices **60**, 103 (2013).

[69] K. Zou and J. Zhu, Phys. Rev. B **82**, 081407 (2010).

[70] T. Taychatanapat and P. Jarillo-Herrero, Phys. Rev. Lett. **105**, 166601 (2010).

[71] C. C. Hobbs, L. R. C. Fonseca, A. Knizhnik, V. Dhandapani, S. B. Samavedam, W. J. Taylor, J. M. Grant, L. G. Dip, D. H. Triyoso, R. I. Hegde, D. C. Gilmer, R. Garcia, D. Roan, M. L. Lovejoy, R. S. Rai, E. A. Hebert, H.-H. Tseng, S. G. H. Anderson, B. E. White, and P. J. Tobin, IEEE Trans. Electron Devices **51**, 971 (2004).

[72] C. C. Hobbs, L. R. C. Fonseca, A. Knizhnik, V. Dhandapani, S. B. Samavedam, W. J. Taylor, J. M. Grant, L. G. Dip, D. H. Triyoso, R. I. Hegde, D. C. Gilmer, R. Garcia, D. Roan, M. L. Lovejoy, R. S. Rai, E. A. Hebert, H.-H. Tseng, S. G. H. Anderson, B. E. White, and P. J. Tobin, IEEE Trans. Electron Devices **51**, 978 (2004).

[73] C. Hobbs, L. Fonseca, V. Dhandapani, S. Samavedam, B. Taylor, J. Grant, L. Dip, D. Triyoso, R. Hegde, D. Gilmer, R. Garcia, D. Roan, L. Lovejoy, R. Rai, L. Hebert, H. Tseng, B. White, and P. Tobin, in *2003 Symp. VLSI Technol. 2003 Dig. Tech. Pap.* (2003), pp. 9–10.

[74] N. W. Ashcroft and N. D. Mermin, *Solid State Physics* (Brooks Cole, 2003).

[75] Y. M. Zuev, W. Chang, and P. Kim, Phys. Rev. Lett. **102**, 096807 (2009).

[76] J. C. W. Song and L. S. Levitov, Phys. Rev. Lett. **111**, 126601 (2013).

[77] M. Gibertini, A. Tomadin, F. Guinea, M. I. Katsnelson, and M. Polini, Phys. Rev. B **85**, 201405 (2012).

[78] J. Xue, J. Sanchez-Yamagishi, D. Bulmash, P. Jacquod, A. Deshpande, K. Watanabe, T. Taniguchi, P. Jarillo-Herrero, and B. J. LeRoy, Nat. Mater. **10**, 282 (2011).

[79] M. Titov, R. V. Gorbachev, B. N. Narozhny, T. Tudorovskiy, M. Schütt, P. M. Ostrovsky, I. V. Gornyi, A. D. Mirlin, M. I. Katsnelson, K. S. Novoselov, A. K. Geim, and L. A. Ponomarenko, Phys. Rev. Lett. **111**, 166601 (2013).

[80] J. C. W. Song, D. A. Abanin, and L. S. Levitov, Nano Lett. **13**, 3631 (2013).

[81] A.-P. Jauho and H. Smith, Phys. Rev. B **47**, 4420 (1993).

[82] S. Kang, B. Fallahazad, K. Lee, H. Movva, K. Kim, C. M. Corbet, T. Taniguchi, K. Watanabe, L. Colombo, L. F. Register, E. Tutuc, and S. K. Banerjee, IEEE Electron Device Lett. **36**, 405 (2015).

[83] C. Hwang, D. A. Siegel, S.-K. Mo, W. Regan, A. Ismach, Y. Zhang, A. Zettl, and A. Lanzara, Sci. Rep. **2**, (2012).

[84] F. Guinea, M. I. Katsnelson, and A. K. Geim, Nat. Phys. **6**, 30 (2010).

[85] V. M. Pereira and A. H. Castro Neto, Phys. Rev. Lett. **103**, 046801 (2009).

[86] M. Huang, H. Yan, T. F. Heinz, and J. Hone, Nano Lett. **10**, 4074 (2010).

[87] C. R. Woods, L. Britnell, A. Eckmann, R. S. Ma, J. C. Lu, H. M. Guo, X. Lin, G. L. Yu, Y. Cao, R. V. Gorbachev, A. V. Kretinin, J. Park, L. A. Ponomarenko, M. I. Katsnelson, Y. N. Gornostyrev, K. Watanabe, T. Taniguchi, C. Casiraghi, H.-J. Gao, A. K. Geim, and K. S. Novoselov, Nat. Phys. **10**, 451 (2014).

[88] Y.-W. Son, M. L. Cohen, and S. G. Louie, Phys. Rev. Lett. **97**, 216803 (2006).

[89] L. Yang, C.-H. Park, Y.-W. Son, M. L. Cohen, and S. G. Louie, Phys. Rev. Lett. **99**, 186801 (2007).

[90] M. Y. Han, B. Özyilmaz, Y. Zhang, and P. Kim, Phys. Rev. Lett. **98**, 206805 (2007).

[91] C.-H. Park, L. Yang, Y.-W. Son, M. L. Cohen, and S. G. Louie, Phys. Rev. Lett. **101**, 126804 (2008).

[92] C.-H. Park, L. Yang, Y.-W. Son, M. L. Cohen, and S. G. Louie, Nat. Phys. **4**, 213 (2008).

[93] M. Yankowitz, J. Xue, D. Cormode, J. D. Sanchez-Yamagishi, K. Watanabe, T. Taniguchi, P. Jarillo-Herrero, P. Jacquod, and B. J. LeRoy, Nat. Phys. **8**, 382 (2012).

[94] B. Hunt, J. D. Sanchez-Yamagishi, A. F. Young, M. Yankowitz, B. J. LeRoy, K. Watanabe, T. Taniguchi, P. Moon, M. Koshino, P. Jarillo-Herrero, and R. C. Ashoori, Science **340**, 1427 (2013).

[95] L. A. Ponomarenko, R. V. Gorbachev, G. L. Yu, D. C. Elias, R. Jalil, A. A. Patel, A. Mishchenko, A. S. Mayorov, C. R. Woods, J. R. Wallbank, M. Mucha-Kruczynski, B. A. Piot, M. Potemski, I. V. Grigorieva, K. S. Novoselov, F. Guinea, V. I. Fal'ko, and A. K. Geim, Nature **497**, 594 (2013).

[96] C. R. Dean, L. Wang, P. Maher, C. Forsythe, F. Ghahari, Y. Gao, J. Katoch, M. Ishigami, P. Moon, M. Koshino, T. Taniguchi, K. Watanabe, K. L. Shepard, J. Hone, and P. Kim, Nature **497**, 598 (2013).

[97] Z. F. Wang, F. Liu, and M. Y. Chou, Nano Lett. **12**, 3833 (2012).

[98] S. Dubey, V. Singh, A. K. Bhat, P. Parikh, S. Grover, R. Sensarma, V. Tripathi, K. Sengupta, and M. M. Deshmukh, Nano Lett. **13**, 3990 (2013).

Vita

Kayoung Lee was born in Yeocheon, South Korea on 18 May 1985. She received the degree of B.S.E.E from Yonsei University at Seoul in 2009. She entered the Electrical and Computer Engineering M.S.E/Ph.D program at the University of Texas at Austin in 2009. She earned the degree of M.S.E in 2012.

Permanent address (or email): 11500 Jollyville Rd Apt 1024
Austin, Texas 78759

This dissertation was typed by Kayoung Lee.